Title

Net fluxes of broadband shortwave and photosynthetically active radiation complement NDVI and near infrared reflectance of vegetation to explain gross photosynthesis variability across ecosystems and climate

Authors

Mallick, Kanishka
Verfaillie, Joseph
Wang, Tianxin
et al.

Publication Date

2024-06-01

DOI

10.1016/j.rse.2024.114123

Peer reviewed

Net Fluxes of Broadband Shortwave and Photosynthetically Active Radiation Complement NDVI and Near Infrared Reflectance of Vegetation to explain Gross Photosynthesis Variability Across Ecosystems and Climate

Kanishka Mallick[1,2], Joseph Verfaillie[2], Tianxin Wang[2], Ariane Arias Ortiz[2,3], Daphne Szutu[2], Koong Yi[2], Yanghui Kang[2], Robert Shortt[2], Tian Hu[1], Mauro Sulis[1], Zoltan Szantoi[4,5], Gilles Boulet[6], Joshua B Fisher[7], Dennis Baldocchi[2]

[1]Remote Sensing and Natural Resource Modeling, Department ERIN, Luxembourg Institute of Science and Technology, Luxembourg

[2]Department of Environmental Science, Policy and Management, University of California, Berkeley, CA, United States

[3]Department of Physics, Universitat Autònoma de Barcelona, Barcelona, Spain

[4]Science, Applications & Climate Department, European Space Agency, Frascati, Italy

[5]Department of Geography & Environmental Studies, Stellenbosch University, Stellenbosch, South Africa

[6]Centre d'Etudes Spatiales de la Biosphère, CNES, CNRS, INRAE, IRD, UPS, Toulouse, France,

[7]Schmid College of Science and Technology, Chapman University, 1 University Drive, Orange, CA, 92866, USA

Corresponding author: Kanishka Mallick (email: kaniska.mallick@gmail.com; kaniska.mallick@list.lu)

Abstract

A grand challenge in global change research is understanding how the interaction of vegetation with the environment influences ecosystem gross primary productivity (GPP) through carbon assimilation. An evolving goal is to continuously predict GPP variability everywhere by finding a robust scaling relationship between flux tower GPP and satellite spectral reflectance. The footprint mismatch between the pixel size of many early satellite measurements and eddy flux measurements is a major hindrance in such an endeavor. By using a large set of growing season data covering 100 site-years in North and Central America, we explored the potential of transforming incident and reflected shortwave (R_g) and photosynthetically active radiation (PAR) measurements into a broadband normalized difference vegetation index (NDVI) and near-infrared (NIR) reflectance of vegetation (NIRv) which simultaneously explains the GPP variability. We found that the broadband NDVI and NIRv derived from R_g and PAR measurements at the daily time scale were highly correlated with Planet Fusion, Landsat-8/9, and Sentinel-2 narrowband NDVI and NIRv across a wide range of climate and ecological gradients. The differences between satellite and broadband NDVI and NIRv were found to be significantly associated with soil background variations, phenological stages, water stress and signal saturation of broadband NIR reflectance at high biomass. The seasonal variability of broadband NDVI and NIRv remarkably captured the seasonality of vegetation phenology, evaporative fraction, GPP and rainfall in different ecosystems. Although a saturation of GPP at high NDVI was evident, a linear relationship between broadband NIRv times incident PAR versus GPP indicated the strength of NIRv-based approach to capture the hidden light use efficiency impacts on GPP. We conclude that the inexpensive

measurement of R_g and PAR components can provide highly reliable information on NDVI, NIRv, and GPP uninterruptedly thereby augmenting the proximal sensing capability of the flux tower sites without the need for additional spectrometer measurements. The proposed in-situ vegetation indices make a stronger case on the use of radiation signals for handshaking between ecosystem-scale measurements and remote sensing observables relevant to carbon uptake.

Keywords: Spectral reflectance, broadband, vegetation index, NIRv, gross primary productivity, photosynthetically active radiation, ecosystem, climate

1. Introduction

Vegetation is an integral component of the biosphere influencing the variability of energy, water, and carbon dioxide fluxes (Ryu et al., 2012; Hoek van Dijke et al., 2020; Camps-Valls et al., 2021; Brown et al., 2017). Systematic information of biophysical metrics that describe vegetation vigor, phenological development, and biomass production are required to enhance our understanding of the flux variabilities in the climate system, for ecosystem monitoring and agricultural management practices (Brown et al., 2017; Richardson et al., 2010; Zhang et al., 2004, Sellers et al., 1997; Foley et al., 2011; Godfray et al., 2010). Consequently, leaf area index (LAI) and fraction of absorbed photosynthetically active radiation (FAPAR) are identified as two of the essential climate variables by the Global Climate Observing System (GCOS).

For the large-scale monitoring of vegetation development through remote sensing satellites, FAPAR and LAI are not available as direct measurements, and they need to be retrieved through complex radiative transfer models. However, there are two more biophysical metrics namely NDVI (Normalized Difference Vegetation Index) and GCC (Green Chromatic Coordinate) that are closely related to vegetation growth and development yet have a proximity with both FAPAR and LAI (Seyednasrollah et al., 2019; Gitelson et al., 2019; Richardson et al., 2007, 2013; Hao et al., 2012). In this context, NDVI can be directly obtained from the amount of reflectance in red and near-infrared (NIR, hereafter) regions of the electromagnetic spectrum. Similarly, GCC can also be directly calculated from the amount of reflectance in red, green, and blue regions (Richardson et al., 2007; Brown et al., 2017).

Using the theory of strong absorption of photosynthetically active radiation (PAR) in the red region and dissipation of energy through reflection of the NIR radiation, a vast body of literature explored the potential of satellite derived NDVI to understand the variability in gross primary productivity (GPP, hereafter) with vegetation growth and development (Ustin and Middleton, 2021; Liu et al., 2020, Magney et al., 2019, Huang et al., 2019; Prabhakara et al., 2015; Mutanga et al., 2023; Tesfaye and Awoke, 2021; Mutanga and Skidmore, 2004). An asymptotic pattern in NDVI at maximum vegetation growth became evident from all these studies, and NDVI yielded poor GPP estimates in evergreen vegetation (Pierrat et al., 2022) or during the peak seasons when vegetation reaches maturity (Mutanga et al., 2023; Mutanga and Skidmore, 2004). This saturation is attributed to the imbalance due to the insensitivity of chlorophyll absorbing red light at dense canopy cover (Kumar et al., 2001, Mutanga et al., 2023) versus a simultaneous rise in the NIR reflectance, apparently leading to negligible changes in NDVI. Studies showed that NIR reflectance scales with leaf nitrogen (Ollinger et al., 2011), and therefore NIR reflectance can be used as an index of photosynthetic capacity (Field and Mooney, 1986).

Following the analogy of linearity between GPP versus the product of absorbed PAR and light use efficiency, NIR reflectance of vegetation (NIRv) (product of NDVI and NIR reflectance) is explored to understand the magnitude and variability of GPP at hourly-to-daily and from ecosystem to global scale (Badgley et al., 2017; Baldocchi et al., 2020). The philosophy of linking GPP with NIRv is based on the fact that increasing biomass (leaf layer) in the canopy results in multiple scattering, which leads to significant changes in NIR reflectance in moderate-to-high vegetation density (LAI from 2 to 6) (Sellers et

al., 1997). Some of the more recent studies demonstrated a much tighter coupling when GPP is linked with the product of NIRv and incident PAR (Dechant et al., 2022). All these studies generated encyclopedic understanding on the pros and cons of NDVI and NIRv towards explaining the GPP variability across and within ecosystems. However, there are some open challenges. Firstly, how to bridge the scale gap in linking global remote sensing reflectance with eddy covariance GPP? Secondly, how to obtain the best and consistent NDVI and NIRv information at the same scale of flux tower GPP measurements? Thirdly, how to extrapolate the findings of a handful of ecosystems to global scale?

Over the last decade, there has been great evolution on in-situ monitoring of phenology through the PhenoCam network (http://phenocam.sr.unh.edu/) (Richardson et al., 2013; Filippa et al., 2018; Petach et al., 2014; Browning et al., 2017; Burke et al., 2021; Zhou et al., 2020; Tian et al., 2021). The broad objective is to develop deep insights into the temporal variation in phenology across (within) different (same) ecosystems, and how this variability is driven by environmental factors such as radiation, temperature, and precipitation. PhenoCam provides data at an intermediate scale between ground observations and satellite remote sensing. This camera-based monitoring of vegetation phenology is standardized with consumer-grade digital cameras (e.g., Sonnentag et al., 2012) which records a three-layer image (red, green, and blue: RGB) and a NIR monochrome image. Broadband NDVI can be calculated from these paired images, however, a correction is needed if the exposure between the two images is different and there is a need for empirical adjustments to make the camera NDVI match with satellite NDVI (Petach et al., 2014). Most of the cameras have a nearly horizontal field of view

with about a quarter of the image sky. This can lead to earlier green up and saturation as compared to PAR and shortwave radiation sensors with vertical fields of view that better match satellite imagery. Another disadvantage of camera-based approach is the pronounced variability in normalized channel brightness resulting from changes in quality and quantity of incident solar radiation (Richardson et al., 2007, Liu et al., 2022). Like the dedicated NDVI sensors, the PhenoCam network is a relatively new invention whereas many measurements of PAR and shortwave radiation extend much further back in time.

One of the emerging utilities of FLUXNET are continuous observations of NDVI and NIRv for assessing the contribution of vegetation seasonality on energy, water, and carbon fluxes at the corresponding flux tower footprint (Hoek van Dijke et al., 2020). Despite satellite NDVI providing global coverage of vegetation vigor, current NDVI products suffer from trade-off between high (low)-spatial and low(high)-temporal resolution. While coarse spatial resolution (250 m) satellite observations are available as continuous time series (e.g., MODIS and VIIRS), finer spatial resolution vegetation information (10 – 30 m) is available only as a discrete time series (e.g., Sentinel-2 and Landsat8/9). Contamination of satellite observations due to the cloud interference brings hindrance while diagnosing the seasonal variation of vegetation attributes. Therefore, NDVI and NIRv at the 'eyes and ears' of the flux towers and at the temporal resolution of flux measurements is a critical requirement, especially since it is nearly impossible to measure LAI daily and without destruction. This could complement operational remote sensing data and document considerable diversity in plant development and seasonality in

greenness over the representative vegetation in which the flux towers operate. This will simultaneously complement and magnify the legacy research of PhenoCam.

Many AmeriFlux sites are equipped with Decagon/METER (SRS-Ni, SRS-Nr) or Apogee (S2-111-SS, S2-112-SS, S2-411-SS, S2-412-SS) NDVI sensors on flux towers to capture the rapid change in ecosystem greenness and temporal variability of NDVI. However, these sensors have only been available since 2015, and the Decagon/METER model has already gone out of production. Both sensor models had early issues with stability as well (Anderson et al., 2016). The Apogee sensors have a similar cost to other research-grade radiation sensors (~$600 US). Thus, a major challenge concerns how to observe temporally continuous NDVI and NIRv at the flux tower sites accurately, inexpensively, and over the entire data record.

Based on measurements of incident (^{i}) and reflected (^{r}) components of PAR (symbolized as Q in the equations and figures) (Q^{i}, Q^{r}) in conjunction with incident (^{i}) and reflected (^{r}) shortwave radiation (R_g) (R_g^{i}, R_g^{r}), Huemmrich et al. (1999) and Wilson and Meyers (2007) showed the possibility of estimating a robust broadband NDVI, but with limited evaluation with respect to spatially coarse satellite NDVI over a restricted number of sites. The approach has great potential as measurements of Q contain information on the visible waveband and greenness, and net flux of R_g - Q measurements inform us about infrared reflectance (shortwave minus visible). While Rocha and Shaver (2009) evaluated broadband NDVI and enhanced vegetation index (EVI) at a burnt and an unburnt site in the high latitude, Rocha et al. (2021) assessed the effects of solar position on the relationship between ecosystem function and NDVI derived from R_g - Q measurements. However, it remains unclear how well a broadband NDVI and NIRv perform in a range

of ecosystems and how they relate to carbon uptake when plants are exposed to large fluctuations of covarying biometeorological limits. Therefore, the current work seeks to address the following science questions and objectives: *(SQ1) Can a broadband NDVI and NIRv retrieved from the flux tower shortwave and PAR measurements explain satellite NDVI and NIRv variability across ecosystems and climate of varying energy-water availability limits? (SQ2) How effectively does the broadband NDVI capture the phenological changes and function of vegetation on the land surface? (SQ3) Can we use broadband NDVI and NIRv as a robust modulator of GPP across a wide range of energy-water availability? (SQ4) How does the background soil exposure variations, phenology, radiation components, and water stress impact the estimation of broadband NDVI?*

We present a cross-site synthesis of PAR and R_g observations to derive a broadband NDVI and NIRv (hereafter denoted as $NDVI_{bb}$ and $NIRv_{bb}$) across a diverse range of ecosystems, water- and energy-limited conditions. $NDVI_{bb}$ and $NIRv_{bb}$ patterns and their seasonal variability were compared with satellite NDVI, NIRv, and GCC at multiple spatial scales from 3-30 m spatial resolution using PLANET Fusion (continuous time series) and Harmonized Landsat Sentinel (HLS) (discrete time series) datasets. We analyzed the relationship between $NDVI_{bb}$, $NIRv_{bb}$, and PAR variability with GPP to fill a critical scale gap between flux footprint, ecosystem, and satellite remote sensing. As a final test, we assessed the role soil background variations in different phenological stages, radiation components, and water stress variations on the performance of $NDVI_{bb}$.

2. Materials and methods

2.1. Estimating $NDVI_{bb}$ and $NIRv_{bb}$

Beer's law already provides the theoretical link between incident, transmitted, and absorbed PAR versus leaf area. We hypothesize that from the net fluxes of PAR and R_g component measurements we can directly estimate $NDVI_{bb}$ and $NIRv_{bb}$, which simultaneously explains GPP variability (Baldocchi et al., 2020; Wilson and Meyers, 2007; Huemmrich et al., 1999). For estimating $NDVI_{bb}$ and $NIRv_{bb}$, estimation of visible and near-infrared reflectance ($\rho_{vis,bb}$, $\rho_{nir,bb}$) in the broad visible (0.4 – 0.7 µm) and near-infrared to shortwave infrared spectrum (0.7 – 3 µm) is needed. The derivation of $NDVI_{bb}$ is based on the theory of satellite narrowband NDVI. Vegetation shows strong absorption (85 – 90%) and low reflectance and transmittance (5 – 10%) in the visible wavelength. However, they show substantially higher reflectance, transmittance, and low absorption in the NIR radiation wavelength (Wilson and Meyers, 2007; Campbell and Norman, 1998). **Figure 1a** shows the conceptual diagram for estimating $\rho_{vis,bb}$ and $\rho_{nir,bb}$ from PAR and R_g measurements.

(a)

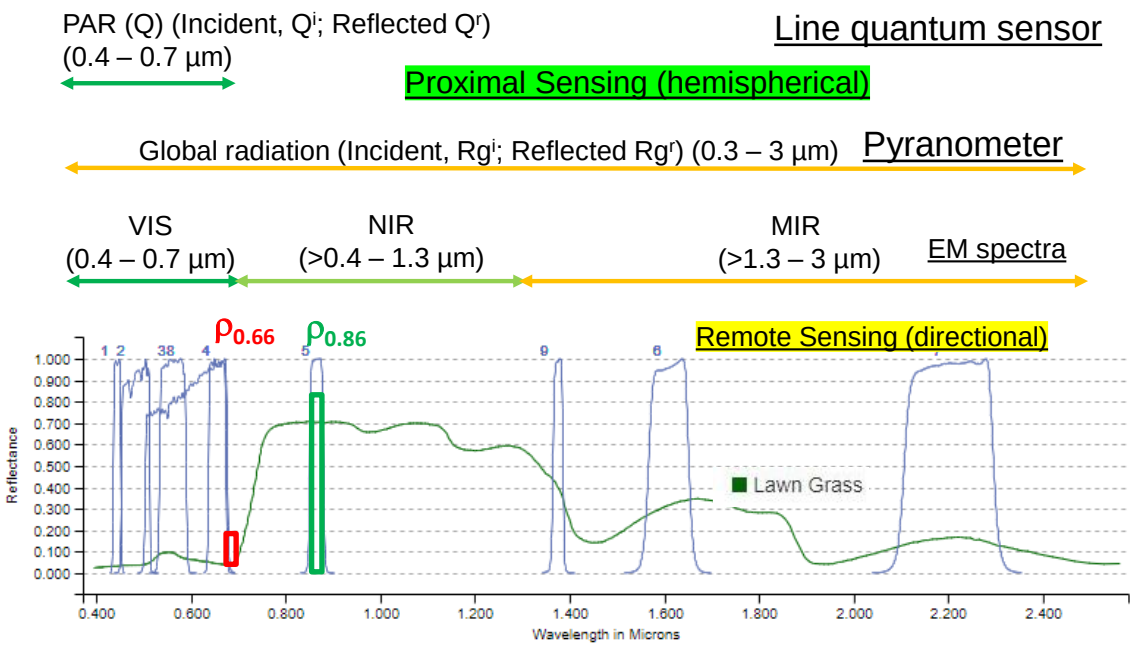

(b)

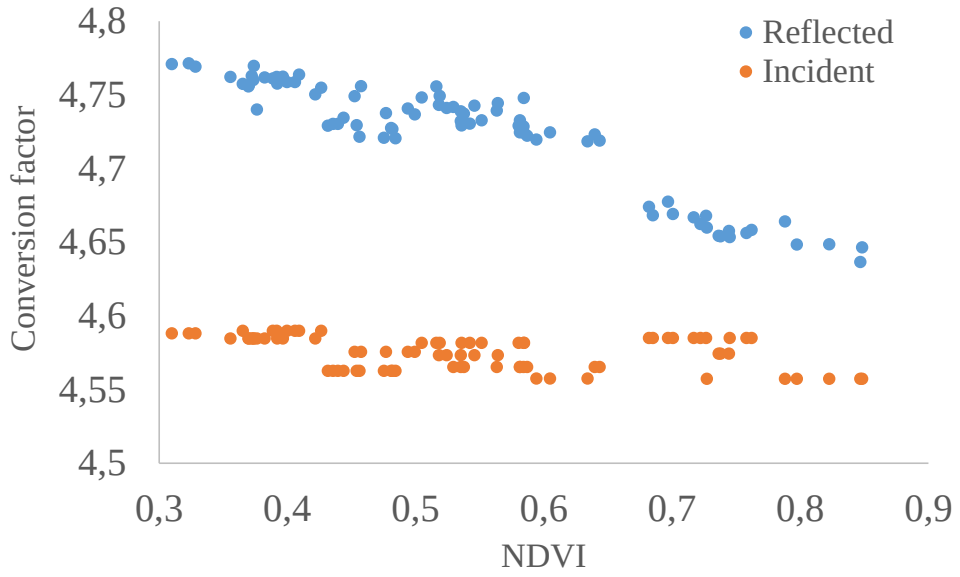

Figure 1: (a) Conceptual diagram showing the hypothesis for estimating broadband spectral reflectance from the measurements of hemispherical broadband radiation components in PAR and total shortwave spectral region. It also shows an example of the narrowband spectral reflectances that we obtain in red and near infrared spectral region from operational remote sensing satellite Landsat-9 (Source: https://landsat.usgs.gov/spectral-characteristics-viewer). VIS signified visible, NIR signifies near-infrared, MIR signifies mid-wave infrared. (b) Figure showing the scaling factor for converting PAR (both incident and reflected) from µmols/m^2/s to W/m^2 for a range of NDVI as an example over rice crop in California.

A pyranometer measures energy flux density in its native spectral range (0.3 – 3 µm) and the quantum sensor measures photon flux density in its native range (0.4 – 0.7 µm) (**Fig. 1**). To produce a broadband NDVI that deduces the reflectance of energy, we need to do a transformation, starting with the principle of Planck's law ($E = h\nu$, h = Planck's constant and ν = frequency of radiation) and information on the incoming solar spectrum and reflected spectrum. Therefore, we used the incident and reflected PAR measurements in conjunction with incident and reflected R_g measurements to segregate $\rho_{vis,bb}$ and $\rho_{nir,bb}$. The measurements of hemispherical broadband PAR and R_g components act as the proximal sensing data source to retrieve equivalent estimates of narrowband directional reflectances in red and NIR regions as obtained from remote sensing satellites (**Fig. 1**). The central wavelength of narrowband red and NIR directional reflectance of operational remote sensing satellite is around 0.66 ($\rho_{0.66}$) and 0.86 ($\rho_{0.86}$) µm. We hypothesize that separation of $\rho_{vis,bb}$ and $\rho_{nir,bb}$ from proximal sensing of broadband hemispherical PAR and R_g components are approximately equivalent to $\rho_{0.66}$ and $\rho_{0.86}$. Therefore,

$$NDVI_{bb} = (\rho_{nir,bb} - \rho_{vis,bb})/(\rho_{nir,bb} + \rho_{vis,bb})$$

$NDVI_{bb}$ is considered as approximately equivalent proxy for the standard NDVI [$NDVI = (\rho_{0.66} - \rho_{0.86})/(\rho_{0.66} + \rho_{0.86})$]. The implication of approximating $\rho_{vis,bb} \approx \rho_{0.66}$ and $\rho_{nir,bb} \approx \rho_{0.86}$ in different ecosystems are described in detail in section 3.4.

At first, $\rho_{vis,bb}$ was approximated from reflected (^{r}) and incident (^{i}) components of PAR (µmols/m^2/s) measurements (symbolized as Q) as follows:

$$\rho_{vis,bb} = Q^r/Q^i \quad (1)$$

For estimating $\rho_{nir,bb}$, the shortwave radiation components (R_g^i and R_g^r) were partitioned into downward broadband visible ($VIS_{i,bb}$) and near-infrared ($NIR_{i,bb}$) components following Weiss and Norman (1985) and Wilson and Meyers (1999), however with little modification.

$$\mathbf{VIS_{i,bb} = k_{vis} R_g^i} \quad \mathbf{(2)}$$

Here k_{vis} is the ratio of Q^i and R_g^i, where Q^i in µmols/m^2/s was converted to W/m^2 as (Q^i/4.5946). This conversion factor is based on the energy of photons of visible light in 0.4 – 0.7 µm region of the electromagnetic spectrum. Considering green wavelength (0.55 µm) as the central average wavelength in the entire visible band (0.4 – 0.7 µm), we can apply Planck's law as $E = hc/\lambda = Nhc/\lambda$. Where, h = Planck's constant (6.626×10^{-34} Js), c = speed of light (3×10^8 m/s), N = Avogadro number (6.022×10^{23} mol^{-1}). By putting the central wavelength of Q^i (λ = 0.55 µm), we can derive the scaling factor (i.e., 4.5946 µmols/joules) to convert Q^i from µmols/m^2/s to W/m^2. Maximum plant photosynthesis occurs in the blue (0.44 µm) and red light (0.66 µm) (Liu and Van Iersel, 2021). Putting these values in the conversion equation will make the conversion factor 3.6757 µmols/joules and 5.5135 µmols/joules for blue and red bands, respectively. However, these are the maximum and minimum conversion factors. Averaging these three conversion factors from blue, green, and red leads to the mean value of 4.5946 µmols/joules. Alternatively, by applying Planck's law at every 0.01 µm interval within the visible spectrum, followed by integration over the entire visible band also results in the same value. Thus, for every datapoint k_{vis} varies instead of assuming a constant (Weiss and Norman, 1985; Wilson and Meyers, 1999).

$$NIR_{i,bb} = k_{nir} R_g^i \quad (3)$$

Given there is no universal consensus on converting the energy of photons from µmols to watts beyond the visible region, we cannot apply the same factor to estimate k_{nir} from the reflected components of PAR and R_g for the NIR region. The conversion factor of 4.5946 µmols/joules is applicable for Q^i as we have Planck's law and a known solar spectrum. However, the reflected light is filtered and the filtering changes with season, leaf area, soil etc. Until now, there is no report on a scaling factor for converting reflected PAR from the molar to energy unit. Deriving such a scaling factor needs hyperspectral data of reflected PAR and shortwave radiation spectra. The UC Berkeley Biomet lab had collected reflected PAR and shortwave radiation spectra over rice, and we have computed this scaling factor for the reflected PAR for different classes of NDVI (**Fig. 1b**). While the conversion factor for the incoming PAR changes marginally with NDVI (4.56 – 4.60 µmols/joules), the conversion factor for the reflected PAR changes with season from 4.78 to 4.64 µmols/joules (**Fig. 1b**). The conversion factor of 4.72 µmols/joules is the average value for the reflected PAR as derived from the available observations in rice. Computing this value over other vegetation types is not within the scope of this study since it needs hyperspectral measurements.

In the present case, we estimate k_{nir} as (1 - k_{vis}). This gives us the advantage that no additional uncertainty is introduced due to the conversion from molar unit to energy unit for Q^r. This is also another reason that we did not adopt the approach of Huemmrich et al. (1999) to bypass any uncertainty for converting the reflected component of PAR from molar to energy unit.

From the partitioning of $VIS_{i,bb}$, the reflected upward broadband visible component ($VIS_{r,bb}$) is estimated as follows.

$$\mathbf{VIS_{r,bb} = \rho_{vis,bb} VIS_{i,bb}} \quad \textbf{(4)}$$

For estimating the upward reflected broadband near-infrared ($NIR_{r,bb}$), we used the R_g^r (W/m^2) measurements as follows.

$$\mathbf{NIR_{r,bb} = R_g^r - VIS_{r,bb}} \quad \textbf{(5)}$$

From the information of $NIR_{r,bb}$ and $NIR_{i,bb}$, we can now estimate $\rho_{nir,bb}$ as follows.

$$\mathbf{\rho_{nir,bb} = NIR_{r,bb}/NIR_{i,bb}} \quad \textbf{(6)}$$

From eqs. (1) and (6), VI_{bb} is computed as follows.

$$NDVI_{bb} = (\rho_{nir,bb} - \rho_{vis,bb})/(\rho_{nir,bb} + \rho_{vis,bb}) \quad \textbf{(7)}$$

Reflected near-infrared radiation from the vegetation, $NIRv_{bb}$, was calculated in terms of a renormalized $NDVI_{bb}$ times broadband NIR reflectance ($\rho_{nir,bb}$) ($NIRv_{bb} = NDVI_{bb} * \rho_{nir,bb}$) (Baldocchi et al., 2020; Badgley et al., 2019).

The daytime PAR and R_g components measured between 10:00 to 14:00 h were used for computing $\rho_{vis,bb}$ and $\rho_{nir,bb}$. The purpose of selecting this time slot is, all the operational remote sensing satellites have equatorial crossing time either around 10:00 – 11:00 h (Terra platform) or around 13:00 – 14:00 h (Aqua platform) (Wilson and Meyers, 2007). Thus, the comparison between satellite versus broadband NDVI will be coherent in this way. The daily values of $\rho_{vis,bb}$ and $\rho_{nir,bb}$ was estimated by averaging their 30-min values from 10:00 to 14:00 h, followed by the calculation of $NDVI_{bb}$ and $NIRv_{bb}$.

It is important to remember that satellite NDVI accounts for the signals of the entire field of view of the sensors. Based on the spatial resolution of the sensors, there is a possibility of inclusion of background soil reflectance in satellite NDVI due to different soil reflectance factors in red and NIR wave bands. Such possibility also exists while deriving $NDVI_{bb}$ from PAR and R_g measurements at the flux tower sites. For instance, in the deciduous vegetation and annual crops, early and late in the growing season when leaf area is small, the soil background can be seen by the sensors. The background reflectance can substantially influence the spectral reflectance (both for satellite and proximal) from the closed canopy due to multiple scattering in the NIR and SWIR bands. The extent of such background effects will be different in two methods of estimating NDVI. We anticipate that the impact of variations in soil background will be consequently reflected in their comparison.

2.2. Sites and data

The site locations, biome, vegetation type, climate and associated information are listed in **Table 1**. The analysis was carried out for cropland (CRO), grassland (GRA), woody savanna (WSA), open shrubland (OSH), forest (FOR), and nontidal wetlands (WET). These are AmeriFlux (11 sites) and NEON (14 sites) sites with publicly available data accessible through the respective AmeriFlux web pages. Seven out of eleven AmeriFlux site are from University of California, Berkeley, Biometeorology lab (https://nature.berkeley.edu/biometlab/sites.php) and the sites characteristics are published by the group (Baldocchi et al., 2020; Eichelmann et al., 2018; Hemes et al., 2019; Ma et al., 2016). The remaining four AmeriFlux sites are maintained by University of Nebraska (US-Ne3), University of Illinois (US-UiA, US-UiB), and United States

Department of Agriculture (US-Wkg), respectively. The description of the NEON sites is available in the NEON web page (https://www.neonscience.org/field-sites/explore-field-sites) and also in the site information of AmeriFlux (https://ameriflux.lbl.gov/sites).Croplands were a mix of rainfed (Ne3, UiA, UiB, xSL) and irrigated sites (Bi1, Bi2). While Bi2 received subsurface flooding irrigation, Bi1 received subsurface ditch irrigation (Bi2 receives a single irrigation in July-August, Bi1 receives 2 irrigations around May-June and August-September). Irrespective of single and multiple cropping systems, majority of the sites are covered with temporary crops followed by harvest and a bare soil period (Ne3, UiA, UiB, xSL). The time period of data availability for the individual sites are also mentioned in Table 1.

Table 1. Sites characteristics where both incident and reflected photosynthetically active radiation measurements are available (Superscripts, ^{P} = PLANET fusion; ^{HLS} = Harmonized Landsat and Sentinel); Planet fusion: 01/2018 – 12/2021; Landsat: **01/2014 – 12/2021**; Sentinel-2: **01/2016 – 12/2021**)

Biome	Site	Vegetation type	Latitude, Longitude	P (mm)	Climate type	Time period	Reference
CRO	Bi1$^{P, HLS}$	Alfalfa	38.0992, -121.4993	338	Csa	2016 – 2021	Wang et al. (2023)
	Bi2 $^{P, HLS}$	Corn	38.1091, -121.5351	338	Csa	2017 – 2021	Baldocchi et al. (2020)
	Ne3^{HLS}	Corn-soybean	41.1797, -96.4397	783	Dfa	2003 – 2021	Suyker et al. (2005)
	UiA^{HLS}	Switchgrass	40.0646, -88.1961	1051	Dfa	2015	Blackely et al. (2022)
	UiB^{HLS}	Miscanthus	40.0628, -88.1984	1051	Dfa	2014 – 2016	Blackely et al. (2022)
	xSL^{HLS}	Mixed	40.4619, -103.0293	432	Bsk	2017 – 2021	Metzger et al. (2019)
GRA	xAE^{HLS}	Herbaceous	35.4106, -99.0588	780	Cfa	2017 – 2021	Metzger et al. (2019)
	xCP^{HLS}	Herbaceous	40.8155, -104.7456	320	Bsk	2017 – 2021	Metzger et al. (2019)

	xKA[HLS]	Herbaceous	39.1104, -96.6129	850	Cfa	2017–-2021	Metzger et al. (2019)
	xKZ[HLS]	Herbaceous	39.1008, -96.5631	870	Cfa	2017–-2021	Metzger et al. (2019)
	Var[P, HLS]	Herbaceous	38.4133, -120.9508	559	Csa	2000 – 2021	Baldocchi et al. (2020)
	Wkg[HLS]	Herbaceous	31.7365, -109.9419	407	Bsk	2004 – 2021	Scott et al. (2010)
WSA	Ton[P, HLS]	Herbaceous, understory	38.4309, -120.9660	559	Csa	2001 – 2021	Baldocchi et al. (2020)
	xSJ[HLS]	Herbaceous, understory	37.1088, -119.7323	540	Csa	2018 – 2021	Metzger et al. (2019)
OSH	xJR[HLS]	woody (evergreen or deciduous)	32.5907, -106.8425	270	Bsk	2017 – 2021	Metzger et al. (2019)
	xNQ[HLS]	woody (evergreen or deciduous)	40.1776, -112.4524	288	Dfb	2017–-2021	Metzger et al. (2019)
	xSR[HLS]	woody (evergreen or deciduous)	31.9107, -110.8355	346	Bsk	2017 – 2021	Metzger et al. (2019)
FOR	xAB[HLS]	ENF	45.7624, -122.3303	2450	Csb	2017 – 2021	Metzger et al. (2019)
	xBL[HLS]	DBF	39.0603, -78.0716	983	Cfa	2017 – 2021	Metzger et al. (2019)
	xDL[HLS]	MF	32.5417, -87.8039	1372	Cfa	2017 – 2021	Metzger et al. (2019)
	xHa[HLS]	DBF	42.5369, -72.1727	1071	Dfb	2017 – 2021	Metzger et al. (2019)
	xJE[HLS]	ENF	31.1948, -84.4686	1307	Cfa	2017–-2021	Metzger et al. (2019)
WET	Myb[P,HLS]	herbaceous, woody	38.0499, -121.7650	338	Csa	2010 – 2021	Arias-Ortiz et al. (2021)
	TW1[P,HLS]	herbaceous	38.1074, -121.6469	421	Csa	2012 – 2020	Baldocchi et al. (2020)
	TW4[P,HLS]	herbaceous	38.1027, -121.6413	421	Csa	2013 – 2021	Eichelmann et al. (2018)

P: Annual precipitation (mm)

Bsk: Steppe: warm winter; Cfa: Humid Subtropical: mild with no dry season, hot summer; Csa: Mediterranean: mild with dry, hot summer; Csb: Mediterranean: mild with dry, warm summer; Dfa: Humid Continental: humid with severe winter, no dry season, hot summer; Dfb: Warm Summer Continental: significant precipitation in all seasons.

CRO: cropland; GRA: Grassland; WSA: Woody savanna; OSH: Open shrubland; FOR: Forest; WET: Wetland; ENF: Evergreen needleleaf forest; DBF: Deciduous broadleaf forest; MF: Mixed forest

2.3. Measurements: Radiation and Energy Flux Density and Biophysical Conditions

The incident and reflected PAR (Q^i and Q^r) measurements were made with upward and downward facing quantum sensors (Kipp & Zonen, PAR-Lite or PQS1) at each tower. The shortwave radiation components were measured by pyranometers, one facing upward for measuring the incident component (R_g^i) and the other looking downward for measuring the reflected component (R_g^r) (Kipp & Zonen, CNR1 or Hukseflux NR01). A suite of meteorological variables was measured in conjunction with the mass and energy flux measurements. Air temperature and relative humidity were measured once every 10 seconds (0.1Hz) with Vaisala HMP45 RH/Temp sensors, with fan-aspirated solar shields to represent ambient air and prevent solar heating. These data were then stored as a 30-min average.

Fluxes were calculated from high-frequency (20 Hz) continuous recordings of temperature, water vapor, and CO2 concentrations, along with three-dimensional measurements of wind velocities using infrared gas analyzers and a 3-D sonic anemometer mounted on a scaffold or a tower structure at each site. High-frequency data were integrated to 30-min intervals, and half-hourly fluxes were calculated from the covariance between fluctuations in the vertical wind velocity and concentrations of greenhouse gasses and energy. Common across sites are flux corrections and quality control, which include high-frequency data despiking, 2-D coordinate rotations, sensor separation distance, density corrections, and site-specific friction velocity (u*) filtering (Leuning, 2007, Wang et al., 2023).

Net CO2 exchange was partitioned into ecosystem respiration and gross photosynthesis (GPP) (symbolized as A_G in figures and equations) by training an Artificial Neural Network on nighttime CO2 fluxes (Biomet lab sites) or by applying partitioning algorithms based on the short-term temperature sensitivity of respiration and nighttime CO2 fluxes to extrapolate respiration from nighttime to daytime periods and thus predict ecosystem respiration at all times (Reichstein et al. 2005). Regardless of the partitioning method, A_G was estimated as the sum of measured net CO2 exchange and estimated ecosystem respiration. A_G and surface energy balance fluxes measured between 10:00 to 14:00 h were averaged from their 30-min values to support the analysis of $NDVI_{bb}$ and $NIRv_{bb}$.

Continuous measurements of leaf area index (LAI) were available from the University of California, Berkeley, Biometeorology lab for the Tonzi Ranch site. Three identical consumer grade point-and-shoot digital cameras (PowerShot A570IS, Canon, Japan) were used to quantify LAI continuously and details are available in Ryu et al. (2012). The cameras were leveled at 1 m height with the lens pointed towards the zenith. They were approximately 50 m apart and set to a maximum wide angle (focal length of 5.8 mm), automatic exposure, aperture priority mode and minimum aperture (F/2.6). These settings yielded a view zenith angle from 0 to 32° diagonally. The Canon Hack Development Kit (CHDK) (CHDK Project, http://chdk.wikia.com) was installed on the flash memory cards of the cameras to extend their capabilities, including digital repeat photography through a simple script written in uBasic (Sonnentag et al., 2012). The cameras were turned on and off with data loggers (CR200, CR10X, Campbell Scientific Inc., USA).

2.4. Remote sensing data

Three different satellite datasets, namely Planet Fusion and Harmonized Landsat Sentinel-2 (HLS) are used with spatial resolution varying between 3 and 30 m, respectively. Planet Fusion data was available from 2017 to 2021 as a daily continuous time series and HLS data was available from 01/2014 (Landsat) and 01/2016 (Sentinel-2) as a daily discrete time series at 3 - 5 days interval. Although HLS data is continuously generated, the Ameriflux database was updated until 12/2021 at the time of start of this analysis, and therefore the present analysis is restricted up to year 2021.

Planet Labs' Planet Fusion data set comes from a constellation of more than 100 CubeSats in low earth orbit. This provides high resolution (3m x 3m pixels) and high frequency revisits (<1day) but adds the complications of integrating data from many sensors, cross-calibration, and atmospheric contamination. The Planet Fusion processing combines this high resolution CubeSat data with MODIS/VIIRS, Landsat-8, and Sentinel-2 imagery to create a daily, gap filled product that is radiometrically accurate, and free of clouds and shadows. The technical specification can be found in https://assets.planet.com/docs/Planet_fusion_specification_March_2021.pdf. The Planet Fusion data was only available for seven UC Berkeley Biomet lab sites (**Table 1**) (US-Bi1, US-Bi2, US-Var, US-Ton, US-Myb, US-TW1, US-TW4). Therefore, comparison and evaluation of VI_{bb} and $NIRv_{bb}$ at 3 m spatial resolution was restricted to seven sites. For analyzing and comparing $NDVI_{bb}$ with Planet Fusion at 3 m spatial resolution, we extracted the radiation & associated meteorological variables, surface energy balance and carbon fluxes, and ancillary hydrological variables (soil moisture and precipitation) of

seven Biomet sites of California corresponding to the Planet Fusion data availability period.

HLS data was available across all the 25 sites. The HLS products take input data from the joint National Aeronautics and Space Administration-United States Geological Survey (NASA-USGS) Landsat-8 and Landsat-9 (L8/9, hereafter) and the European Space Agency (ESA) Sentinel-2A and Sentinel-2B (S2, hereafter) satellites to generate a harmonized, analysis-ready surface reflectance data product with observations every two to three days (https://www.earthdata.nasa.gov/esds/harmonized-landsat-sentinel-2) (Claverie et al., 2018). HLS data for all the sites were acquired for the central pixel of the tower sites through NASA AppEEARS (The Application for Extracting and Exploring Analysis Ready Samples, https://appeears.earthdatacloud.nasa.gov/). AppEEARS enables users to acquire datasets using coordinate, temporal, and band/layer information. For analyzing and comparing $NDVI_{bb}$ with HLS data at 30 m spatial resolution, we extracted the radiation & associated meteorological variables, surface energy balance and carbon fluxes, and ancillary hydrological variables (soil moisture and precipitation) of all the 25 sites corresponding to the data availability time-period of L8/9 (01/2014 – 12/2021) and S2 (01/2016 – 12/2021), respectively.

While we computed NDVI and NIRv from red and near-infrared surface reflectance as described in Baldocchi et al. (2020) and Badgley et al. (2019), we compared $NDVI_{bb}$ and $NIRv_{bb}$ against daily NDVI and NIRv from Planet Fusion and HLS (both L8/9 and S2) covering the time frame of both the datasets. The entire analysis is performed across 25 flux tower sites of Ameriflux that covers a broad spectrum of ecosystems and energy-water availability limits. For Planet Fusion, we used 5x5 pixel average values of

calculated NDVI and NIRv for all daily scenes around each flux tower sites (seven sites) of Biomet lab. For HLS, we acquired data over the central pixel of the flux tower location and conducted the subsequent evaluation.

2.5. Evaluation method

To evaluate $NDVI_{bb}$ and $NIRv_{bb}$ with respect to the satellite vegetation indices across different ecosystems and climate (SQ1), we used coefficient of determination (R^2), bias, root mean squared difference (RMSD), normalized root mean squared difference (nRMSD, in percent), and systematic root mean squared difference (sRMSD, in percent) as statistical metrics (**Fig. 3 – 8**; section 3.1). To assess the efficacy of $NDVI_{bb}$ in capturing the phenological changes and vegetation function (SQ2), we computed the mean seasonal variation of $NDVI_{bb}$ and satellite NDVI in terms of the daily mean values normalized by their annual mean (Baldocchi et al., 2021) and examined their responses to green chromatic coordinate (GCC) and evaporative fraction (ratio of latent heat flux and net available energy) (F_E). While GCC is used as a phenological metric to assess the responses of NDVIs with the progression from low vegetation cover (or senescent vegetation) until the peak vegetation, F_E indicates the biophysical response of vegetation at different developmental stages (**Fig. 9 – 10**; section 3.2). To understand the explanatory potential of $NDVI_{bb}$ and $NIRv_{bb}$ to the GPP variability (SQ3), we followed a two-step procedure. We first verified the intraseasonal variability (coefficient of variation, CV) in $NDVI_{bb}$ and $NIRv_{bb}$ by comparing them with the intraseasonal variability of GPP and corresponding precipitation variability for the growing season. Growing seasons includes all the days of spring, summer, and early autumn (i.e., periods April to middle October). We subsequently used both these indices in conjunction with

EC GPP measurements to examine their relationship for range of energy-water availability limits (**Fig. 11 – 12**; section 3.3). To understand the effects of soil background variations and phenological progression on $NDVI_{bb}$ retrieval and its consequent impact on $NDVI_{bb}$-NDVI difference (SQ4), we also adopted a two-step analysis. At the first step, we examined $NDVI_{bb}$-NDVI difference (δ_{NDVI}) with respect to GCC from senescent vegetation or bare soil to the peak vegetation stage. In this analysis, we used Soil Adjusted and Atmospherically Resistant Vegetation Index (SARVI) (Qi et al., 1994; Kaufman et al., 1992) as a third variable to simultaneously understand the impacts of soil background variations on δ_{NDVI} during different phenological stages (**Fig. 13**; section 3.4). At the second step, we analyzed the effects of individual radiation components on the performance of broadband hemispherical reflectances with respect to satellite directional reflectances (**Fig. 14 – 16**; section 3.4) across ecosystems. Same analysis is also performed for a range of energy-water availability limits and described in Appendix A4 (**Fig. A3 – A5**).

3. Results and discussion

To answer the four science questions, we organized the results and discussion into four sub-sections (3.1 to 3.4). The sequence of results and the corresponding figure numbers are in the order of the following progression.

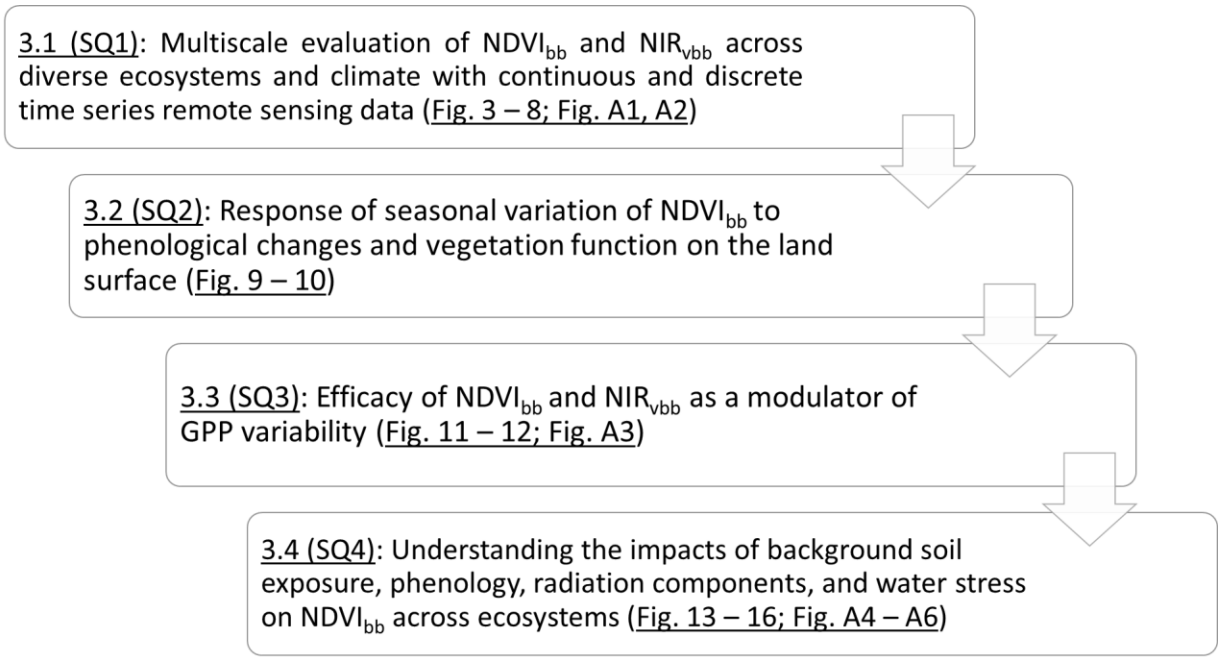

Figure 2: An illustrative diagram showing the sequence of results corresponding to the science questions (SQs) and the respective figure numbers associated with the description of results falling under individual science question.

3.1. Multiscale evaluation of broadband NDVI and NIRv across different ecosystems and climate (SQ1)

Planet Fusion evaluation: The scatterplots of $NDVI_{bb}$ versus Planet Fusion NDVI (**Fig. 3-6**) revealed a robust, stable, and linear relationship at all the four different ecosystems across seven EC flux tower sites of UC Berkeley Biomet lab in California. When all the data points of corn and alfalfa were combined, the goodness of fit of linear regression revealed $NDVI_{bb}$ to explain 86% of the variation of Planet Fusion NDVI ($R^2 = 0.86$) at the croplands (CRO) with bias, RMSD and sRMSD of 0.02, 0.08 and 52% for a wide range of available energy-water limit (represented through evaporative fraction, F_E). In CRO, the unexplained variation in $NDVI_{bb}$ at a given NDVI was larger for NDVI>0.7, which also corresponded to high water and available energy limits (**Fig. 3a**). Besides, some unexplained variation in $NDVI_{bb}$ at a given NDVI was also evident in CRO for low

NDVI (NDVI: 0.35 – 0.40) and low F_E (F_E: 0.3 – 0.4), which ultimately led to relatively less dense scatters around low NDVI region.

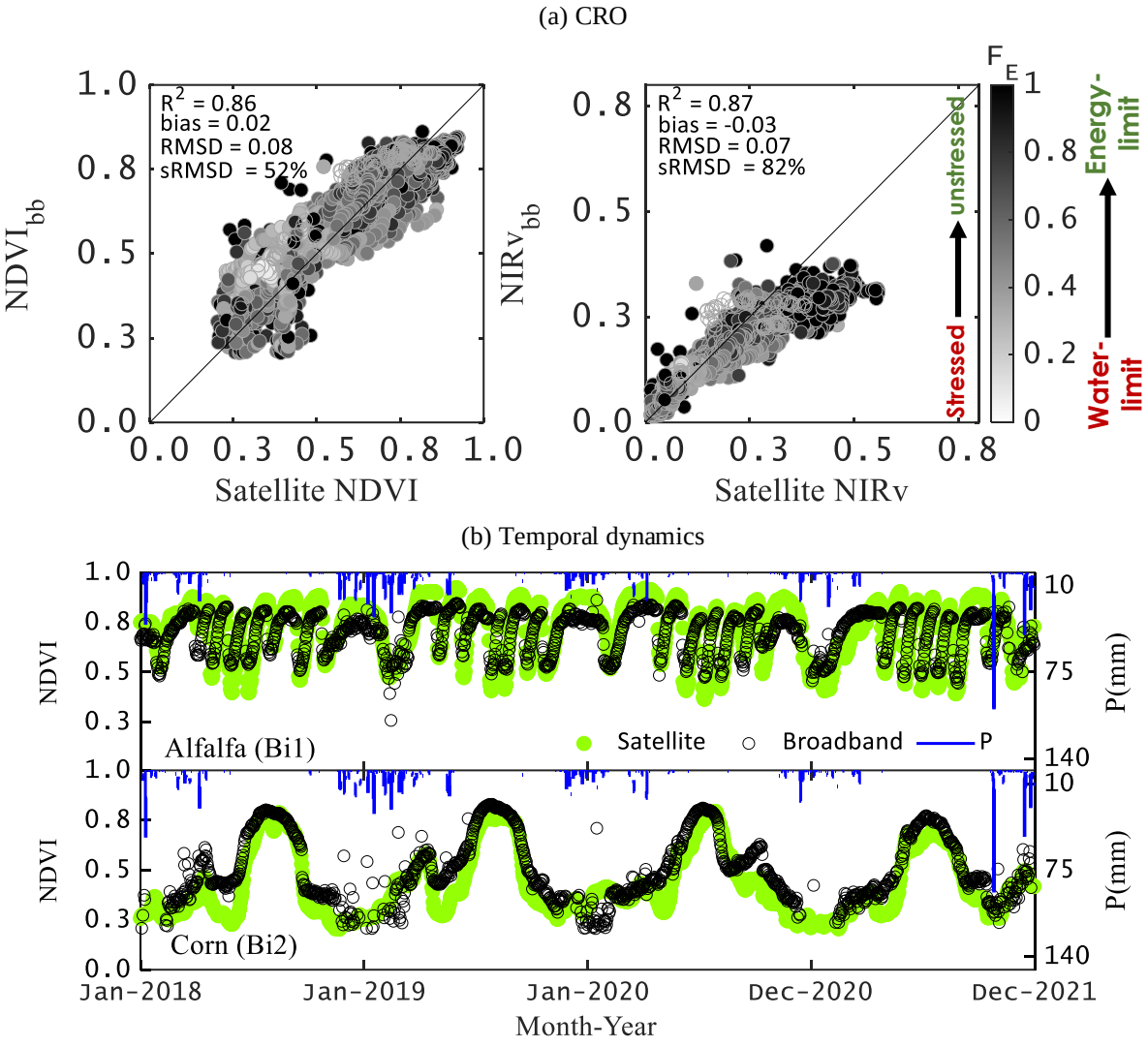

Figure 3: (a) Plots of $NDVI_{bb}$ and $NIRv_{bb}$ versus Planet Fusion NDVI and NIR_V (3 m spatial resolution) in the Californian cropland ecosystems for NDVI>0.25 for a range of evaporative fraction (F_E) representing stressed to unstressed conditions. F_E is an indicator of water availability and denotes the ratio of evaporation (latent heat flux) to equilibrium evaporation. (b) Temporal dynamics of $NDVI_{bb}$ (black dots) and NDVI (green dots) along with daily precipitation (P) (blue stairs) shows close correspondence between them in Alfalfa [Bi1] and Corn [Bi2].

Same analysis by combining data of grassland (GRA) and woody savanna (WSA) sites revealed low range of NDVI in both the datasets with low mean 0.44 – 0.48 and median 0.43 – 0.50 as compared to CRO (mean 0.57 – 0.61 and median 0.58 – 0.63). Due to the

strong water limitations, these ecosystems very rarely form a closed canopy cover, ultimately leading to low mean NDVI. The goodness of fit of linear regression revealed $NDVI_{bb}$ to explain 47% of the variation of Planet Fusion NDVI (R^2 = 0.47) (**Fig. 4a**), which is substantially lower as compared to CRO. Consequently, bias and RMSD was also higher (0.04 and 0.11) than the croplands (**Fig. 4a**). Some exceptionally high magnitude of $NDVI_{bb}$ was evident at low satellite NDVI (0.3 – 0.5), which corresponded to unstressed conditions in GRA-WSA (**Fig. 4a**).

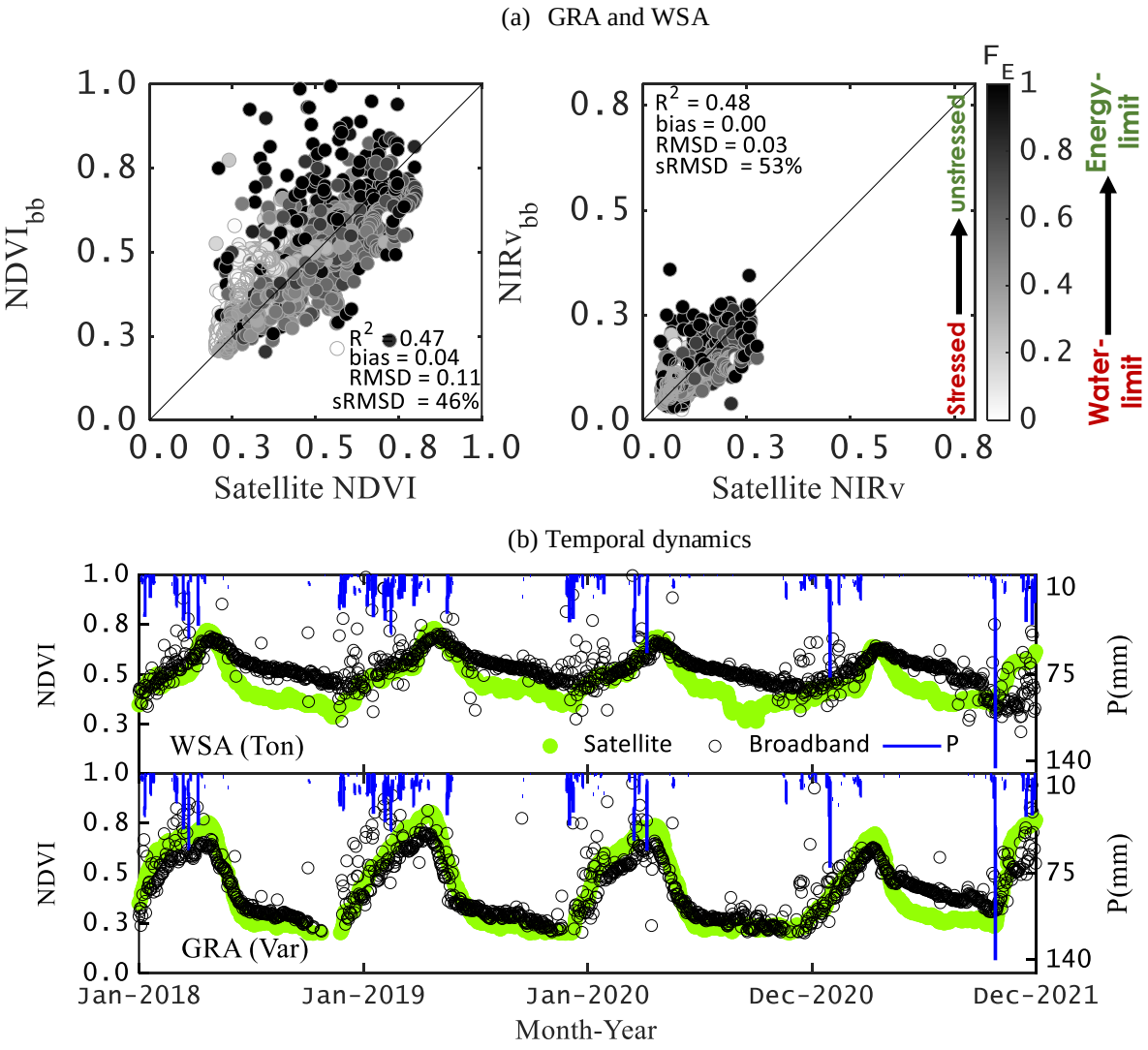

Figure 4: (a) Plots of $NDVI_{bb}$ and $NIRv_{bb}$ versus Planet Fusion NDVI and NIR_V (3 m spatial resolution) in water-limited Californian grassland (GRA) and woody savanna (WSA) ecosystems for NDVI>0.25 for a range of

evaporative fraction (F_E) representing stressed to unstressed conditions. F_E is an indicator of water availability and denotes the ratio of evaporation (latent heat flux) to equilibrium evaporation. (b) Temporal dynamics of $NDVI_{bb}$ (black dots) and NDVI (green dots) along with daily precipitation (P) (blue stairs) shows close correspondence between them especially in the grassland [Var] and partly in woody savanna [Ton].

In comparison to CRO and GRA-WSA, scatterplot of $NDVI_{bb}$ versus Planet Fusion NDVI at the wetland (WET) sites revealed relatively lesser spread (**Fig. 5a**) with a mean and median of 0.51 – 0.52, respectively. $NDVI_{bb}$ explains 66% of the variations in Planet Fusion NDVI (R^2 = 0.66), with a relatively low bias (-0.01), RMSD (0.06) and sRMSD (17%) for the entire range of available energy and limits. The seasonal dynamics of daily $NDVI_{bb}$ at the representative sites (**Fig. 3b, 4b, 5b**) revealed a close resemblance with satellite NDVI for the respective tower pixel at almost all the sites, except at the WSA (Tonzi ranch) (**Fig. 4b**). Despite the rising and falling behavior of $NDVI_{bb}$ was well coordinated with the satellite NDVI at WSA, substantial differences between $NDVI_{bb}$ and Planet Fusion NDVI is also evident as the magnitude NDVI declined with the progression of summer (**Fig. 4b**). This implies that $NDVI_{bb}$ could not efficiently capture the very low NDVI magnitude of the open canopy architecture at woody savanna during the water stressed summer months.

(a) WET

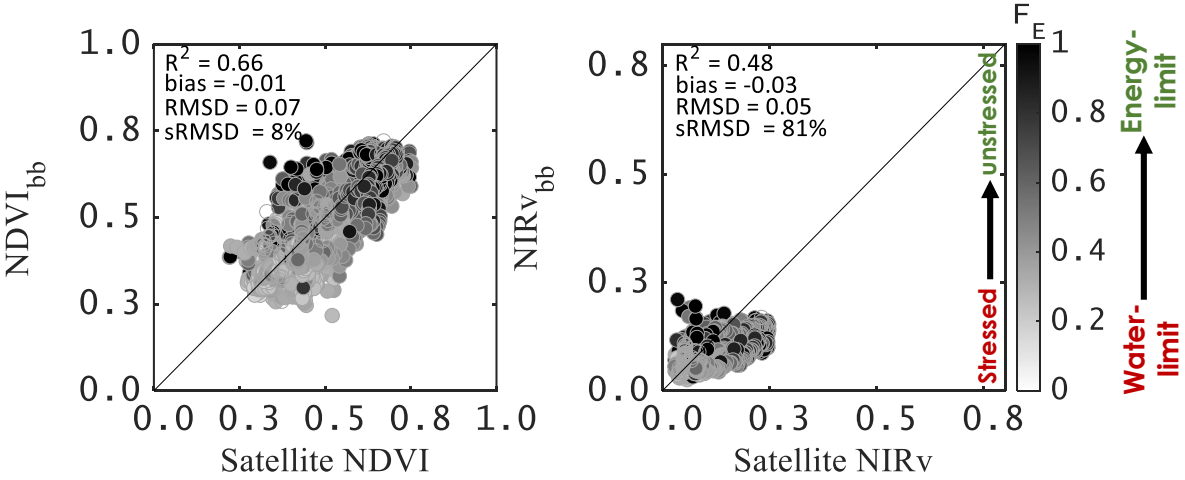

(b) Temporal dynamics

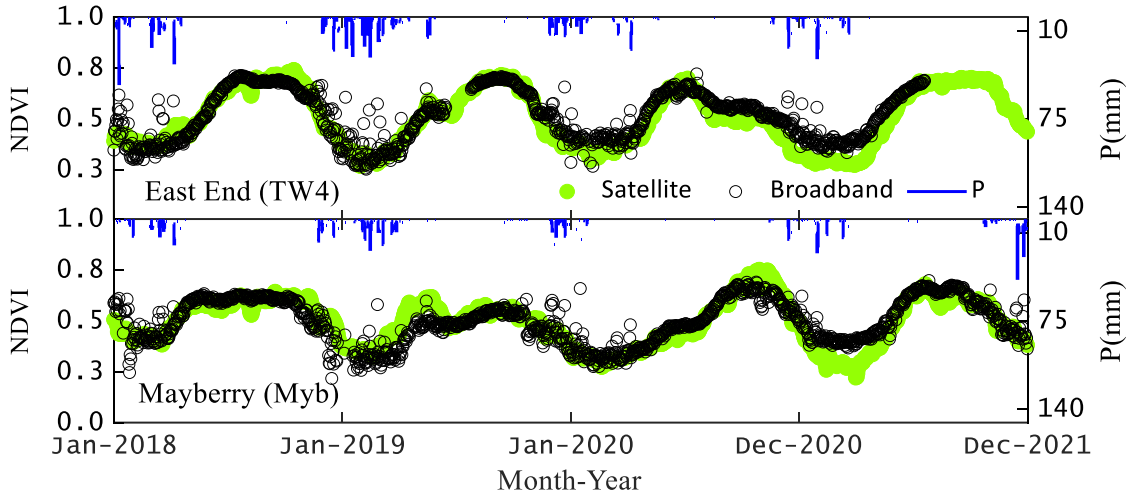

Figure 5: (a) Plots of $NDVI_{bb}$ and $NIRv_{bb}$ versus Planet Fusion NDVI and NIR_V (3 m spatial resolution) in Californian wetland ecosystems (non-tidal) for NDVI>0.25 for a range of evaporative fraction (F_E) representing stressed to unstressed conditions. F_E is an indicator of water availability and denotes the ratio of evaporation (latent heat flux) to equilibrium evaporation. (b) Temporal dynamics of $NDVI_{bb}$ (black dots) and NDVI (green dots) along with daily precipitation (P) (blue stairs) shows close correspondence between them in both East End and Mayberry.

Comparison of $NIRv_{bb}$ versus satellite NIRv revealed $NIRv_{bb}$ to explain 48 – 87% variation in satellite NIRv (R^2 varying from 0.48 – 0.87; mean R^2: 0.79) (**Fig. 3a, 4a, 5a, 6**), RMSD (varying from 0.02 – 0.09; mean RMSD: 0.05), and sRMSD (varying from 35 – 92%; mean sRMSD: 70%) for a broad range of F_E. A distinct saturation in $NIRv_{bb}$ signal around $NIRv_{bb}$> 0.3 and asymptotic behavior in $NIRv_{bb}$ was evident in CRO and WET with increasing satellite NIRv. While this saturation of $NIRv_{bb}$ corresponded to high F_E (>0.7) **(Fig. 3a**) at the CRO sites, the saturation of $NIRv_{bb}$ corresponded to both high and low F_E at the WET sites (**Fig. 5a**). Nevertheless, by combining data of all the sites, the overall performance of $NDVI_{bb}$ and NIR_{Vbb} appeared to be stable (**Fig. 6**). The range of $NDVI_{bb}$ and NIR_{Vbb} obtained from the net fluxes of PAR and R_G are comparable with the magnitude and dynamics of satellite NDVI and NIR_V within and across different ecosystems falling under the same climatic setting.

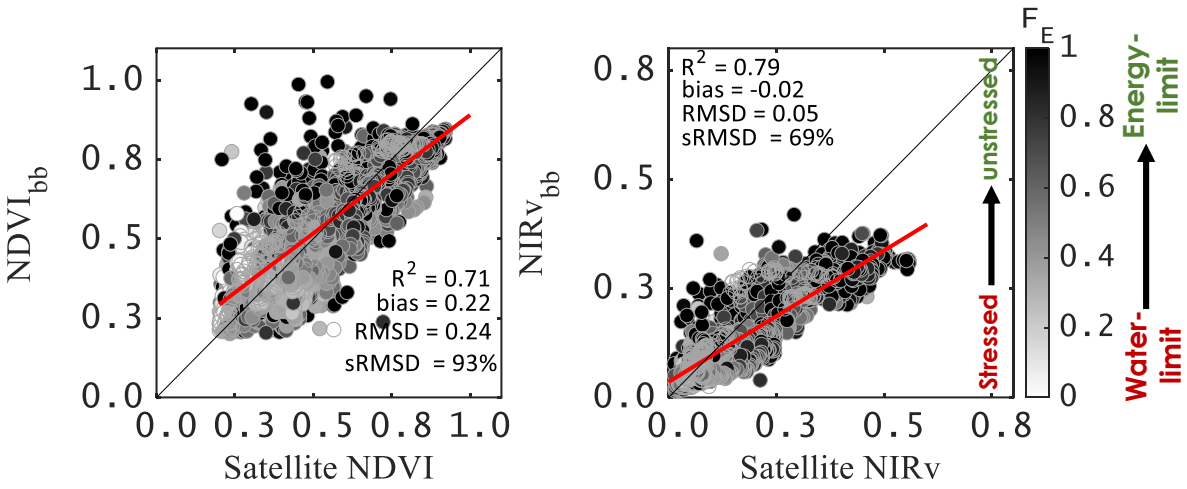

Figure 6: Pooled evaluation plots of $NDVI_{bb}$ and $NIRv_{bb}$ versus Planet Fusion NDVI and NIR_V (3 m spatial resolution) by combining all the seven sites of Californian ecosystems for a range of evaporative fraction (F_E) representing stressed to unstressed conditions. F_E is an indicator of water availability and denotes the ratio of evaporation (latent heat flux) to equilibrium evaporation.

Landsat & Sentinel evaluation: Analysis of $NDVI_{bb}$ and $NIRv_{bb}$ derived from Q^i and Q^r measurements in all 25 sites with respect to HLS NDVI and NIR_V provided another assessment of $NDVI_{bb}$ and $NIRv_{bb}$ in energy- and water-limited environments across diverse ecosystems. Our analysis revealed that $NDVI_{bb}$ consistently captured the variations in NDVI when compared with both L8/9 and S2 sensors (**Fig. 7; Fig. 8**). While the mean and median $NDVI_{bb}$ at the energy-limited ecosystems was found to be 0.56 (0.52 for HLS) and 0.59 (0.53 for HLS), these metrics were 0.41 (0.34 for HLS) and 0.38 (0.31 for HLS) in the water-limited ecosystems. Four distinct features are notable from this analysis. Firstly, the scatterplots of $NDVI_{bb}$ versus satellite NDVI showed significant spread in the energy-limited ecosystems for both L8/9 and S2 across the entire range of F_E (**Fig. 7a, c**). Secondly, the statistical metrics of $NDVI_{bb}$ with respect to NDVI were very similar across the sensors, with higher coefficient of determination for S2 (R^2 = 0.59) as compared to L8/9 (R^2 = 0.43) and lower systematic difference in L8/9 as compared to S2 (**Fig. 7a, c**).

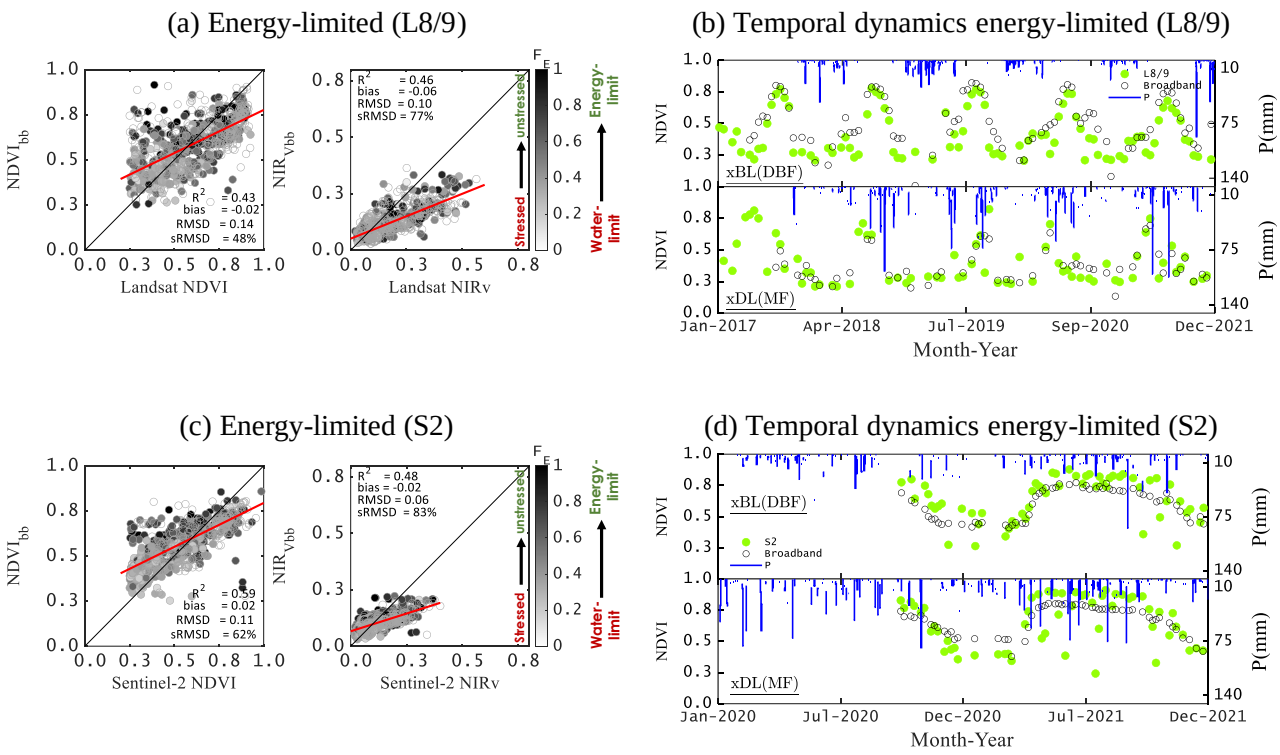

Figure 7: (a, c) Plots of $NDVI_{bb}$ and NIR_{Vbb} versus Landsat and Sentinel-2 NDVI and NIR_V (30 m spatial resolution) in energy-limited ecosystems of Biomet and NEON sites. Color shading is done by evaporative fraction (F_E) showing stressed to unstressed conditions which corresponds to water and energy limits within the energy-limited environment. (b, d) Illustrative examples of temporal dynamics of $NDVI_{bb}$ (black dots) and NDVI (green dots) along with daily precipitation (P) (blue stairs) showing close correspondence in the seasonal and interannual variability of $NDVI_{bb}$ and NDVI at the NEON sites Blandy Experimental Farm (xBL) and Dead Lake (xDL).

Thirdly, the agreement between $NDVI_{bb}$ versus satellite NDVI and $NIRv_{bb}$ versus satellite NIR_V was much stronger (with less systematic difference) in the water-limited ecosystems (R^2 = 0.59 – 0.66 and 0.69 – 0.74; sRMSD: 33 - 42% and 49 - 54%) as compared to energy-limited ecosystems (R^2 = 0.44 – 0.49 and 0.41 – 0.46; sRMSD: 48 - 57% and 76 - 77%). Fourthly, a marked asymptotic pattern and saturation in $NIRv_{bb}$ was evident with increasing satellite NIR_V (>0.3) (**Fig. 7a, c; Fig. 8a, c**) in both the climatic limits. This resulted in large differences and high RMSD between $NIRv_{bb}$ versus satellite NIR_V across the entire range of F_E. The seasonal dynamics of $NDVI_{bb}$ at the representative cropland and grassland sites in the water-limited ecosystems revealed a close resemblance with satellite NDVI for the respective tower pixel at each site (**Fig. 8b,**

551 **d**). A detailed description of ecosystem wise analysis by combining data of both L8/9 and

552 S2 is given in **Appendix A1**, **Fig. A1**, **Table A1** (for L8/9) and **Table A2** (for S2),

553 respectively.

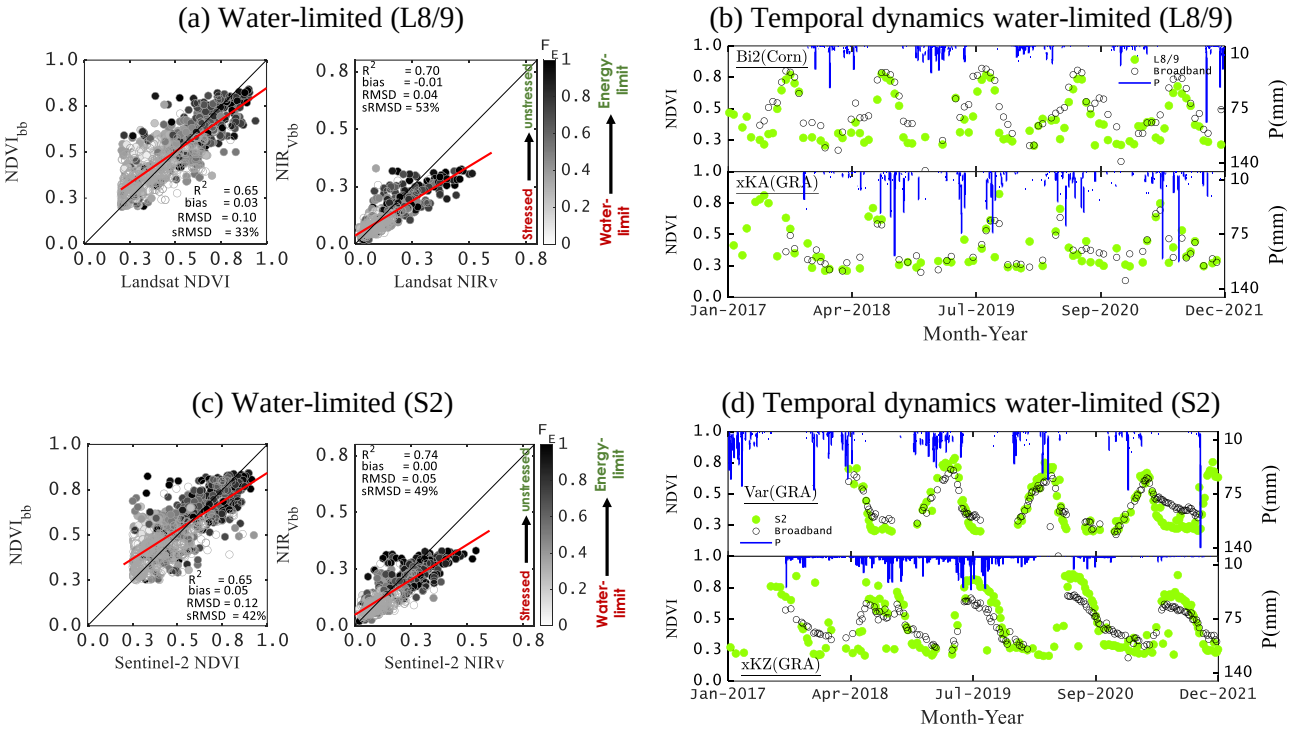

Figure 8: (a, c) Plots of $NDVI_{bb}$ and NIR_{Vbb} versus Landsat and Sentinel-2 NDVI and NIR_V (30 m spatial resolution) in water-limited ecosystems of Biomet and NEON sites. Color shading is done by evaporative fraction (F_E) showing stressed to unstressed conditions which corresponds to water and energy limits within the water-limited environment. (b, d) Illustrative examples of temporal dynamics of $NDVI_{bb}$ (black dots) and NDVI (green dots) along with daily precipitation (P) (blue stairs) showing close correspondence in the seasonal and interannual variability of $NDVI_{bb}$ and NDVI over Bouldin corn (Bi2), Vaira ranch (Var) and two grasslands sites of NEON Konza Prairie Biological Station (xKA and xKZ).

554 To understand the explanatory potential of $NDVI_{bb}$ in tracking the variation in LAI, we

555 also analyzed $NDVI_{bb}$ with respect to continuous LAI observations at the Tonzi ranch site

556 (detailed explanations are in **Appendix A2**; **Fig. A2**).

557 It is further important to emphasize that in the comparisons between broadband versus

558 satellite NDVI, we do not expect to see an ideal 1:1 relationship. Discrepancies between

559 these two indices could arise, (i) due to the differences in bandwidths for the bands used

in satellite and broadband vegetation indices and (ii) due to comparing broadband hemispherical reflectance derived through proximal sensing versus directional narrowband reflectance from remote sensing. The effects of these two important aspects are demonstrated and discussed in detail in section 3.4.

3.2. Mean seasonal variability of broadband NDVI with phenology and vegetation function (SQ2)

This section examines the mean seasonal variability of $NDVI_{bb}$ along with satellite NDVI, a phenological metric namely Green Chromatic Coordinate (GCC), and their response to water stress (evaporative fraction, F_E). (**Fig. 9, 10**). This analysis is based on the continuous time series information of $NDVI_{bb}$, Planet Fusion NDVI, and UC Berkeley Biomet lab flux tower datasets. The reasons to use Planet Fusion data are that firstly they are finely resolved in time to allow for filtering day-to-day variability and secondly, they span over a period of four years to allow investigating the mean seasonal variations. **Figure 9** shows the synthesis of the mean seasonal variation of $NDVI_{bb}$, NDVI, GCC, and F_E for the two cropland ecosystems (alfalfa and corn) in California. The seasonal variation is expressed in terms of the daily mean values normalized by their annual mean following Baldocchi et al. (2021).

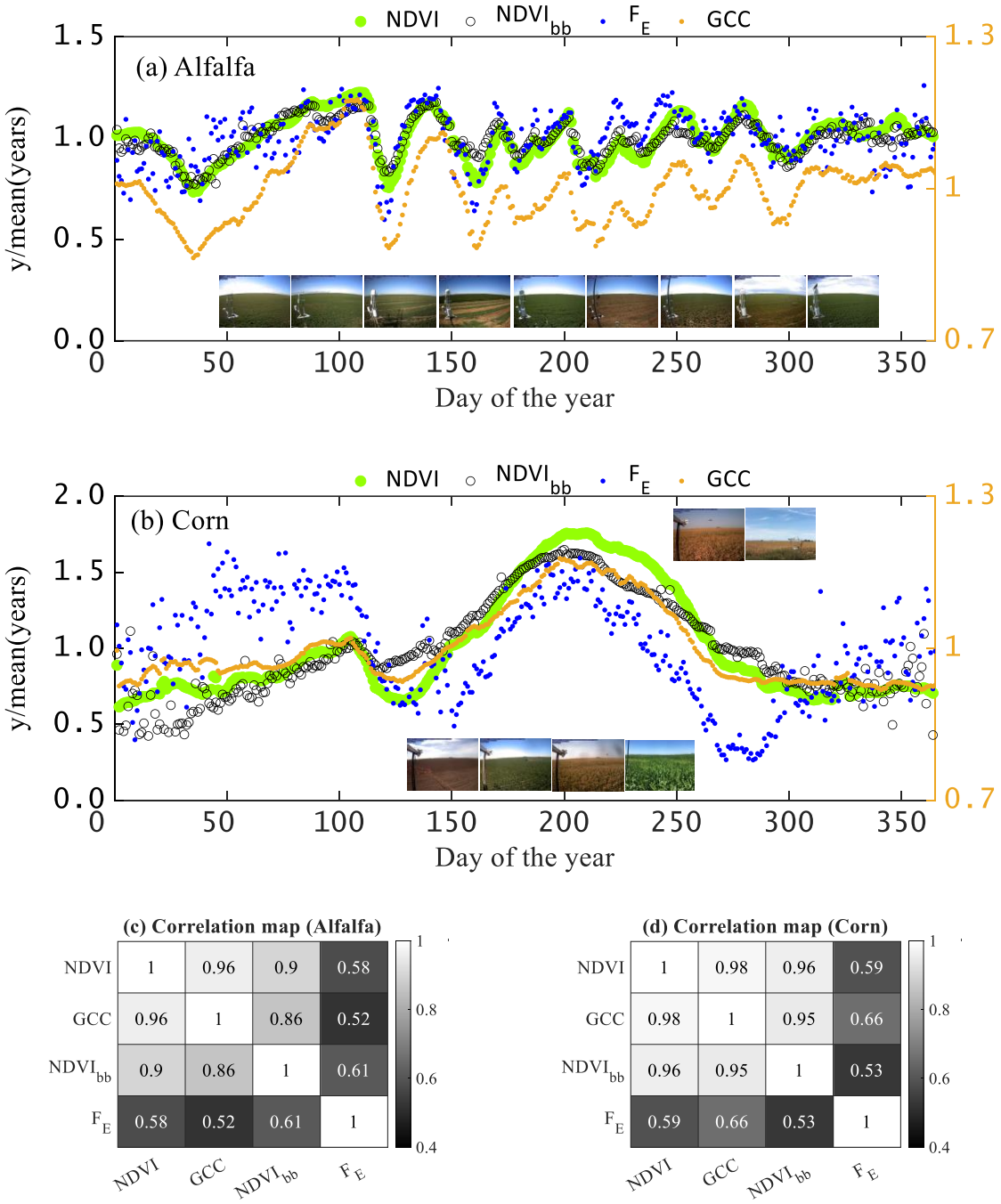

Figure 9: (a-b) Daily variation in $NDVI_{bb}$, Planet Fusion NDVI, Green Chromatic Coordinate (GCC) (secondary y-axis), and evaporative fraction (F_E) over agricultural ecosystems (alfalfa and corn) in California. Here we plot daily values, averaged over 4 years, normalized by the annual mean for that variable. (c-d) Correlation map showing the strength of seasonal relationship between individual variables. For corn, the correlation map is applicable for the growing season from March to September.

577 Two things became evident in this analysis. (i) The coordination of $NDVI_{bb}$ and satellite

578 NDVI was found to be remarkably high with GCC at alfalfa throughout the entire year

(**Fig. 9a, c**). The coordination of the two NDVIs with GCC was also substantially strong in corn from the start of the growing season (day of the year 120), green-up phase (day of the year 150 – 180), peak growth phase (day of the year 180 – 250) and until the end of the growing season (day of the year 250 – 300) (**Fig. 9b, d**). (ii) The response of both the NDVIs and GCC is also highly correlated with F_E at the alfalfa site (**Fig. 9a, c**) (r = 0.52 – 0.61), and their responses to F_E were also very robust in corn during the annual growth cycle that spans from day of the year 120 to 300 (**Fig. 9d**) (r = 0.53 – 0.66). This indicates substantial controls of water availability on the growth dynamics of both alfalfa and corn. Peak daily $NDVI_{bb}$ (and NDVI) and GCC coincided when F_E is greater than their mean annual values (**Fig. 9b**).

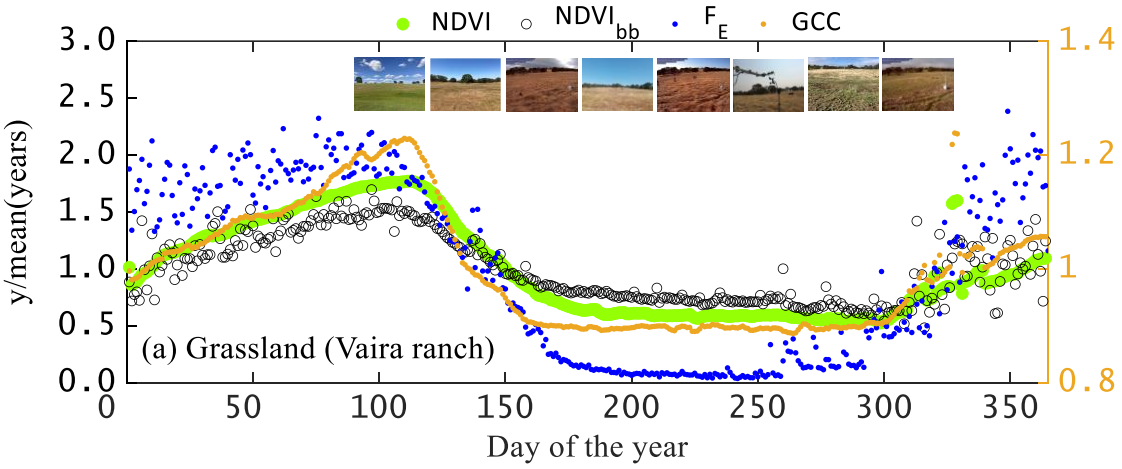

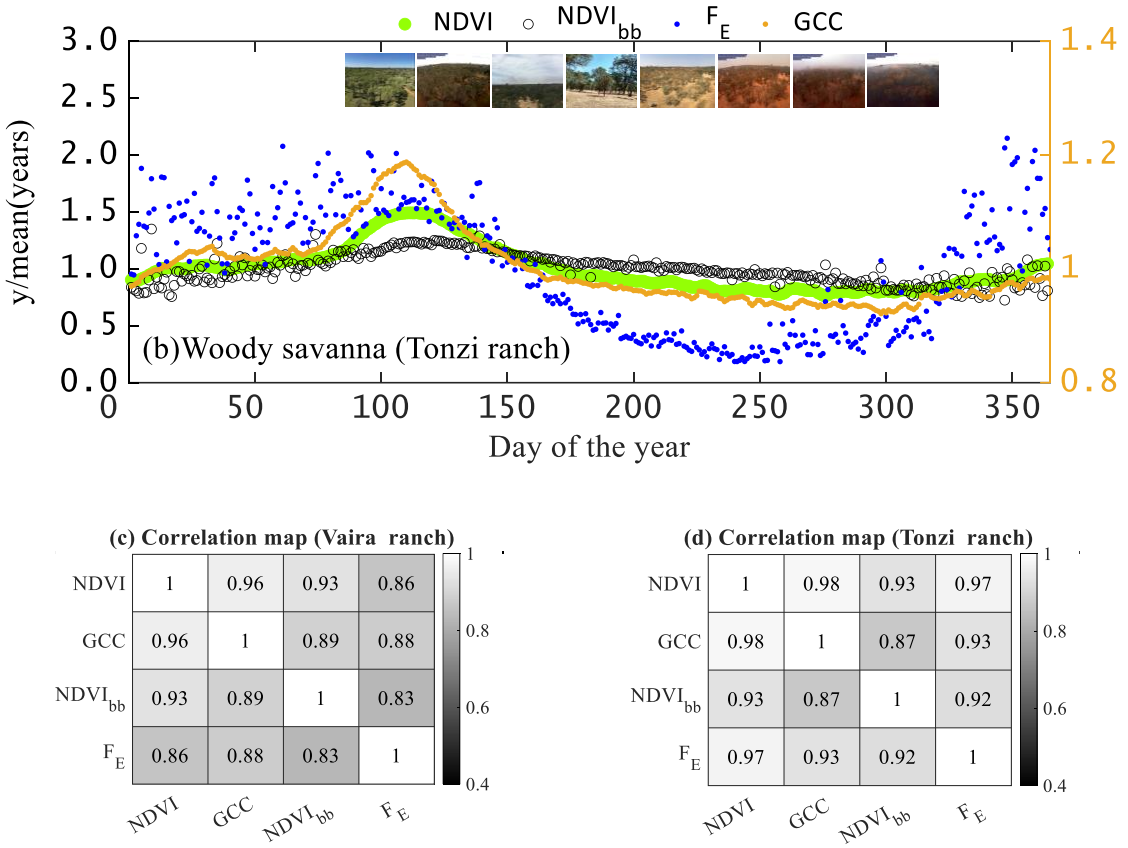

Figure 10: (a-b) Daily variation in $NDVI_{bb}$, Planet Fusion NDVI, Green Chromatic Coordinate (GCC) (secondary y-axis), and evaporative fraction (F_E) over grassland (Vaira ranch) and woody savanna (Tonzi ranch) ecosystems in California. Here we plot daily values, averaged over 4 years, normalized by the annual mean for that variable. (c-d) Correlation map showing the strength of seasonal relationship between individual variables during the growing season from March to October.

Figure 10 shows the synthesis of the mean seasonal variation of $NDVI_{bb}$, NDVI, GCC, and F_E at GRA and WSA ecosystems in California. Here also, some distinctive behavior of $NDVI_{bb}$, NDVI and GCC and their response to water stress variations was noted. Firstly, the overall coordination of GCC and NDVIs with F_E was high in both the ecosystems (r = 0.83 – 0.88 and r = 0.93 – 0.97) and the coordination strength of NDVI versus GCC was equally high (r = 0.83 – 0.96 and r = 0.87 – 0.98). Secondly, the coordination strength between the two NDVIs versus water availability in GRA and WSA is substantially higher as compared to the croplands (**Fig. 10c, d**). In both the ecosystems, peak daily $NDVI_{bb}$ (and NDVI) and GCC coincided when F_E is greater than

598 their mean annual values (**Fig. 10a, b**). The maximum NDVI and GCC was found in
599 early spring (day of year 120) during the unstressed conditions. After that, the two
600 NDVIs started declining with F_E and it reached the minimum during the middle of the
601 summer, between days 170 and 250. Interestingly, despite the declining pattern of GCC
602 was very similar to NDVI in WSA, it remained invariant in GRA between days 150 and
603 300. This is the period when the soil remains nearly bone dry due to prolong absence of
604 precipitation. The coalition of high soil water stress and atmospheric aridity (as defined
605 by vapor pressure deficit) in association with high net available energy triggers the
606 stomatal closure and consequently the photosynthetic activity is at the minimum level.

607 It is further important to emphasize that croplands receive subsurface irrigation at a depth
608 of 2 m and the irrigation frequency is very low. While corn receives a single irrigation
609 (around day of the year 230), alfalfa receives maximum 2 irrigation (around day of the
610 year 160 and 180; 240 and 260). The atmospheric humidity over cropland is higher (as
611 compared to GRA and WSA) due to being situated close to the delta shores of
612 Sacramento and due to moisture advection (Wang et al., 2023). All these factors lead to
613 an increased evaporative fraction, and vegetation seasonality responds significantly to F_E
614 dynamics. On the contrary, being situated at the valley, GRA and WSA sites face dual
615 challenge due to high soil and atmospheric water stress. The different NDVI, $NDVI_{bb}$ and
616 GCC profiles for these two ecosystems indicate that the vegetation seasonality in GRA
617 and WSA has a stronger coupling to the seasonality in water stress as compared to the
618 croplands, despite being situation in the same Mediterranean climate.

3.3. Efficacy of $NDVI_{bb}$ and NIR_{Vbb} to explain GPP variability (SQ3)

This analysis is carried out into two halves. In the first step, we examined whether the intraseasonal variability (expressed as 'coefficient of variation', cv) of $NDVI_{bb}$ and NIR_{Vbb} can explain the intraseasonal variability of GPP (symbolized as A_G). In the second step, we tested the robustness and feasibility of using daily $NDVI_{bb}$ and NIR_{Vbb} as a robust predictor of daily GPP. Here also, we used the continuous time series EC tower GPP record of seven Biomet lab sites and the Planet Fusion data. The reasons to use PLANET Fusion data is the same as mentioned in section 3.2.

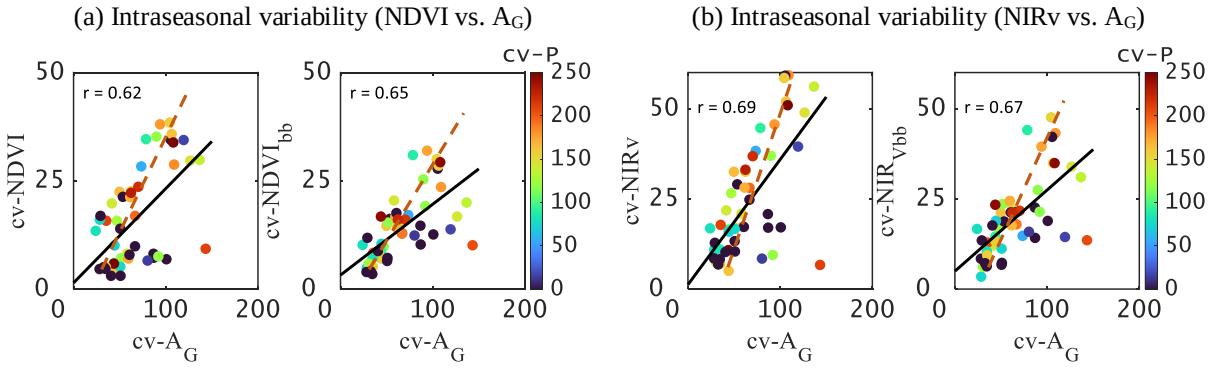

Figure 11: (a-b) Plots of intraseasonal variability (expressed as 'coefficient of variation', cv) in NDVI ($NDVI_{bb}$) and NIR_V (NIR_{Vbb}) versus intraseasonal variability in gross photosynthesis (A_G) by combining all the site data in different ecosystems of California. Color shading is by precipitation (P) variability. This also shows the steeper slope of cv-NDVI (and cv-$NDVI_{bb}$) vs. cv-A_G and cv-NIR_V (and cv-NIR_{Vbb}) vs. cv-A_G relationship with increasing precipitation variability.

Combining data of all the seven Biomet sites showed a relatively stronger relationship between NIR_V (NIR_{Vbb}) variability with GPP variability (r = 0.67 – 0.69) as compared to NDVI ($NDVI_{bb}$) (r = 0.62 – 0.65) (**Fig. 11a, b**). The intraseasonal variability of the two NDVIs versus GPP and two NIR_V versus GPP relationship was also found to be strongly associated with the rainfall variability during the growing season in CRO, GRA, and WSA (Appendix A3, **Fig. A3**). Previous studies also showed the tendency of the water-limited ecosystems towards higher interannual variability in vegetation productivity (Ritter et al., 2020). The high water use efficiency of cropland, grassland, and savanna

plays a major role. During the pluvial years or wet seasons, water infiltration into deep soil layers compensates for the preceding water deficit (Ritter et al., 2020), increasing the soil water content available for transpiration and biomass production for the following months. This leads to an increased productivity during high rainfall years relative to their reduction during the dry years (Ritter et al., 2020). Similar mechanism is also reflected in these two vegetation indices through efficient vegetation greening as a result of optimum vegetation productivity. This led to steeper slopes between the coefficient of variation of these two vegetation indices (both broadband and satellite) versus the coefficient of variation of GPP (cv-A_G) with increasing precipitation variability when all the data were pooled together (**Fig. 11**).

(a) A_G vs. $NDVI_{bb}$

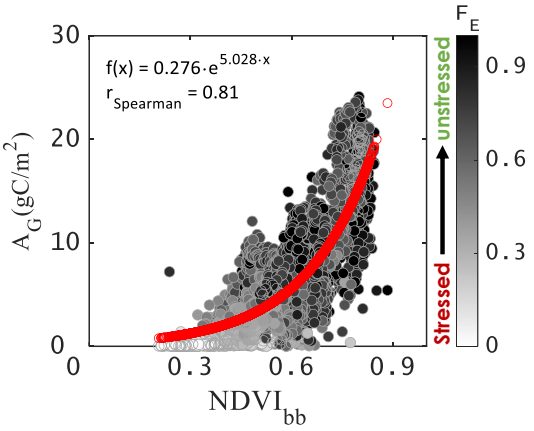

(b) A_G vs. $NIRv_{bb}*\Sigma Q^i$

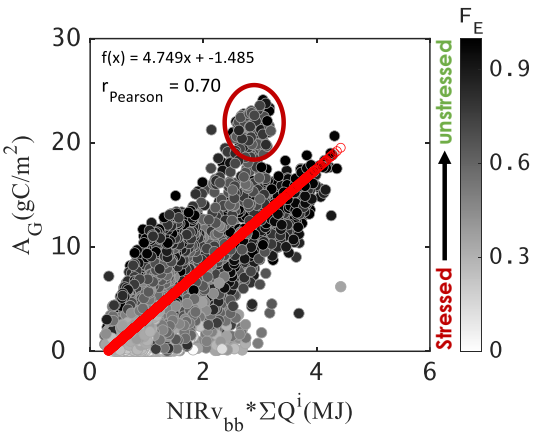

(c) A_G vs. NDVI (Planet Fusion)

(d) A_G vs. $NIRv*\Sigma Q^i$ (Planet Fusion)

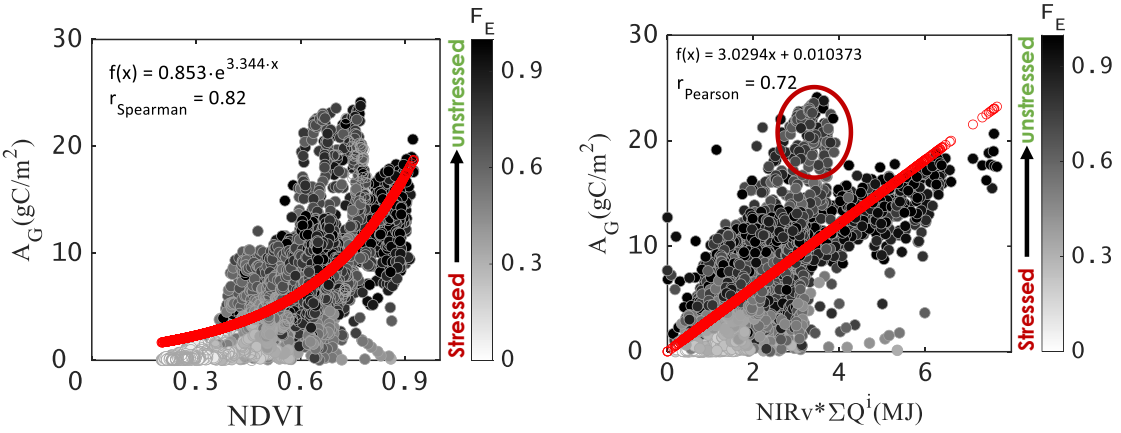

(e) A_G vs. $NDVI_{bb}^2$*ΣQ^i

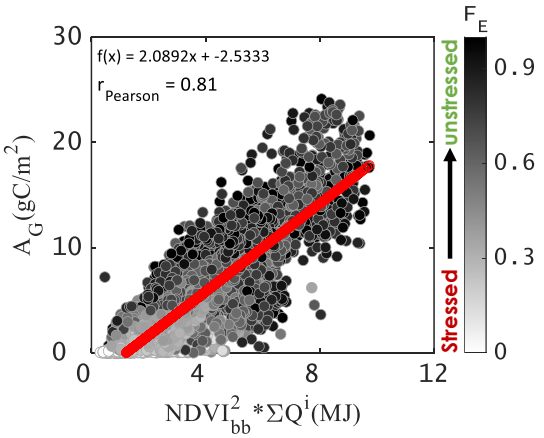

Figure 12: (a, b) Site-level relationships of A_G versus $NDVI_{bb}$ and A_G versus $NIRv_{bb}$*ΣQ^i at seven eddy covariance towers of UC Berkeley Biomet sites that includes 2 crop sites (one C4, one C3), one grassland site, one woody savanna and 3 wetland sites. (c, d) Similar plot is shown by plotting A_G with Planet Fusion NDVI and $NIRv_{bb}$*ΣQ^i. Here ΣQ^i and A_G are the daily integrated Q^i (MJ) and A_G (gC/m^2) obtained by summing up the half-hourly observation. Data points inside the red circle showed saturation in A_G with increasing $NIRv_{bb}$*ΣQ^i. These data points belong to corn crop and could presumably be associated with the diffuse component of Q^i. (e) Scatter plot of A_G versus $NDVI_{bb}^2$*ΣQ^i.

By combining the Planet Fusion and EC data of all the seven Biomet lab sites, we found a distinct exponential pattern between flux tower GPP and $NDVI_{bb}$ (**Fig. 12a**) with Spearman's correlation ($r_{Spearman}$) of 0.79. This further confirms that NDVI saturates at high biomass and this saturation is mainly attributed to the insensitivity of chlorophyll absorbing red light at 100% vegetation cover (Sellers et al., 1985; Kumar et al., 2001). Any addition of vegetation does not impact further changes since the amount of red light that can be absorbed by leaves reaches a peak, whereas NIR reflectance will increase because an addition of leaves results in multiple scattering (Tesfaye and Awoke, 2020; Kumar et al., 2001). The imbalance between red and high NIR reflectance results in a marginal change in the NDVI ratio and yields saturation at high biomass. Given the

product of NIRv and incident PAR (Q^i) is considered as a proxy for GPP at different spatial scales (Dechant et al., 2022), we further evaluated the relationships between GPP versus the product of $NIRv_{bb}$ and daily integrated PAR ($NIRv_{bb}*\sum Q^i$). We found a strong and significant correlation between A_G versus $NIRv_{bb}*\sum Q^i$ (r = 0.68) (**Fig. 12b**). Despite substantial linearity between A_G versus $NIRv_{bb}*\sum Q^i$ relationship, a small portion of data points (inside red circle) showed saturation in A_G with increasing $NIRv_{bb}*\sum Q^i$ (**Fig. 12b**). These data points belong to corn and could presumably be associated with the diffuse component of Q^i. The scatterplots of flux tower A_G versus Planet Fusion NDVI and the product of $NIRv*\sum Q^i$ also showed the same exponential and linear pattern and very similar correlation ($r_{Spearman}$= 0.81 and $r_{Pearson}$ = 0.70) (**Fig. 12c, d**). These results corroborate with the findings of Pierrat et al. (2022), Gamon et al. (1995), and Liu et al. (2021) which showed that NDVI is insensitive to maximum carbon uptake in evergreen trees and reported the similar pattern of saturation as we found in **Fig. 12a**. However, where canopy structure, PAR, and carbon uptake are in synchrony, NDVI was found to be significantly correlated with gross photosynthesis (Gamon et al., 1995, Liu et al., 2021). The $NIRv_{bb}*\sum Q^i$ approach constituted a nonlinear stretch of $NDVI_{bb}$ by multiplying $NDVI_{bb}$ with the NIR reflectance, thereby increasing the sensitivity of $NIRv_{bb}*\sum Q^i$ for high vegetation carbon uptake and green biomass. $NIRv_{bb}$ implicitly assumes a linear relationship between $NDVI_{bb}$ and fractional absorbed PAR, and this fraction is 100% at maximum $NDVI_{bb}$. Therefore, multiplying $NIRv_{bb}$ by $\sum Q^i$ gives a close estimate of absorbed PAR, and we see a good relationship with gross primary productivity. Although the scatterplot of A_G versus Planet Fusion $NIRv*\sum Q^i$ shows a tendency to saturate at high A_G (**Fig. 12d**), overall $NIRv_{bb}*\sum Q^i$ approach reflects much

better fidelity to capture the variability in carbon fluxes (Baldocchi et al., 2020; Dechant et al., 2022).

The relationship between A_G versus $NIRv_{bb}*\sum Q^i$ has a physical basis and it is analogous to the classic light use efficiency (LUE) approach of Monteith (1972), Gitelson and Gamon (2015). According to Monteith (1972), Gitelson and Gamon (2015), GPP = LUE*$\sum$APAR, where APAR is the absorbed PAR. From this analogy, NIRv seems to carry the dual information of absorbed PAR and LUE. While high (low) GPP is the consequence of high (low) absorbed PAR, NIRv is the consequence of multiple reflection in the near infrared reflectance which increases with vegetation layer. Therefore, $NIRv_{bb}*\mathbf{\Sigma}Q^i$ has a clear upper and lower bound to explain the GPP variability for a wide range of vegetation and radiation conditions. For example, high GPP during the peak developmental phase of vegetation is due to high absorbed PAR, which apparently leads to high NIRv. On the other hand, during the early growth phase and maturity, we see increasing and declining GPP with increasing and decreasing absorbed PAR and NIRv. Thus, $NIRv_{bb}*\mathbf{\Sigma}Q^i$ is able to separate green from dead vegetation. This is the reason why we found a remarkably good relationship when we plotted daily A_G with $NIRv_{bb}*\mathbf{\Sigma}Q^i$ (**Fig. 12b, d**). One other aspect worth highlighting is that corn is C4 crop and has a complex canopy structure. The fact that our broadband NIRv can capture this so well, further shows the promise of this analysis.

Interestingly, by simply taking the square of NDVI and by multiplying $NDVI^2$ with $\mathbf{\Sigma}Q^i$, we obtained even better correlation ($r_{Pearson}$ = 0.81) between A_G versus $NDVI^2*\mathbf{\Sigma}Q^i$ (**Fig. 12e**) as compared to A_G versus $NIRv_{bb}*\mathbf{\Sigma}Q^i$. The square of NDVI gives an almost

equivalent result as fractional absorbed PAR (Carlson and Ripley, 1997). Then multiplying $NDVI^2$ with $*\Sigma Q^i$, we get an estimate of absorbed PAR, which is why **Fig. 12e** showed strong correlation between A_G and $NDVI^2*\Sigma Q^i$.

It is worth mentioning that in the higher latitude sites, NDVI describes GPP during vegetation green-up when the energy from PAR is generally high (Zhang et al., 2020; Descals et al., 2022). However, NDVI provides little information about GPP in the autumn where photosynthesis is driven by the seasonally decreasing PAR. Therefore, including PAR with $NIRv_{bb}$ could have added advantage in describing the day-to-day variability in GPP during the periods of varying cloudiness where NDVI remains almost invariant (Zhang et al., 2020; Descals et al., 2022).

3.4. Impacts of background soil exposure, phenology, radiation components, and water stress on broadband NDVI (SQ4)

This analysis is categorized into two parts. First, we examined the consequence of background soil exposure and phenology on the estimation of $NDVI_{bb}$. We carried a residual error analysis across different ecosystems where the differences between broadband and satellite NDVI ($\delta_{NDVI} = NDVI_{bb} - NDVI$) were assessed with respect to GCC for a range of Soil Adjusted and Atmospherically Resistant Vegetation Index (SARVI) (**Fig. 13** below). At the second step, we compared the broadband VIS and NIR hemispherical reflectances with satellite narrowband directional reflectance for a large range of incident and reflected radiation components (**Fig. 14 - 16**).

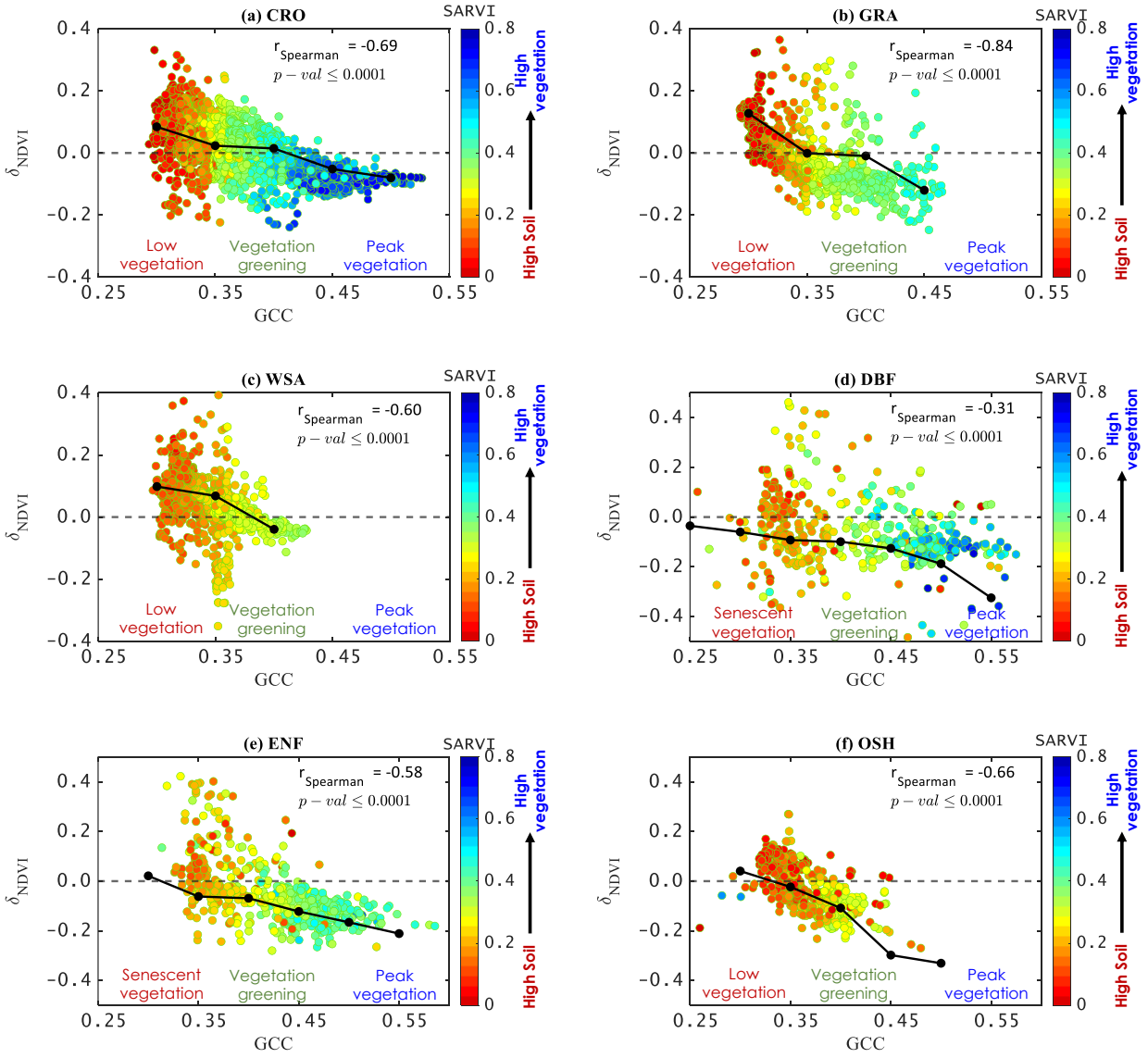

Figure 13: Plots of residual difference between $NDVI_{bb}$ and satellite NDVI (δ_{NDVI} = $NDVI_{bb}$ - NDVI) versus Green Chromatic Coordinate (GCC) for a wide range of soil background conditions across diverse ecosystems. Color shading is by Soil Adjusted and Atmospherically Resistant Vegetation index (SARVI), which serves as an indicator of soil-canopy background. The black line indicates the average bias for each bin. This clearly indicates a consistent positive difference between $NDVI_{bb}$ and satellite NDVI during low vegetation or during vegetation senescence, which also coincides with low SARVI. The black line shows the mean bias pattern for different classes of GCC.

720 The scatterplots of mean δ_{NDVI} clustered for different classes of GCC (from

721 senescence/low vegetation to peak vegetation) showed significant relationships between

722 mean δ_{NDVI} and GCC for varying background from high soil cover to high canopy cover

723 across different ecosystems (r = 0.31 – 0.84) (**Fig. 13**). A consistent positive bias in

$NDVI_{bb}$ (δ_{NDVI} >0) is evident when the vegetation cover is low (low GCC) or during the senescent phase of vegetation (datapoints in red color cluster). The green reflectance contributes very little during senescence and red reflectance has a greater dominance among the three primary band reflectances, ultimately leading to low GCC (0.30<GCC<0.35). Low leaf area during the senescent phase in forests or due to grazing in the grasslands leads to greater exposure of soil background at the field-of-view of the sensors, ultimately reading to high NIR reflectance (Huete et al., 1988; Qi et al., 1994). Spectral reflectance of the canopies is mixed with background reflectance due to multiple scattering in the broad NIR band. Such high NIR reflectance apparently leads to an overestimation of $NDVI_{bb}$ under low vegetation cover. These positive biases in $NDVI_{bb}$ also corresponded to low SARVI (0 – 0.2) (**Fig. 13**), indicating soil background to be exerting considerable influence on the canopy spectra and the calculated $NDVI_{bb}$ (Huete et el., 1988; Qi et al., 1994). This dual assessment of δ_{NDVI} with respect to phenology and soil background variations authenticates the sensitivity of $NDVI_{bb}$ to first-order soil exposure effects.

In the estimation of $NDVI_{bb}$, the consistency of broadband hemispherical VIS and NIR reflectances ($\rho_{vis,bb}$, $\rho_{nir,bb}$) play a crucial role where proximal sensing of R_g (R_g^i, R_g^r) and PAR components (Q^i, Q^r) are used. Therefore, to further understand the effects of background on this overestimation of $NDVI_{bb}$, we compared the performance of $\rho_{vis,bb}$ and $\rho_{nir,bb}$ with respect to satellite narrowband directional reflectances under varying PAR (both Q^i and Q^r) (**Fig. 14 - 16** below). The effects of individual R_g components (R_g^i, R_g^r) on this comparison is very similar to what is seen in **Fig. 14 – 16** and they are not shown for brevity.

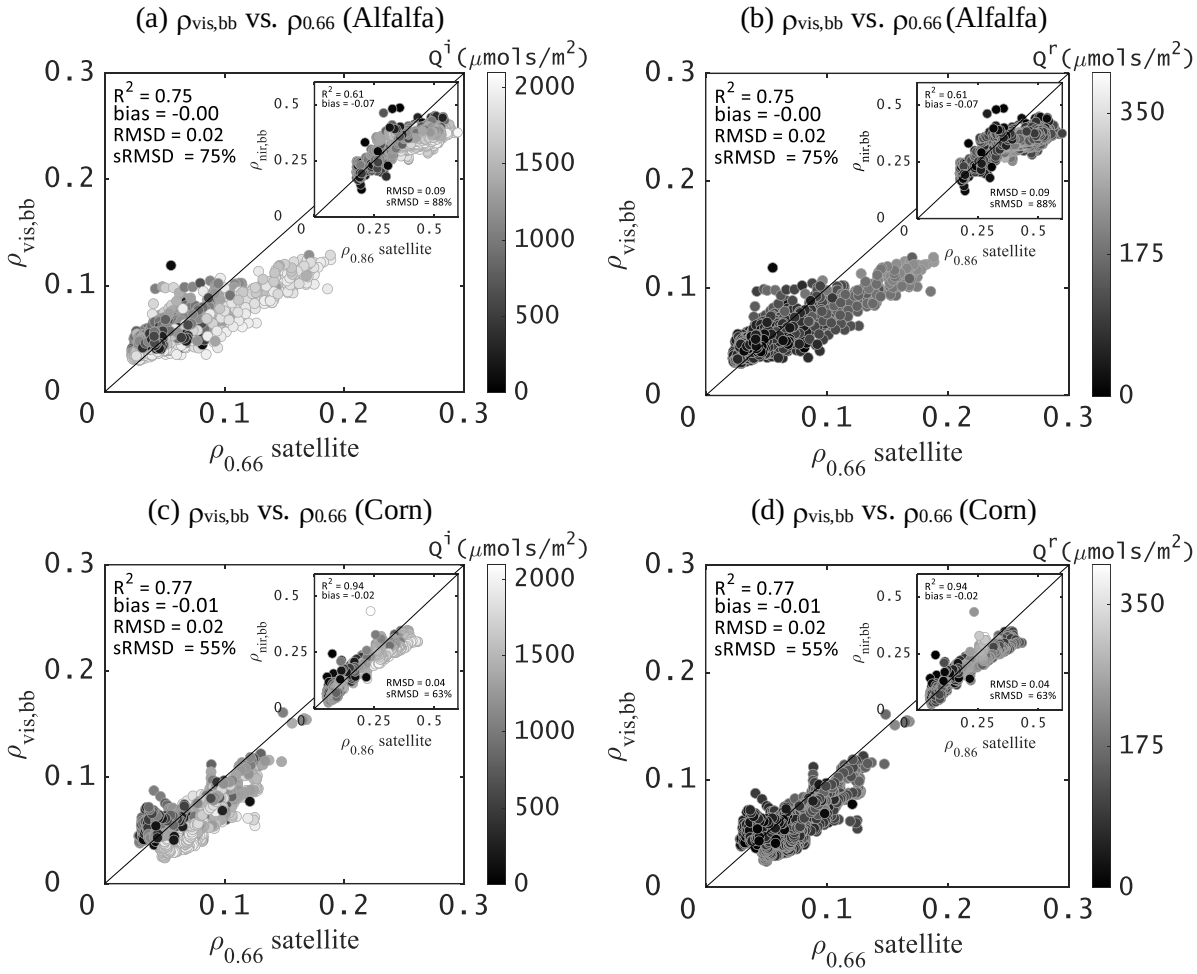

Figure 14: Illustrative examples of comparison between $\rho_{vis,bb}$ versus $\rho_{0.66}$ for a range of incident and reflected PAR (Q^i and Q^r) over alfalfa (a, b) and corn (c, d) in California. This clearly shows a tendency of systematic underestimation of $\rho_{vis,bb}$ with respect to $\rho_{0.66}$, and the underestimation increases at high Q^i and Q^r. Figures in the inset shows a similar comparison between $\rho_{nir,bb}$ versus $\rho_{0.86}$ for a range Q^i and Q^r. This analysis was performed with Planet Fusion data.

747 The spectral reflectance comparison revealed $\rho_{vis,bb}<\rho_{0.66}$ for the majority of the data

748 points and their differences were magnified with increasing Q^i (Q^i>1500 µmols). The

749 effects of high Q^i and Q^r on $\rho_{nir,bb}$ was also visible and $\rho_{nir,bb}>\rho_{0.86}$ at low satellite $\rho_{0.86}$

750 (**inset of Fig. 14 – 16**). This implies that in the estimation of $NDVI_{bb}$ [$NDVI_{bb} = (\rho_{nir,bb} -$

751 $\rho_{vis,bb})/(\rho_{nir,bb} + \rho_{vis,bb})$], there is a consistent overestimation of the numerator ($\rho_{nir,bb} -$

752 $\rho_{vis,bb}>\rho_{0.86} - \rho_{0.66}$) with increasing Q^i under low fractional vegetation cover. This

ultimately led to greater difference between $NDVI_{bb}$ and satellite NDVI (δ_{NDVI} >0) at high Q^i, Q^r, and at high soil background.

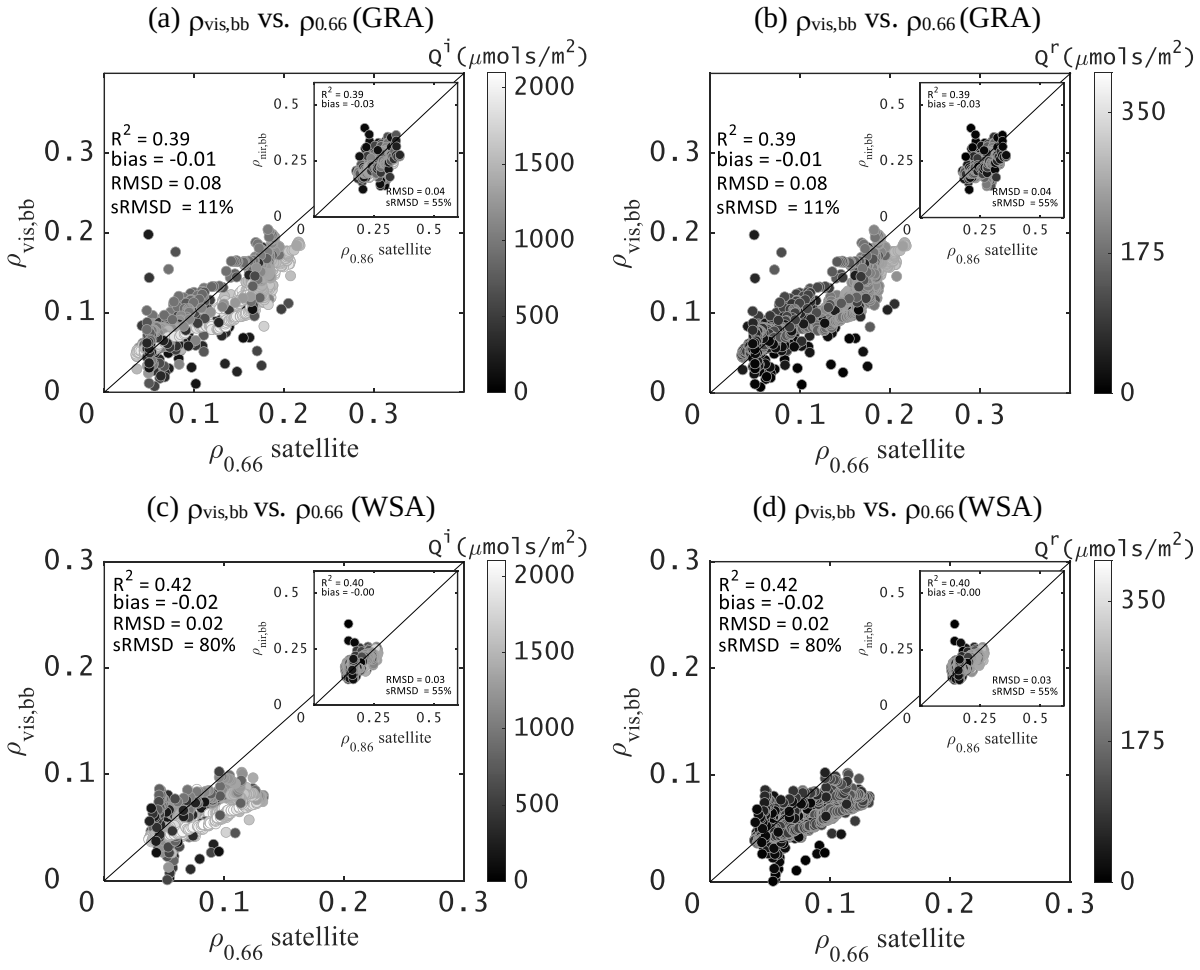

Figure 15: Illustrative examples of comparison between $\rho_{vis,bb}$ versus $\rho_{0.66}$ for a range of incident and reflected PAR (Q^i and Q^r) over grassland (Vaira ranch) (a, b) and woody savanna (Tonzi ranch) (c, d) in California. This clearly shows a tendency of systematic underestimation of $\rho_{vis,bb}$ with respect to $\rho_{0.66}$, and the underestimation increases at high Q^i and Q^r. Figures in the inset shows a similar comparison between $\rho_{nir,bb}$ versus $\rho_{0.86}$ for a range Q^i and Q^r. This analysis was performed with Planet Fusion data.

The overestimation tendency of $NDVI_{bb}$ apparently diminished with vegetation greening and it showed underestimation under dense vegetation cover (δ_{NDVI}<0). However, exceptions were also found in the deciduous broadleaf forest (DBF) and evergreen needleleaf forest (ENF), where the underestimation tendency of $NDVI_{bb}$ was visible across all the clusters of GCC (**Fig. 13d, e**). In the $NDVI_{bb}$ retrieval, the broadband NIR

reflectance covers up to 3.0 µm, which also accounts the reflectance signals from the shortwave infrared domain. Studies reported that in the coniferous needles, the surface reflectance in the shortwave infrared region is low (Pierrat et al., 2022; Roberts et al., 2004). This consequently leads to an underestimation of $\rho_{nir,bb}$ and $NDVI_{bb}$ at the ENF.

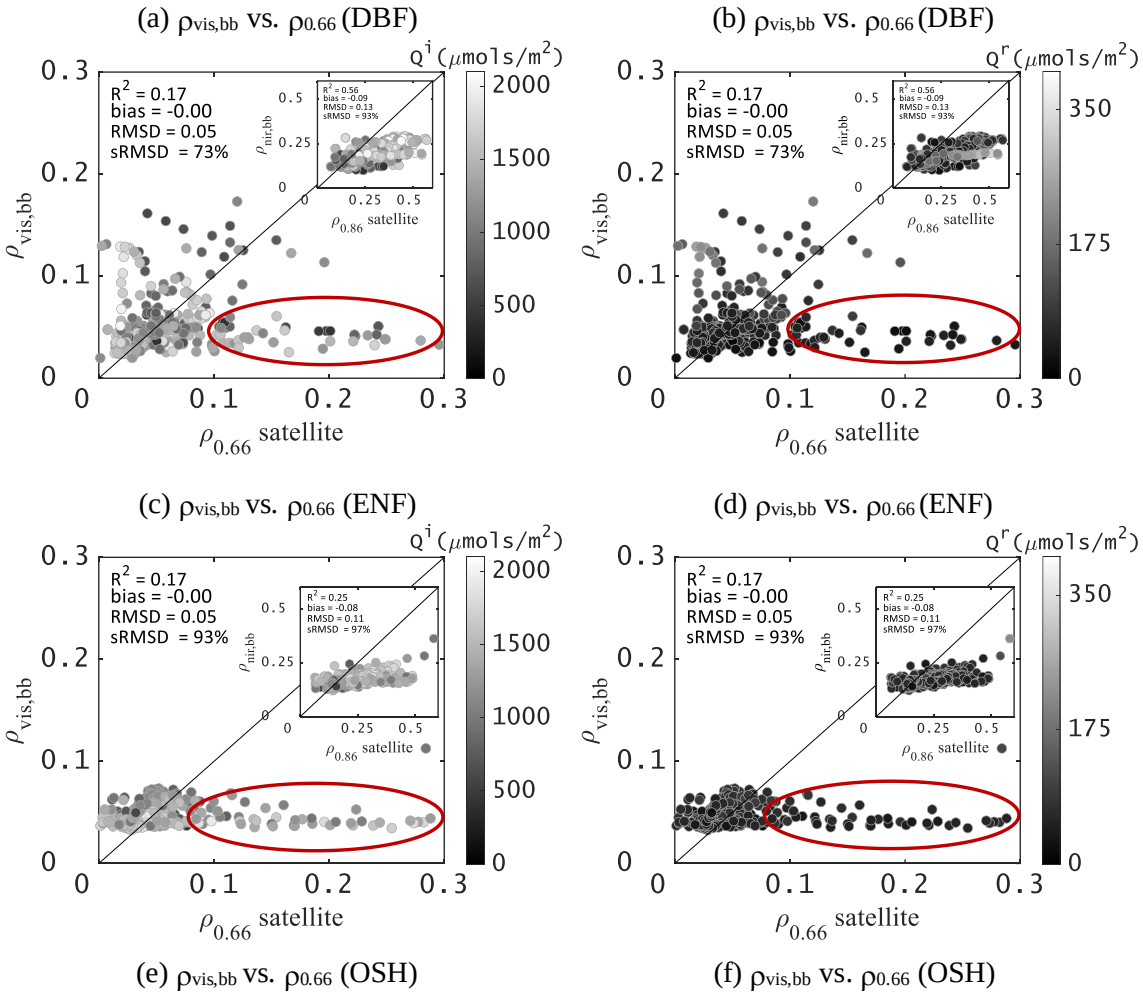

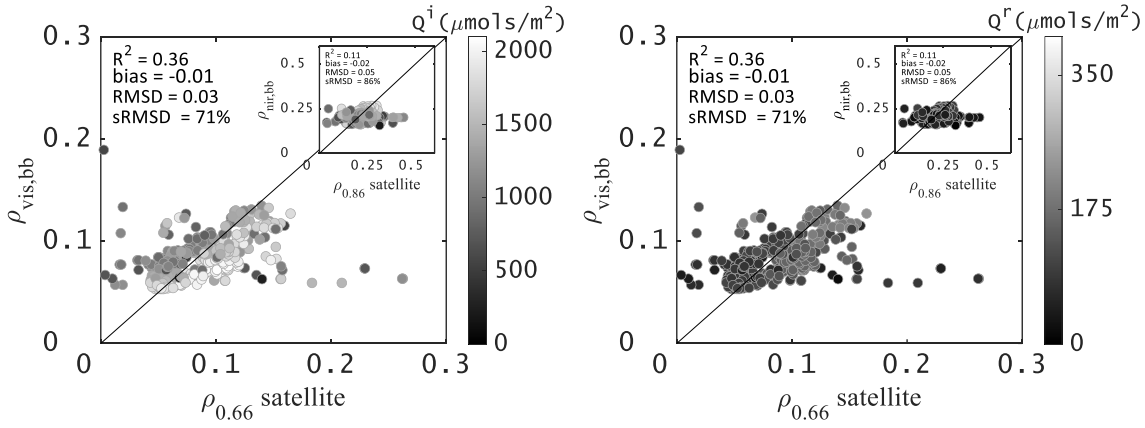

Figure 16: Illustrative examples of comparison between $\rho_{vis,bb}$ versus $\rho_{0.66}$ for a range of incident and reflected PAR (Q^i and Q^r) over deciduous broadleaf forests (DBF) (a, b), evergreen needleleaf forests (ENF) (c, d), and open shrubland (OSH) (e, f). This clearly shows a tendency of systematic underestimation of $\rho_{vis,bb}$ with respect to $\rho_{0.66}$, and the underestimation increases at high Q^i and Q^r. Figures in the inset shows a similar comparison between $\rho_{nir,bb}$ versus $\rho_{0.86}$ for a range Q^i and Q^r. This analysis was performed with HLS data since no Planet Fusion data was available for these ecosystems.

Figure 13 (a-f) also showed underestimation of $NDVI_{bb}$ at low GCC (GCC<0.35) corresponding to high background soil exposure (red data cluster at δ_{NDVI} <0). These datapoints could be associated with the low magnitude of Q^i and the details are revealed in **Fig. 14 – 16**. In all the ecosystems, there were data clusters with $\rho_{vis,bb}>\rho_{0.66}$ and these datapoints are associated with low Q^i (Q^i: 0 - 650 µmols) (**Fig. 14 - 16**). In the croplands, $\rho_{vis,bb}$ could also be affected due to irrigation, and $\rho_{vis,bb}$ might pick up the signal of wet soil, ultimately leading to $\rho_{vis,bb}>\rho_{0.66}$ (Ma et al., 2019). The effects of low Q^i and low Q^r were also evident in $\rho_{nir,bb}$ to some extent (**inset of Fig. 14 – 16**). These conditions led to an underestimation of the numerator in eq. (7) ($\rho_{nir,bb} - \rho_{vis,bb}<\rho_{0.86} - \rho_{0.66}$), ultimately leading to an underestimation of $NDVI_{bb}$ as compared to satellite NDVI.

These detailed analysis (**Fig. 14 – 16**) additionally helped understanding the reasons for underestimation of $NDVI_{bb}$ (**Fig. 3 – 6, Fig. 13**) and saturation of $NIRv_{bb}$ under high biomass when compared with the satellites (**Fig. 3 – 6**). A closer look at these figures

(**inset of Fig. 14 - 16**) revealed that almost 75-85% of the $\rho_{nir,bb}$ signal tends to become invariant with increasing $\rho_{0.86}$ beyond 0.30 µm at the cropland (alfalfa, corn) and forests (DBF, ENF) and beyond 0.25 µm at the OSH. The wavebands have very different bandwidths. The broadband NIR reflectance has differential sensitivity to increasing biomass as compared to $\rho_{0.86}$, which ultimately led to saturation in $NIRv_{bb}$ compared with satellite NIRv at high F_E. The consequence of the water stress on $\rho_{vis,bb}$ and $\rho_{nir,bb}$ estimation is described in Appendix A4 **(Fig. A4-A6)**.

4. Broader implications

Overall, our analysis shows that continuous and combined measurement of Q and R_g components serves a robust proximal sensing capability for diagnosing the seasonal variability in NDVI across ecological and climatic gradients. The $NDVI_{bb}$ versus satellite NDVI relationship was highly significant when compared with satellite sensors at different spatial resolutions (**Fig. 3 - 8**), across a broad spectrum of managed and unmanaged ecological settings, crop management regimes (e.g., irrigated vs. rainfed) that experience dynamic water stress, productivity variability, and physiological variations. With the availability of PAR and R_g components worldwide from different FLUXNET sub-networks, a global comparison with satellite NDVI and other vegetation indices is foreseen in the future. Due to the nature of the broadband reflectance retrieval from the proximal sensing of hemispherical radiation components, the spectral differences between broadband versus narrowband reflectances at the selected band regions are obvious. Therefore, we do not anticipate a perfect one to one relation between $NDVI_{bb}$ versus satellite NDVI unless we have hyperspectral tower-based remote sensing, or custom built sensors of Q and R_g components at the narrowband wavelengths. In fact,

comparing different NDVI from different satellite sensors showed substantial differences across different ecosystems (Fan and Liu, 2016; Huang et al., 2021).

The advantage of $NDVI_{bb}$ in comparison to spectrometer based NDVI became further evident when we compared $NDVI_{bb}$ and Planet Fusion NDVI with Apogee spectrometer NDVI at some flux tower sites covering four representative land cover types (alfalfa, corn, pasture, herbaceous vegetation) in California (**Fig. 17b, d, f, h**). The consistent negative bias in Apogee NDVI (-0.07 to -0.26) is mainly attributed to weak relationship in Apogee versus Planet Fusion red and NIR spectral reflectance (**Fig. 17a, c, e, g**), confirming that exploring the radiation components to estimate in-situ vegetation attributes is credible.

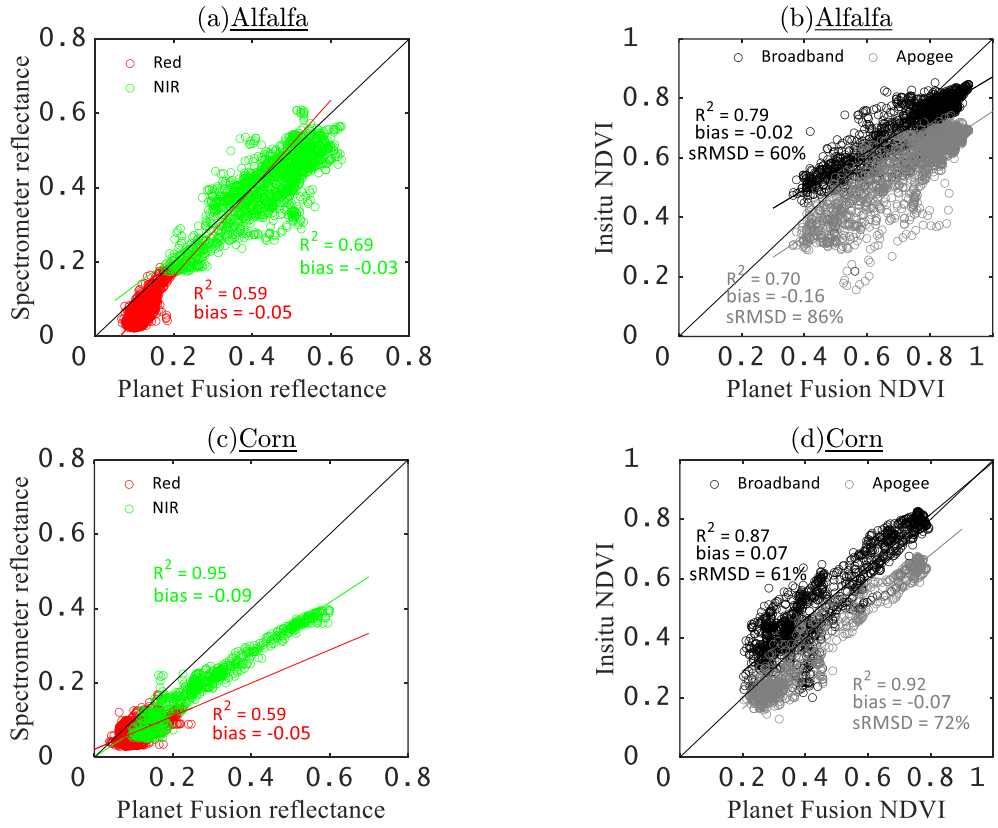

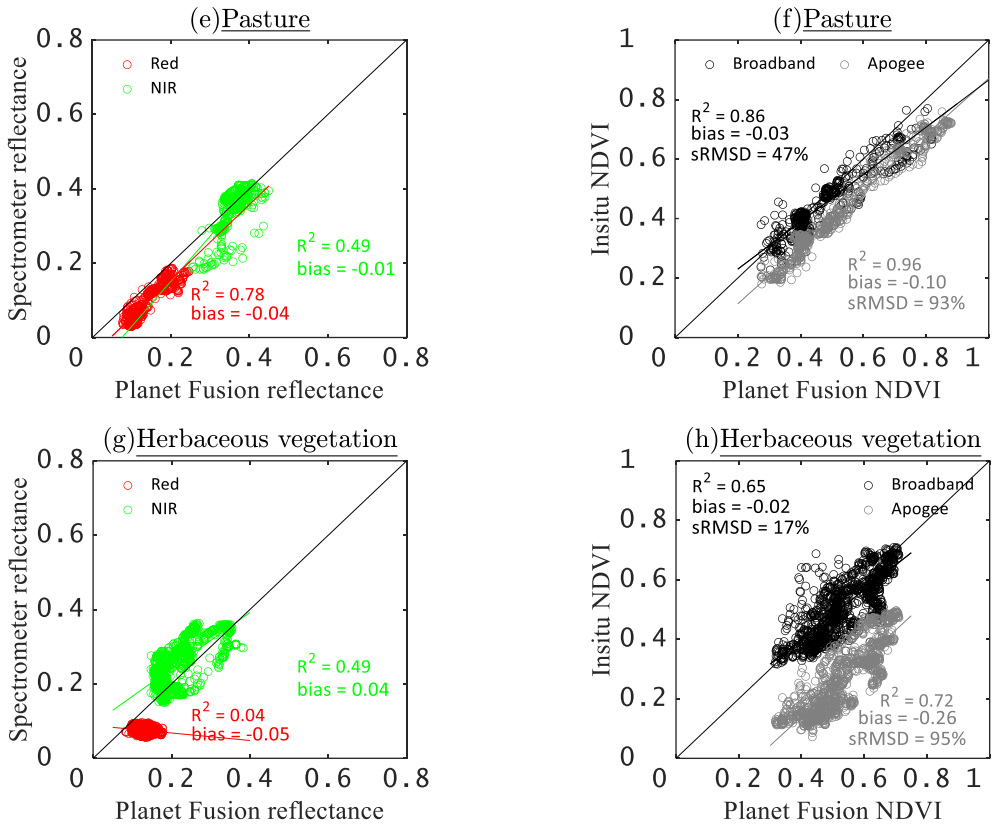

Figure 17: (a, c, e, g) Illustrative examples of comparison between Apogee spectrometer versus Planet Fusion spectral reflectances in red and NIR wavelengths in four representative ecosystems in California. (b, d, f, h) Comparison between Apogee spectrometer versus Planet Fusion and broadband NDVI in four representative ecosystems in California. This clearly shows a tendency of systematic underestimation of Apogee NDVI with respect to satellite, which is attributed to the disagreement in spectral reflectances between Apogee spectrometer and Planet Fusion.

Relatively greater disagreement of $NDVI_{bb}$ and $NIRv_{bb}$ with respect to HLS data is due to the relatively coarser spatial resolution of 30 x 30 m NDVI used in their comparison. Significant variability in greenness and fractional vegetation cover can be present at the sub-pixel scale depending on the ecosystem types (Turner et al, 2002). If HLS versus $NDVI_{bb}$ and $NIRv_{bb}$ agrees on a seasonal scale, we can assume that the greenness and vegetation fraction surrounding the tower is representative of the land cover within the 30 x 30 m S2 and L8/9 pixel containing the tower location. For several sites that showed moderate agreement between the tower $NDVI_{bb}$ and HLS NDVI, the variability in

fraction ground cover within the 30 x 30 m S2 and L8/9 pixel might be responsible for such a behavior. This indicates the challenges and intricacies associated with respect to directly comparing flux tower $NDVI_{bb}$ with satellite NDVI at a coarser spatial scale in the presence of profound spatial variability in vegetation cover. The extent to which the variability in fractional vegetation cover within one HLS pixel could impact such comparison, could only be estimated upon having coincident Planet Fusion (3 m) and HLS (30 m) data across all the sites. In the present study, only a small subset of sites (seven biomet sites) had both Planet fusion and HLS datasets. This led us examining the effects of the variability of vegetation fraction on $NDVI_{bb}$ versus satellite NDVI evaluation at four different ecosystems (**Appendix A5; Fig. A7**). The statistical comparison clearly showed the effects due to the variability in vegetation fraction when NDVI average from 10 x 10 pixels of Planet Fusion was used for the evaluation of $NDVI_{bb}$. Although a detailed spatial variability analysis could shed greater insight, such analysis is beyond the scope of the present study. Nevertheless, $NDVI_{bb}$ is a valid proxy of satellite NDVI for a wide range of conditions tested.

We found that $NIRv_{bb}*\Sigma Q^i$ is a robust structural proxy for GPP by combining 28 site-years of data (seven sites and four years for each site). $NIRv_{bb}*\Sigma Q^i$ tends to have higher signal quality (Baldocchi et al., 2020) as compared to $NDVI_{bb}$, and $NDVI_{bb}$ is known to become invariant at high GPP (Baldocchi et al., 2020, Dechant et al., 2022). The correlative relationship between GPP and NDVI emerges because green leaves do photosynthesis, and there is a seasonality in greenness and photosynthesis. Therefore, one should be careful to use such correlative relationships to upscale GPP from the information of NDVI. A linear relationship between GPP and $NIRv_{bb}*\Sigma Q^i$ was also

reported for croplands (Dechant et al., 2020, 2022; Liu et al., 2020; Wu et al., 2019), which could further be exploited to understand GPP variability at different spatio-temporal scales. Our results confirm and considerably extend previous findings and demonstrated that the linearity between GPP and $NIRv_{bb}*\Sigma Q^{i}$ also holds for a range of ecosystems that experience variable water stress. The significant outcome of this analysis is that from the measurements of four radiation components, we are able to detect the most critical vegetation variables that have a direct link with ecosystem carbon assimilation across a range of climatic gradients. Our results also substantiate the findings of Pierrat et al. (2022) who showed that in the boreal ecosystems where seasonal downregulation of photosynthesis occurs without significant changes in canopy structure or chlorophyll content, NDVI scales poorly with carbon assimilation. We believe that more work is needed to develop a robust scaling function for GPP versus $NIRv_{bb}*\Sigma Q^{i}$ relationship across a wide spectrum of ecological gradients. Such studies should use high spatial resolution satellite data, standardized PAR and R_g sensors and calibration methods. Nevertheless, our tower-based broadband NDVI and NIRv is promising enough to be treated as highly valuable and critical vegetation attributes relevant to flux measurement footprints for ecosystem modeling.

Despite its own limitations, the present study could be seen promising enough that highlights the utility of shortwave and photosynthetically active radiation measurements to augment the proximal sensing capability at the flux tower sites. The in-situ broadband NDVI derived through transforming these radiation signals could make a stronger case for how these data could be used for handshaking between ecosystem-scale measurements and remote sensing for scaling and/or understanding satellite observables.

5. Summary and conclusion

We conclude that the net fluxes of broadband shortwave radiation components in conjunction with the components of photosynthetically active radiation offer a novel proximal sensing perspective to directly retrieve a robust broadband NDVI and NIRv relevant to explain ecosystem productivity for a wide spectrum of ecosystems and climatic gradients. This novel perspective is obtained through a simplified method which neither needs explicit radiative transfer for solving canopy reflectance, nor does it need any additional spectrometer measurements. Our analysis revealed that the discrepancies between the broadband NDVI and operational satellite-based NDVI products are due to the differences in hemispherical versus directional reflectance, differential sensitivity of broad visible and near infrared reflectance to background soil exposure, water stress and biomass accumulation and resultant saturation of the hemispherical reflectance signals at high biomass.

These critical insights and multiscale comparison with satellite products are highly significant to monitoring the intraseasonal and interannual variability of NDVI directly at the flux tower sites and relevant to validating operational NDVI products from the Earth observation mission. Statistical analysis over a range of ecosystems and climatic limits demonstrates the potential of the broadband NDVI and NIRv as a valid alternative to study the effects of vegetation seasonality on energy-water-carbon flux interactions and their interannual variability worldwide. This novel approach can be implemented across all the flux tower sites of AmeriFlux and Fluxnet subnetworks to generate insightful vegetation dynamics information for the ecosystem modeling community and complementing the PhenoCam observations. As more flux sites are equipped with the

887 necessary radiometric instrumentation, i.e., quantum sensors and pyranometers, we
888 expect the available ground-based data to increase dramatically. This will provide the
889 community with a critical tool to link flux tower measurements with satellite-borne
890 observations.

891 6. Acknowledgements

892 KM acknowledges the Mobility Fellowship from the FNR Luxembourg
893 (INTER/MOBILITY/2020/14521920/MONASTIC). MS acknowledges the financial
894 support from the FNR CORE programme (C19/SR/13652816/CAPACITY). DDB
895 acknowledges support from NASA Ecostress project and the US Department of Energy,
896 Office of Science which supports the AmeriFlux project as well as the Delta Stewardship
897 Council and the California Department of Water Resources (DWR). AA-O acknowledges
898 the “Ramon y Cajal” Fellowship RYC2021-034455-I. The National Ecological
899 Observatory Network is a program sponsored by the National Science Foundation and
900 operated under cooperative agreement by Battelle. This material is based in part upon
901 work supported by the National Science Foundation through the NEON Program.

902 Reference:

903 Anderson, H., Lennart, N., Tømmervik, H., Karlsen, S., Nagai, S., Cooper, E., 2016.
904 Using Ordinary Digital Cameras in Place of Near-Infrared Sensors to Derive Vegetation
905 Indices for Phenology Studies of High Arctic Vegetation. Remote Sensing, 8, 847.
906 https://doi.org/10.3390/rs8100847.
907 Arias-Ortiz, A., Oikawa, P. Y., Carlin, J., Masqué, P., Shahan, J., Kanneg, S., Paytan, A.,
908 Baldocchi, D. D., 2021., Tidal and nontidal marsh restoration: a trade-off between
909 carbon sequestration, methane emissions, and soil accretion. Journal of Geophysical
910 Research: Biogeosciences, 126(12). https://doi.org/10.1029/2021JG006573.

911 Badgley, G., Field, C.B., Berry, J.A., 2017. Canopy near-infrared reflectance and
912 terrestrial photosynthesis. Science advances, 3(3), e1602244.
913 Badgley, G., Anderegg, L. D., Berry, J. A., Field, C. B., 2019. Terrestrial gross primary
914 production: Using NIR_V to scale from site to globe. Global Change Biology, 25, 3731–
915 3740. https://doi.org/10.1111/gcb.14729.
916 Baldocchi, D.D., Ryu, Y., Dechant, B., Eichelmann, E., Hemes, K., Ma, S., Rey Sanchez,
917 C., Shortt, R., Szutu, D., Valach, A., Verfaillie, J., Badgley, G., Zeng, Y., Berry, J.A.,
918 2020. Outgoing near-infrared radiation from vegetation scales with canopy
919 photosynthesis across a spectrum of function, structure, physiological capacity, and
920 weather. Journal of Geophysical Research: Biogeosciences,125, e2019JG005534.
921 https://doi.org/10.1029/2019JG005534.
922 Baldocchi, D.D., Ma, S., Verfaillie, J., 2021. On the inter- and intra-annual variability of
923 ecosystem evapotranspiration and water use efficiency of an oak savanna and annual
924 grassland subjected to booms and busts in rainfall. Global Change Biology, 27, 359–
925 375. https://doi.org/10.1111/gcb.15414.
926 Blakely, B., Moore, C., Bernacchi, C. J., Pederson, T., 2022. AmeriFlux BASE US-UiA
927 University of Illinois Switchgrass, Ver. 2-5, AmeriFlux AMP, (Dataset).
928 https://doi.org/10.17190/AMF/1617725
929 Brown, L. A., Dash, J., Ogutu, B. O., Richardson, A. D., 2017. On the relationship
930 between continuous measures of canopy greenness derived using near-surface remote
931 sensing and satellite-derived vegetation products. Agricultural and Forest Meteorology,
932 247, 280-292.
933 Browning, D.M., Karl, J.W., Morin, D., Richardson, A.D., Tweedie, C.E., 2017.
934 Phenocams Bridge the Gap between Field and Satellite Observations in an Arid
935 Grassland Ecosystem. Remote Sensing, 9(10),1071. https://doi.org/10.3390/rs9101071.
936 Burke, M.W., Rundquist, B.C., 2021. Scaling PhenoCam GCC, NDVI, and EVI2 with
937 harmonized Landsat-Sentinel using Gaussian processes. Agricultural and Forest
938 Meteorology, 300, 108316.
939 Campbell, G., Norman, J., 1998. An Introduction to Environmental Biophysics. Springer-
940 Verlag, New York.

941 Camps-Valls, G., et al., 2021. A unified vegetation index for quantifying the terrestrial
942 biosphere. Science Advances, 7, eabc7447, doi:10.1126/sciadv.abc7447
943 Carlson,T.N., Ripley, D.A.,1997.On the relation between NDVI, fractional vegetation
944 cover, and leaf area index. Remote Sensing of Environment, 62(3), 241–252.
945 https://doi.org/10.1016/ S0034-4257(97)00104-1.
946 Claverie, M., Ju, J., Masek, J.G., Dungan, J.L., Vermote, E.F., Roger, J.-C., Skakun,
947 S.V., Justice, C., 2018. The Harmonized Landsat and Sentinel-2 surface reflectance
948 data set. Remote Sensing of Environment, 219, 145-161.
949 https://doi.org/10.1016/j.rse.2018.09.002.
950 Dechant, B., Ryu, Y., Badgley, G., Zeng, Y., Berry, J.A., Zhang, Y., Goulas, Y., Li, Z.,
951 Zhang, Q., Kang, M., Li, J., Moya, I., 2020. Canopy structure explains the relationship
952 between photosynthesis and sun-induced chlorophyll fluorescence in crops. Remote
953 Sensing of Environment, 241, 111733. https://doi.org/10.1016/j.rse.2020.111733.
954 Dechant, B., Ryu, Y., Badgley, G., Kohler, P., Rascher, U., Migliavacca, M., Zhang, Y.,
955 Tagliabue, G., Guan, K., Rossini, M., Goulas, Y., Zeng, Y., Frankenberg, C., Berry, J.,
956 2022. NIRvP: A robust structural proxy for sun-induced chlorophyll fluorescence and
957 photosynthesis across scales. Remote Sensing of Environment, 268, 112763.
958 https://doi.org/10.1016/j.rse.2021.112763.
959 Descals, A., Verger, A., Yin, G., Filella, I., Fu, Y.H., Piao, S., Janssens, I.A., Peñuelas, J.,
960 2022. Radiation-constrained Boundaries Cause Nonuniform Responses of the Carbon
961 Uptake Phenology to Climatic Warming in the Northern Hemisphere. Global Change
962 Biology, 29, 719–730. https://doi.org/10.1111/gcb.16502.
963 Eichelmann, E., Hemes, K. S., Knox, S. H., Oikawa, P. Y., Chamberlain, S. D.,
964 Sturtevant, C., Verfaillie, J., Baldocchi, D.D., 2018. The effect of land cover type and
965 structure on evapotranspiration from agricultural and wetland sites in the Sacramento–
966 San Joaquin River Delta, California. Agricultural and Forest Meteorology, 256–257,
967 179–195. https://doi.org/10.1016/j.agrformet.2018.03.007.
968 Fan, X., Liu, Y., 2016. A global study of NDVI difference among moderate-resolution
969 satellite sensors. ISPRS Journal of Photogrammetry and Remote Sensing, 121, 177-191,
970 https://doi.org/10.1016/j.isprsjprs.2016.09.008.

971 Fensholt, R., Sandholt, I., 2003. Derivation of a shortwave infrared water stress index
972 from MODIS near- and shortwave infrared data in a semiarid environment. Remote
973 Sensing of Environment, 2003, 87, 111–121. https://doi.org/10.1016/j.rse.2003.07.002.
974
975 Field, C.B., Mooney, H.A., 1986. The photosynthesis-nitrogen relationship in wild plants.
976 In T. Givnish (edited) On the Economy of Plant Form and Function, Cambridge
977 University Press, 25-55.
978 Filippa, G., Cremonese, M., Galvagno, M., Sonnentag, O., Humphreys, E., Hufkens, K.,
979 Ryu, Y., Verfaillie, J., Morra di Cella, U., Richardson, A.D., 2018. NDVI derived from
980 near-infrared-enabled digital cameras: Applicability across different plant functional
981 types. Agricultural and Forest Meteorology, 249, 275–285. https://doi.org/10.1016/j.
982 agrformet.2017.11.003.
983 Foley, J.A., Ramankutty, N., Brauman, K.A., Cassidy, E.S., Gerber, J.S., Johnston, M.,
984 Mueller, N.D., O'Connell, C., Ray, D.K., West, P.C., Balzer, C., Bennet, E.M.,
985 Carpenter, S.R., Hill, J., Monfreda, C., Polasky, S., Rockström, J., Sheehan, J., Siebert,
986 S., Tilman, D. and Zaks, D.P.M. 2011, Solutions for a cultivated planet, Nature, 478,
987 7369, 337-342.
988 Godfray, C.H., Beddington, J.R., Crute, I.R., Haddad, L., Lawrence, D., Muir, J.F.,
989 Pretty, J., Robinson, S., Thomas, S.M. and Toulmin, C. 2010, Food security: the
990 challenge of feeding 9 billion people, Science, 327 (5967), 812-818.
991 Gamon, J.A., Field, C.B., Goulden, M.L., Griffin, K.L., Hartley, A.E., Joel, G., Peñuelas,
992 J., Valentini, R., 1995. Relationship between NDVI, canopy structure and
993 photosynthesis in three Californian vegetation types. Ecological Applications, 5(1), 28
994 – 41. https://doi.org/10.2307/1942049.
995 Gitelson, A.A., Gamon, J.A., 2015. The need for a common basis for defining light-use
996 efficiency: Implications for productivity estimation. Remote Sensing of Environment,
997 156, 196-201.
998 Gitelson, A.A., Peng, Y., Huemmrich, K.F., 2014. Relationship between fraction of
999 radiation absorbed by photosynthesizing maize and soybean canopies and NDVI from
1000 remotely sensed data taken at close range and from MODIS 250m resolution data.

Remote Sensing of Environment, 147, 108–120. https://doi.org/10.1016/j.rse.2014.02.014.

Gitelson, A. A., 2019. Remote estimation of fraction of radiation absorbed by photosynthetically active vegetation: Generic algorithm for maize and soybean. Remote Sensing Letters, 10(3), 283-291.

Hao, F., Zhang, X., Ouyang, W., Skidmore, A.K., Toxopeus, A.G., 2012. Vegetation NDVI linked to temperature and precipitation in the upper catchments of Yellow River. Environmental Modeling & Assessment, 17, 389-398.

Hemes, K.S., Verfaillie, J., Baldocchi, D.D., 2020. Wildfire-smoke aerosols lead to increased light use efficiency among agricultural and restored wetland land uses in California's Central Valley. Journal of Geophysical Research: Biogeosciences, 125, e2019JG005380. https://doi.org/10.1029/2019JG005380.

Hoek van Dijke, A.J., Mallick, K., Schlerf, M., Machwitz, M., Herold, M., and Teuling, A.J., 2020. Examining the link between vegetation leaf area and land–atmosphere exchange of water, energy, and carbon fluxes using FLUXNET data, Biogeosciences, 17, 4443–4457. https://doi.org/10.5194/bg-17-4443-2020.

Huang, X., Xiao, J., Ma, M., 2019. Evaluating the performance of satellite-derived vegetation indices for estimating gross primary productivity using FLUXNET observations across the globe. Remote Sensing, 11(15), 1823.

Huang, S., Tang, L., Hupy, J. P., Wang, Y., Shao, G., 2021. A commentary review on the use of normalized difference vegetation index (NDVI) in the era of popular remote sensing, Journal of Forestry Research, 32(1), 1-6. https://doi.org/10.1007/s11676-020-01155-1.

Huemmrich, K.F., Black, T.A., Jarvis, P.G., McCaughey, J.H., Hall, F.G., 1999. High temporal resolution NDVI phenology from micrometeorological radiation sensors, Journal Geophysical Research, 104, 27935-27944. https://doi.org/10.1029/1999JD900164.Huete, A. R., 1988. A soil-adjusted vegetation index (SAVI). Remote sensing of environment, 25(3), 295-309. https://doi.org/10.1016/0034-4257(88)90106-X.

1030 Kaufman, Y. J., Tanre, D., 1992. Atmospherically resistant vegetation index (ARVI) for
1031 EOS-MODIS. IEEE transactions on Geoscience and Remote Sensing, 30 (2), 261-270.
1032 http://doi.org/10.1109/36.134076.
1033 Kumar, L., Schmidt, K., Dury, S., Skidmore, A., 2001. Imaging spectrometry and
1034 vegetation science. In F. D. van der Meer & S. M. de Jong (Eds.), Imaging
1035 spectrometry (pp. 111–155). Dordrecht: Kluwer Academic Publishers.
1036 Leuning, R., 2007. The correct form of the Webb, Pearman and Leuning equation for
1037 eddy fluxes of trace gases in steady and non-steady state, horizontally homogeneous
1038 flows. Boundary-Layer Meteorology, 123, 263–267. https://doi.org/10.1007/s10546-
1039 006-9138-5.
1040 Liu, F., Wang, C.K., Wang, X.C., 2021. Can vegetation index track the interannual
1041 variation in gross primary production of temperate deciduous forests? Ecological
1042 Processes, 10(1), 51. https://doi.org/10.1186/s13717-021-00324-2.Liu, L., Liu, X.,
1043 Chen, J., Du, S., Ma, Y., Qian, X., Chen, S., Peng, D., 2020. Estimating Maize GPP
1044 using near-infrared radiance of vegetation. Science of Remote Sensing, 100009.
1045 https://doi.org/10.1016/j.srs.2020.100009.
1046 Liu, Z., Liu, K., Zhang, J., Yan, C., Lock, T.R., Kallenbach, R.L., Yuan, Z., 2022.
1047 Fractional coverage rather than green chromatic coordinate is a robust indicator to track
1048 grassland phenology using smartphone photography. Ecological Informatics, 68,
1049 101544.
1050 Liu, J., Van Iersel, M.W., 2021. Photosynthetic physiology of blue, green, and red light:
1051 Light intensity effects and underlying mechanisms. Frontiers in plant science, 12, 328,
1052 https://doi.org/10.3389/fpls.2021.619987.
1053 Ma, S., Baldocchi, D.D., Wolf, S., Verfaillie, J., 2016. Slow ecosystem responses
1054 conditionally regulate annual carbon balance over 15 years in Californian oak-grass
1055 savanna. Agricultural and Forest Meteorology, 228, 252–264.
1056 https://doi.org/10.1016/j.agrformet.2016.07.016.
1057 Ma, S., Zhou, Y., Gowda, P.H., Dong, J., Zhang, G., Kakani, V.G., Wagle, P., Chen, L.,
1058 Flynn, K.C. Jiang, W., 2019. Application of the water-related spectral reflectance
1059 indices: A review. Ecological indicators, 98, 68-79.

Magney, T.S., Bowling, D.R., Logan, B.A., Grossmann, K., Stutz, J., Blanken, P.D., et al., 2019. Mechanistic evidence for tracking the seasonality of photosynthesis with solar-induced fluorescence. Proceedings of the National Academy of Sciences, 116(24), 11640-11645.

Mutanga, O., Masenyama, A., Sibanda, M., 2023. Spectral saturation in the remote sensing of high-density vegetation traits: A systematic review of progress, challenges, and prospects. ISPRS Journal of Photogrammetry and Remote Sensing, 198, 297-309.

Mutanga, O., Skidmore, A.K., 2004. Narrow band vegetation indices overcome the saturation problem in biomass estimation. International journal of remote sensing, 25(19), 3999-4014.

Metzger, S., Ayres, E., Durden, D., Florian, C., Lee, R., Lunch, C., Luo, H., Pingintha-Durden, N., Roberti, J. A., San Clements, M., Sturtevant, C., Xu, K., Zulueta, R. C., 2019. From NEON field sites to data portal: a community resource for surface–atmosphere research comes online. Bulletin of The American Meteorological Society, 100(11), 2305-2325. https://doi.org/10.1175/BAMS-D-17-0307.1.

Monteith, J. L., 1972. Solar radiation and productivity in tropical ecosystems. Journal of applied ecology, 9(3), 747-766.

Ollinger, S.V., 2011. Sources of variability in canopy reflectance and the convergent properties of plants. New Phytologist, 189(2), 375-394, doi:10.1111/j.1469-8137.2010.03536.x.

Petach, A.R., Toomey, M., Aubrecht, D.M., Richardson, A.D., 2014. Monitoring vegetation phenology using an infrared-enabled security camera. Agricultural and Forest Meteorology, 195–196, 143–151.

Pierrat, Z., Magney, T., Parazoo, N. C., Grossmann, K., Bowling, D. R., Seibt, U., et al., 2022. Diurnal and seasonal dynamics of solar-induced chlorophyll fluorescence, vegetation indices, and gross primary productivity in the boreal forest. Journal of Geophysical Research: Biogeosciences, 127, e2021JG006588. https://doi.org/10.1029/2021JG006588

Prabhakara, K., Hively, W.D., McCarty, G.W., 2015. Evaluating the relationship between biomass, percent groundcover and remote sensing indices across six winter cover crop

fields in Maryland, United States. International journal of applied earth observation and geoinformation, 39, 88-102.

Qi, J., Chehbouni, A., Huete, A.R., Kerr, Y.H., Sorooshian, S., 1994. A modified soil adjusted vegetation index. Remote Sensing of Environment, 48, 119–126. https://doi.org/ 10.1016/0034-4257(94)90134-1.

Reichstein, M., Falge, E., Baldocchi, D., Papale, D., Aubinet, M., Berbigier, P., et al., 2005. On the separation of net ecosystem exchange into assimilation and ecosystem respiration: Review and improved algorithm. Global Change Biology. 11, 1424-1439. https://doi.org/10.1111/j.1365-2486.2005.001002.x.

Richardson, A.D., Jenkins, J.P., Braswell, B.H., Hollinger, D.Y., Ollinger. S.V., Smith, M.L., 2007. Use of digital webcam images to track spring green-up in a deciduous broadleaf forest, Oecologia, 152(2), 323-334, doi:10.1007/s00442-006-0657-z.

Richardson, A.D., Black, T.A, Ciais, P., Delbart, N., Friedl, M.A., Gobron, N., Hollinger, D.Y., Kutsch, W.L., Longdoz, B., Luyssaert, S. and Migliavacca, M., 2010. Influence of spring and autumn phenological transitions on forest ecosystem productivity. Philosophical Transactions of the Royal Society B: Biological Sciences, 365(1555), pp.3227-3246.

Richardson, A.D., Keenan, T.F., Migliavacca, M., Ryu, Y., Sonnentag, O., Toomey, M., 2013. Climate change, phenology, and phenological control of vegetation feedbacks to the climate system, Agricultural and Forest Meteorology, 169, 156-173, doi:10.1016/j.agrformet.2012.09.012.

Ritter, F., Berkelhammer, M. Garcia-Eidell, C., 2020. Distinct response of gross primary productivity in five terrestrial biomes to precipitation variability. Communications Earth and Environment, 1, 34. https://doi.org/10.1038/s43247-020-00034-1.

Roberts, D.A., Ustin, S.L., Ogunjemiyo, S., Greenberg, J., Dobrowski, S.Z., Chen, J., Hinckley, T.M., 2004. Spectral and Structural Measures of Northwest Forest Vegetation at Leaf to Landscape Scales. Ecosystems, 7, 545–562. https://doi.org/10.1007/s10021-004-0144-5.

Rocha, A.V., Shaver, G.R., 2009. Advantages of a two band EVI calculated from solar and photosynthetically active radiation fluxes. Agricultural and Forest Meteorology, 149 (9), 1560–1563. https://doi.org/10.1016/j.agrformet.2009.03.016.

Rocha, A.V., Appel, R., Bret-Harte, M.S., Euskirchen, E.S., Salmon, V., Shaver, G., 2021. Solar position confounds the relationship between ecosystem function and vegetation indices derived from solar and photosynthetically active radiation fluxes. Agricultural and Forest Meteorology, 298, 108291.

Ryu, Y., Verfaillie, J., Macfarlane, C., Kobayashi, H., Sonnentag, O., Vargas R., Ma, S., Baldocchi, D.D., 2012. Continuous observation of tree leaf area index at ecosystem scale using upward-pointing digital cameras. Remote Sensing of Environment, 126, 116–125. https://doi.org/10.1016/j.rse.2012.08.027.

Scott, R.L., Hamerlynck, E.P., Jenerette, G.D., Moran, M.S., Barron-Gafford, G., 2010. Carbon dioxide exchange in a semidesert grassland through drought-induced vegetation change. Journal of Geophysical Research: Biogeosciences, 115(G3). https://doi.org/10.1029/2010JG001348.

Sellers, P. J., 1985. Canopy reflectance, photosynthesis, and transpiration. International Journal of Remote Sensing, 6, 1335–1372.

Sellers, P.J., Dickinson, R.E., Randall, D.A., Betts, A.K., Hall, F.G., Berry, J.A., Collatz, G.J., Denning, A.S., Mooney, H.A., Nobre, C.A., Sato, N., Field, C.B., Henderson-Sellers, A., 1997. Modelling the exchanges of energy, water, and carbon between continents and the atmosphere, Science, 275 (5299), 502-509.

Smith, T., Boers, N., 2023. Global vegetation resilience linked to water availability and variability. Nature Communications, 14, 498. https://doi.org/10.1038/s41467-023-36207-7.

Sonnentag, O., Hufkens, K., Teshera-Sterne, C., Young, A. M., Friedl, M., Braswell, B. H., et al., 2012. Digital repeat photography for phenological research in forest ecosystems. Agricultural and Forest Meteorology, 152, 159–177.

Suyker, A. E., Verma, S. B., Burba, G. G., Arkebauer, T. J., 2005. Gross primary production and ecosystem respiration of irrigated maize and irrigated soybean during a growing season, Agricultural and Forest Meteorology, 131(3-4), 180-190. https://doi.org/10.1016/j.agrformet.2005.05.007.

Seyednasrollah, B., Young, A.M., Hufkens, K., Milliman, T., Friedl, M.A., Frolking, S., Richardson, A.D., 2019. Tracking vegetation phenology across diverse biomes using

Version 2.0 of the PhenoCam Dataset, Scientific Data, 6(1), 222, doi:10.1038/s41597-019-0229-9.

Tesfaye, A.A., Awoke, G.B., 2021. Evaluation of the saturation property of vegetation indices derived from sentinel-2 in mixed crop-forest ecosystem. Spatial Information Research, 29, 109–121. https://doi.org/10.1007/s41324-020-00339-5.

Tian, F., Cai, Z., Jin, H., Hufkens, K., Scheifinger, H., Tagesson, T., et al., 2021. Calibrating vegetation phenology from Sentinel-2 using eddy covariance, PhenoCam, and PEP725 networks across Europe. Remote Sensing of Environment, 260, 112456.

Turner, D.P., Gower, S.T., Cohen, W.B., Gregory, M., Maiersperger, T.K., 2002. Effects of spatial variability in light use efficiency on satellite-based NPP monitoring. Remote Sensing of Environment, 80, 397 – 405. https://doi.org/10.1016/S0034-4257(01)00319-4.

Ustin, S.L., Middleton, E.M., 2021. Current and near-term advances in Earth observation for ecological applications, Ecological Processes, 10 (1), 1, doi:10.1186/s13717-020-00255-4.

Wang, T., Verfaillie, J., Szutu, D., Baldocchi, D.D., 2023. Handily measuring sensible and latent heat exchanges at a bargain: A test of the variance-Bowen ratio approach. Agricultural and Forest Meteorology, 333, 109399. https://doi.org/10.1016/j.agrformet.2023.109399.

Weiss, A., Norman, J., 1985. Partitioning solar radiation into direct and diffuse, visible and near-infrared components. Agricultural and Forest Meteorology, 34, 205–213. https://doi.org/10.1016/0168-1923(85)90020-6.

Wilson, T.B., Meyers, T.P., 2007. Determining vegetation indices from solar and photosynthetically active radiation fluxes. Agricultural and Forest Meteorology, 144, 160 – 179. https://doi.org/10.1016/j.agrformet.2007.04.001.

Wu, G., Guan, K., Jiang, C., Peng, B., Kimm, H., Chen, M., Yang, X., Wang, S., Sukyer, A. E., Bernacchi, C., Moore, C.E., Zeng, Y., Berry, J., Cendrero-Mateo, M.P., 2019. Radiance-based NIRv as a proxy for GPP of corn and soybean. Environmental Research Letters, 15, 034009. https://doi.org/10.1088/1748-9326/ab65cc.

Zhang, Y., Commane, R., Zhou, S., Williams, A.P. Gentine, P., 2020. Light limitation regulates the response of autumn terrestrial carbon uptake to warming. Nature Climate Change, 10 (8), 739-743. https://doi.org/10.1038/s41558-020-0806-0.

Zhang, P., Anderson, B., Barlow, M., Tan, B., Myneni, R. B.,2004. Climate-related vegetation characteristics derived from Moderate Resolution Imaging Spectroradiometer (MODIS) leaf area index and normalized difference vegetation index. Journal of Geophysical Research: Atmospheres, 109(D20).

Zhou, X., Wang, X., Zhang, S., Zhang, Y., Bai, X., 2020. Combining Phenological Camera Photos and MODIS Reflectance Data to Predict GPP Daily Dynamics for Alpine Meadows on the Tibetan Plateau. Remote Sensing, 12(22), 3735. https://doi.org/10.3390/rs12223735.

1211 **Figure captions**:

Figure 1: (a) Conceptual diagram showing the hypothesis for estimating broadband spectral reflectance from the measurements of hemispherical broadband radiation components in PAR and total shortwave spectral region. It also shows an example of the narrowband spectral reflectances that we obtain in red and near infrared spectral region from operational remote sensing satellite Landsat-9 (Source: https://landsat.usgs.gov/spectral-characteristics-viewer). VIS signified visible, NIR signifies near-infrared, MIR signifies mid-wave infrared. (b) Figure showing the scaling factor for converting PAR (both incident and reflected) from µmols/m^2/s to W/m^2 for a range of NDVI as an example over rice crop in California.

Figure 2: An illustrative diagram showing the sequence of results corresponding to the science questions (SQs) and the respective figure numbers associated with the description of results falling under individual science question.

Figure 3: (a) Plots of $NDVI_{bb}$ and $NIRv_{bb}$ versus Planet Fusion NDVI and NIR_V (3 m spatial resolution) in the Californian cropland ecosystems for NDVI>0.25 for a range of evaporative fraction (F_E) representing stressed to unstressed conditions. F_E is an indicator of water availability and denotes the ratio of evaporation (latent heat flux) to equilibrium evaporation. (b) Temporal dynamics of $NDVI_{bb}$ (black dots) and NDVI (green dots) along with daily precipitation (P) (blue stairs) shows close correspondence between them in Alfalfa [Bi1] and Corn [Bi2].

Figure 4: (a) Plots of $NDVI_{bb}$ and $NIRv_{bb}$ versus Planet Fusion NDVI and NIR_V (3 m spatial resolution) in water-limited Californian grassland (GRA) and woody savanna (WSA) ecosystems for NDVI>0.25 for a range of evaporative fraction (F_E) representing stressed to unstressed conditions. F_E is an indicator of water availability and denotes the ratio of evaporation (latent heat flux) to equilibrium evaporation. (b) Temporal dynamics of $NDVI_{bb}$ (black dots) and NDVI (green dots) along with daily precipitation (P) (blue stairs) shows close correspondence between them especially in the grassland [Var] and partly in woody savanna [Ton].

Figure 5: (a) Plots of $NDVI_{bb}$ and $NIRv_{bb}$ versus Planet Fusion NDVI and NIR_V (3 m spatial resolution) in Californian wetland ecosystems (non-tidal) for NDVI>0.25 for a range of evaporative fraction (F_E) representing stressed to unstressed conditions. F_E is an indicator of water availability and denotes the ratio of evaporation (latent heat flux) to equilibrium evaporation. (b) Temporal dynamics of $NDVI_{bb}$ (black dots) and NDVI (green dots) along with daily precipitation (P) (blue stairs) shows close correspondence between them in both East End and Mayberry.

Figure 6: Pooled evaluation plots of $NDVI_{bb}$ and $NIRv_{bb}$ versus Planet Fusion NDVI and NIR_V (3 m spatial resolution) by combining all the seven sites of Californian ecosystems for a range of evaporative fraction (F_E) representing stressed to unstressed conditions. F_E is an indicator of water availability and denotes the ratio of evaporation (latent heat flux) to equilibrium evaporation.

Figure 7: (a, c) Plots of $NDVI_{bb}$ and NIR_{Vbb} versus Landsat and Sentinel-2 NDVI and NIR_V (30 m spatial resolution) in energy-limited ecosystems of Biomet and NEON sites. Color shading is done by evaporative fraction (F_E) showing stressed to unstressed conditions which corresponds to water and energy limits within the energy-limited environment. (b, d) Illustrative examples of temporal dynamics of $NDVI_{bb}$ (black dots) and NDVI (green dots) along with daily precipitation (P) (blue stairs) showing close correspondence in the seasonal and interannual variability of $NDVI_{bb}$ and NDVI at the NEON sites Blandy Experimental Farm (xBL) and Dead Lake (xDL).

Figure 8: (a, c) Plots of $NDVI_{bb}$ and NIR_{Vbb} versus Landsat and Sentinel-2 NDVI and NIR_V (30 m spatial resolution) in water-limited ecosystems of Biomet and NEON sites. Color shading is done by evaporative fraction (F_E) showing stressed to unstressed conditions which corresponds to water and energy limits within the water-limited environment. (b, d) Illustrative examples of temporal dynamics of $NDVI_{bb}$ (black dots) and NDVI (green dots) along with daily precipitation (P) (blue stairs) showing close correspondence in the seasonal and interannual variability of $NDVI_{bb}$ and NDVI over Bouldin corn (Bi2), Vaira ranch (Var) and two grasslands sites of NEON Konza Prairie Biological Station (xKA and xKZ).

Figure 9: (a-b) Daily variation in $NDVI_{bb}$, Planet Fusion NDVI, Green Chromatic Coordinate (GCC) (secondary y-axis), and evaporative fraction (F_E) over agricultural ecosystems (alfalfa and corn) in California. Here we plot daily values, averaged over 4 years, normalized by the annual mean for that variable. (c-d) Correlation map showing the strength of seasonal relationship between individual variables. For corn, the correlation map is applicable for the growing season from March to September.

Figure 10: (a-b) Daily variation in $NDVI_{bb}$, Planet Fusion NDVI, Green Chromatic Coordinate (GCC) (secondary y-axis), and evaporative fraction (F_E) over grassland (Vaira ranch) and woody savanna (Tonzi ranch) ecosystems in California. Here we plot daily values, averaged over 4 years, normalized by the annual mean for that variable. (c-d) Correlation map showing the strength of seasonal relationship between individual variables during the growing season from March to October.

Figure 11: (a-b) Plots of intraseasonal variability (expressed as 'coefficient of variation', cv) in NDVI ($NDVI_{bb}$) and NIR_V (NIR_{Vbb}) versus intraseasonal variability in gross photosynthesis (A_G) by combining all the site data in different ecosystems of California. Color shading is by precipitation (P) variability. This also shows the steeper slope of cv-NDVI (and cv-$NDVI_{bb}$) vs. cv-A_G and cv-NIR_V (and cv-NIR_{Vbb}) vs. cv-A_G relationship with increasing precipitation variability.

Figure 12: (a, b) Site-level relationships of A_G versus $NDVI_{bb}$ and A_G versus $NIRv_{bb}*\Sigma Q^i$ at seven eddy covariance towers of UC Berkeley Biomet sites that includes 2 crop sites (one C4, one C3), one grassland site, one woody savanna and 3 wetland sites. (c, d) Similar plot is shown by plotting A_G with Planet Fusion NDVI and $NIRv_{bb}*\Sigma Q^i$. Here ΣQ^i and A_G are the daily integrated Q^i (MJ) and A_G (gC/m^2) obtained by summing up the half-hourly observation. Data points inside the red circle showed saturation in A_G with increasing $NIRv_{bb}*\Sigma Q^i$. These data points belong to corn crop and could presumably be associated with the diffuse component of Q^i. (e) Scatter plot of A_G versus $NDVI_{bb}^2*\Sigma Q^i$.

Figure 13: Plots of residual difference between $NDVI_{bb}$ and satellite NDVI ($\boldsymbol{\delta}_{NDVI}$ = $NDVI_{bb}$ - NDVI) versus Green Chromatic Coordinate (GCC) for a wide range of soil background conditions across diverse ecosystems. Color shading is by Soil Adjusted and Atmospherically Resistant Vegetation index (SARVI), which serves as an indicator of soil-canopy background. The black line indicates the average bias for each bin. This clearly indicates a consistent positive difference between $NDVI_{bb}$ and satellite NDVI during low vegetation or during vegetation senescence, which also coincides with low SARVI. The black line shows the mean bias pattern for different classes of GCC.

Figure 14: Illustrative examples of comparison between $\rho_{vis,bb}$ versus $\rho_{0.66}$ for a range of incident and reflected PAR (Q^i and Q^r) over alfalfa (a, b) and corn (c, d) in California. This clearly shows a tendency of systematic underestimation of $\rho_{vis,bb}$ with respect to $\rho_{0.66}$, and the underestimation increases at high Q^i and Q^r. Figures in the inset shows a similar comparison between $\rho_{nir,bb}$ versus $\rho_{0.86}$ for a range Q^i and Q^r. This analysis was performed with Planet Fusion data.

Figure 15: Illustrative examples of comparison between $\rho_{vis,bb}$ versus $\rho_{0.66}$ for a range of incident and reflected PAR (Q^i and Q^r) over grassland (Vaira ranch) (a, b) and woody savanna (Tonzi ranch) (c, d) in California. This clearly shows a tendency of systematic underestimation of $\rho_{vis,bb}$ with respect to $\rho_{0.66}$, and the underestimation increases at high Q^i and Q^r. Figures in the inset shows a similar comparison between $\rho_{nir,bb}$ versus $\rho_{0.86}$ for a range Q^i and Q^r. This analysis was performed with Planet Fusion data.

Figure 16: Illustrative examples of comparison between $\rho_{vis,bb}$ versus $\rho_{0.66}$ for a range of incident and reflected PAR (Q^i and Q^r) over deciduous broadleaf forests (DBF) (a, b), evergreen needleleaf forests (ENF) (c, d), and open shrubland (OSH) (e, f). This clearly shows a tendency of systematic underestimation of $\rho_{vis,bb}$ with respect to $\rho_{0.66}$, and the underestimation increases at high Q^i and Q^r. Figures in the inset shows a similar comparison between $\rho_{nir,bb}$ versus $\rho_{0.86}$ for a range Q^i and Q^r. This analysis was performed with HLS data since no Planet Fusion data was available for these ecosystems.

Figure 17: (a, c, e, g) Illustrative examples of comparison between Apogee spectrometer versus Planet Fusion spectral reflectances in red and NIR wavelengths in four representative ecosystems in California. (b, d, f, h) Comparison between Apogee spectrometer versus Planet Fusion and broadband NDVI in four representative ecosystems in California. This clearly shows a tendency of systematic underestimation of Apogee NDVI with respect to satellite, which is attributed to the disagreement in spectral reflectances between Apogee spectrometer and Planet Fusion.

Figure A1: Boxplot of statistical error metric of $NDVI_{bb}$ and $NIRv_{bb}$ with respect to satellite NDVI and NIRv by combining data of both L8/9 and S2 of HLS by combining data of different sites falling in different ecosystem categories. Here, nRMSD is the normalized root mean squared deviation. This is computed by normalizing RMSD with the range (maximum - minimum) of satellite NDVI and NIRv.

Figure A2: (a) Time series of daily broadband vegetation index ($NDVI_{bb}$), LAI and canopy gap fraction (P_{gap}) at the oak grass savanna (Tonzi ranch). The data points inside the red rectangular box represent the periods when $NDVI_{bb}$ and LAI showed maximum divergence, which coincided with larger gap fraction during the winter season. (b) Scatterplot of $NDVI_{bb}$ versus LAI by averaging daily data for four years, showing significantly high correlation during the growing season.

Figure A3: (a-f) Plots of intraseasonal variability (expressed as 'coefficient of variation', cv) in satellite (Planet Fusion) NDVI ($NDVI_{bb}$) and NIR_V (NIR_{Vbb}) versus intraseasonal variability in GPP (A_G) in different ecosystems of California. Color shading is by precipitation (P) variability. This also shows the steeper slope of cv-NDVI (and cv-$NDVI_{bb}$) vs. cv-A_G and cv-NIR_V (and cv-NIR_{Vbb}) vs. cv-A_G relationship with increasing precipitation variability.

Figure A4: Illustrative examples of comparison between $\rho_{vis,bb}$ versus $\rho_{0.66}$ and $\rho_{nir,bb}$ versus $\rho_{0.86}$ for a range of water stress (evaporative fraction, F_E) over alfalfa and corn in California. This clearly shows a tendency of systematic underestimation of $\rho_{vis,bb}$ with respect to $\rho_{0.66}$, and the underestimation increases with elevated water stress. This analysis was performed with Planet Fusion data.

Figure A5: Illustrative examples of comparison between $\rho_{vis,bb}$ versus $\rho_{0.66}$ and $\rho_{nir,bb}$ versus $\rho_{0.86}$ for a range of water stress (evaporative fraction, F_E) over grassland (Vaira ranch) and woody savanna (Tonzi ranch) in California. This clearly shows a tendency of systematic underestimation of $\rho_{vis,bb}$ with respect to $\rho_{0.66}$, and the underestimation increases with elevated water stress. This analysis was performed with Planet Fusion data.

Figure A6: Illustrative examples of comparison between $\rho_{vis,bb}$ versus $\rho_{0.66}$ and $\rho_{nir,bb}$ versus $\rho_{0.86}$ for a range of water stress (evaporative fraction, F_E) over deciduous broadleaf forest (DBF) and evergreen needleleaf forest (ENF). This clearly shows a tendency of systematic underestimation of $\rho_{vis,bb}$ with respect to $\rho_{0.66}$, in majority of the datapoints. This also shows a clear saturation of $\rho_{nir,bb}$ signal at high $\rho_{0.86}$. This analysis was performed with HLS data since no Planet Fusion data was available for these ecosystems.

Figure A7: Illustrative examples of the effects of variability (coefficient of variation, cv in percent) in fractional vegetation cover (f_c) on broadband versus satellite NDVI comparison at four different ecosystems. We took the cluster average of 10 x 10 pixel NDVI from Planet Fusion surrounding the tower sites. To understand the impact of f_c variability we took the standard deviation of f_c of 10 x 10 pixel and normalized with mean f_c of the same pixels.

Appendix

A1. Assessment of $NDVI_{bb}$ and $NIRv_{bb}$ in different ecosystems

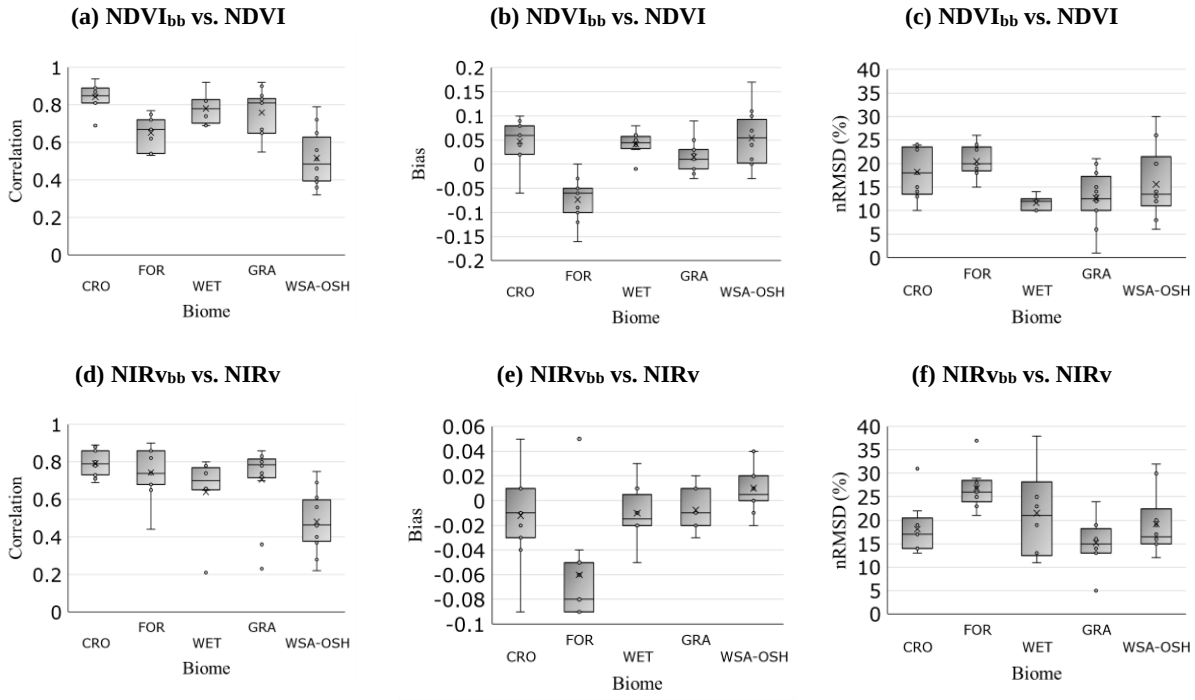

Figure A1: Boxplot of statistical error metric of $NDVI_{bb}$ and $NIRv_{bb}$ with respect to satellite NDVI and NIRv by combining data of both L8/9 and S2 of HLS by combining data of different sites falling in different ecosystem categories. Here, nRMSD is the normalized root mean squared deviation. This is computed by normalizing RMSD with the range (maximum - minimum) of satellite NDVI and NIRv.

Ecosystem wise analysis by combining data of both L8/9 and S2 revealed (**Fig. A1**) significantly high correlation between $NDVI_{bb}$ versus satellite NDVI in cropland (0.81 - 0.85), grassland (0.82 - 0.87), and wetlands (r = 0.68 - 0.78) (**Fig. A1a**). However, a relatively degraded, yet significant relationship was noted in forest (r = 0.52 - 0.59) and woody savanna-shrubland (0.48 - 0.64). The normalized RMSD (nRMSD) showed higher percentage difference in cropland and forest (18 - 22%) as compared to the other ecosystems (**Fig. A1b**). Boxplots also revealed high systematic negative mean bias in forest and systematic positive mean bias in cropland, grassland, and woody savanna-shrubland (**Fig. A1c**). Although no systematic difference in error metrics was identified with respect to L8/9 and S2 sensors, boxplot indicated relatively higher errors in NIR_{vbb}

as compared to $NDVI_{bb}$. Error statistics of individual sites with both L8/9 and S2 HLS data are listed in **Table A1** (for L8/9) and **Table A2** (for S2).

A2. Comparing $NDVI_{bb}$ with leaf area index (LAI)

To understand whether $NDVI_{bb}$ is able to capture the variation in leaf area index (LAI), we also analyzed $NDVI_{bb}$ with respect to LAI observations at the Tonzi ranch site (oak grass savanna). Significantly high correlation ($r = 0.82$) was found during the active growing season between day of the year (DOY) 130 to 280 and for the canopy gap fraction (P_{gap}) of 0.4 to 0.6 (**Fig. A2**). $NDVI_{bb}$ and LAI started to diverge with increasing P_{gap} beyond 0.65, which corresponds to the period around DOY 300 onwards (autumn), and this divergence remained until the warm spring around DOY 100. This is the time when grasses at the understory start greening up and $NDVI_{bb}$ can be affected due to the background effects. Differences in the nature of LAI measurement (upward looking digital camera) versus the estimation of broadband NDVI (downward looking radiation sensors) could be responsible for this divergence. The divergence between LAI and NDVI in autumn is also because leaf browning results in lower NDVI while leaves can still remain in the canopy affecting transmittance and LAI. This is one of the advantages of using NDVI over direct measurements of LAI from transmittance, as NDVI is related to the amount of green leaves and transmittance measures total LAI.

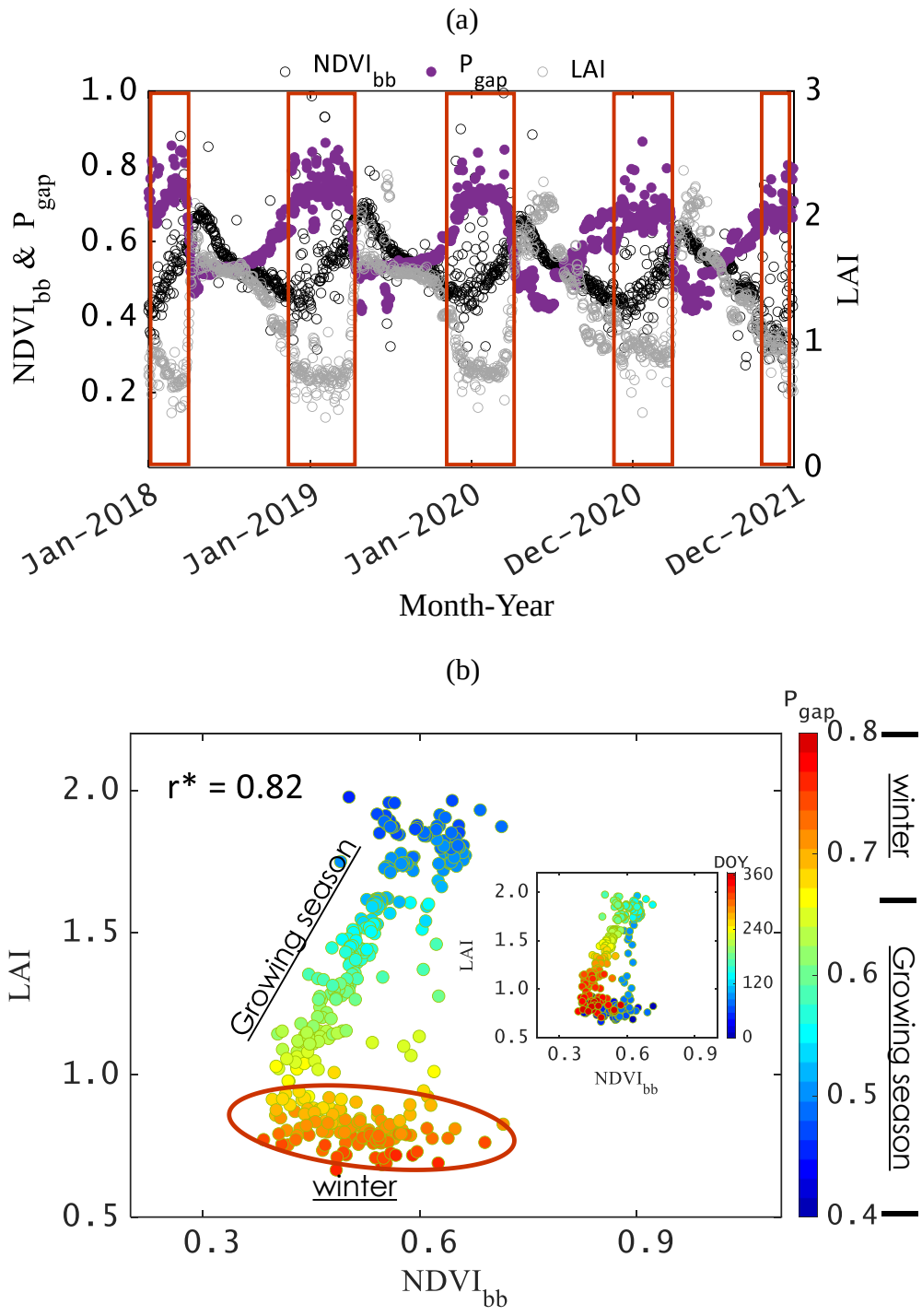

Figure A2: (a) Time series of daily broadband vegetation index ($NDVI_{bb}$), LAI and canopy gap fraction (P_{gap}) at the oak grass savanna (Tonzi ranch). The data points inside the red rectangular box represent the periods when $NDVI_{bb}$ and LAI showed maximum divergence, which coincided with larger gap fraction during the winter season. (b) Scatterplot of $NDVI_{bb}$ versus LAI by averaging daily data for four years, showing significantly high correlation during the growing season.

A3. $NDVI_{bb}$ and NIR_{Vbb} variability versus GPP variability across ecosystems (SQ3)

This analysis is based on the continuous time series EC tower A_G record of seven Biomet lab sites and the Planet Fusion data and is linked with section 3.3. The intraseasonal variability of both $NDVI_{bb}$ and NIR_{Vbb} was significantly correlated with the intraseasonal variability of A_G across different ecosystems (r = 0.51 - 0.65 and r = 0.49 - 0.74). Similar pattern was also noted in satellite NDVI and NIR_V versus A_G for all the ecosystems (r = 0.40 - 0.79 and r = 0.52 - 0.84) (**Fig. A3**).

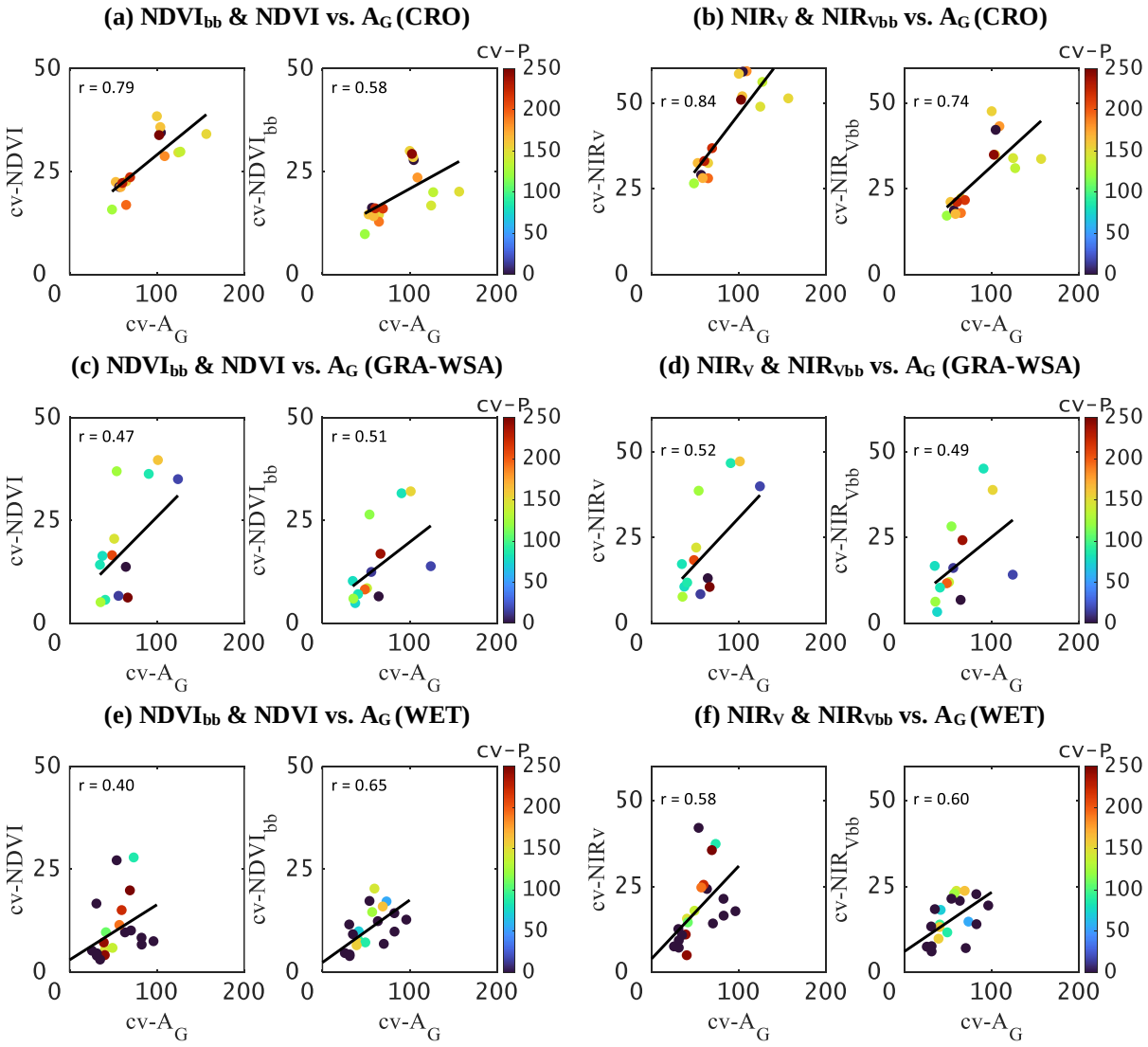

Figure A3: (a-f) Plots of intraseasonal variability (expressed as 'coefficient of variation', cv) in satellite (Planet Fusion) NDVI ($NDVI_{bb}$) and NIR_V (NIR_{Vbb}) versus intraseasonal variability in GPP (A_G) in different ecosystems of California. Color shading is by precipitation (P) variability. This also shows the steeper slope of cv-NDVI (and cv-$NDVI_{bb}$) vs. cv-A_G and cv-NIR_V (and cv-NIR_{Vbb}) vs. cv-A_G relationship with increasing precipitation variability.

A4. Effects energy-water-limitations on broadband spectral reflectance across different ecosystems?

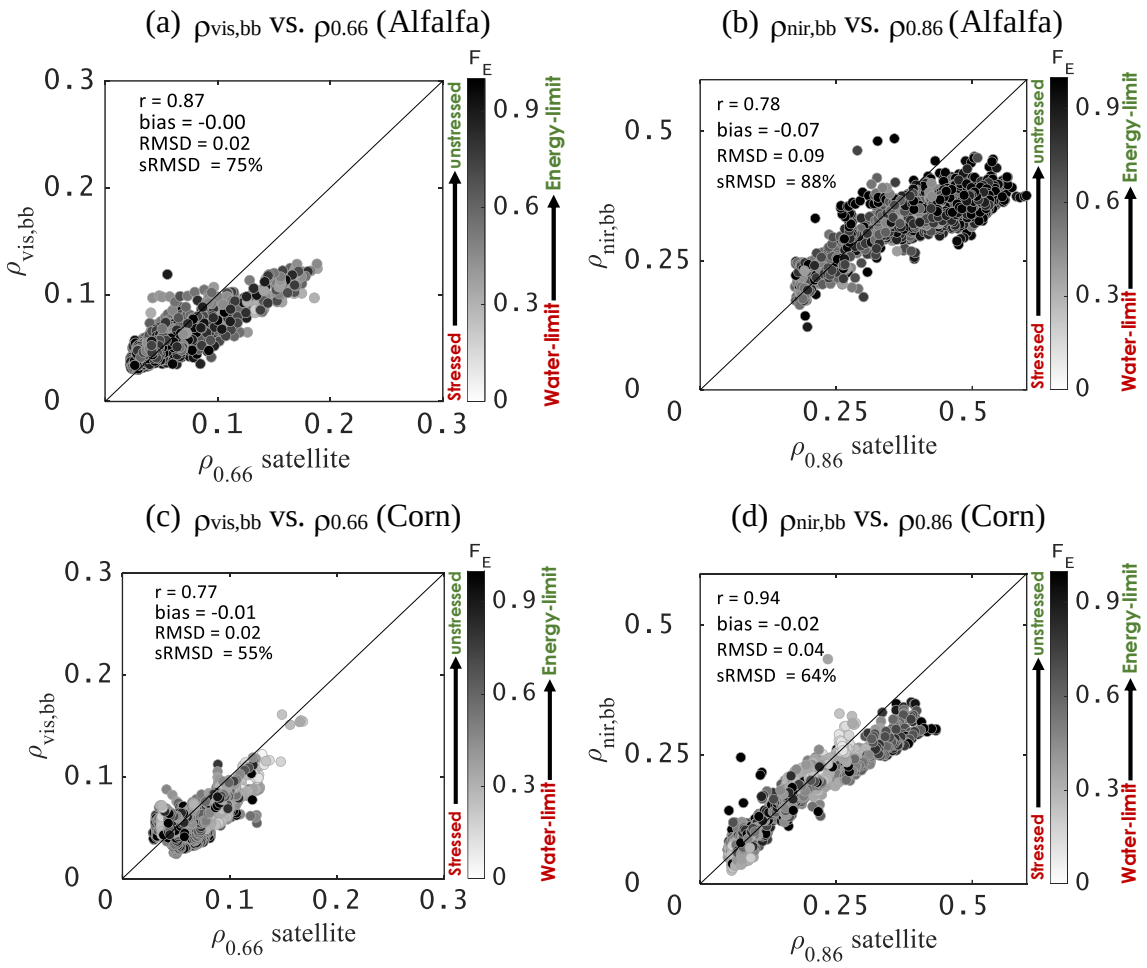

Figure A4: Illustrative examples of comparison between $\rho_{vis,bb}$ versus $\rho_{0.66}$ and $\rho_{nir,bb}$ versus $\rho_{0.86}$ for a range of water stress (evaporative fraction, F_E) over alfalfa and corn in California. This clearly shows a tendency of systematic underestimation of $\rho_{vis,bb}$ with respect to $\rho_{0.66}$, and the underestimation increases with elevated water stress. This analysis was performed with Planet Fusion data.

An analysis of $\rho_{vis,bb}$ and $\rho_{nir,bb}$ with respect to satellite narrowband red and NIR reflectance ($\rho_{0.66}$ and $\rho_{0.86}$) showed $\rho_{vis,bb}$ was systematically less as compared to $\rho_{0.66}$

($\rho_{vis,bb}$<$\rho_{0.66}$) for the majority of the data points (**Fig. A3 – A5**), and their differences were magnified with increasing water stress (F_E<0.3).

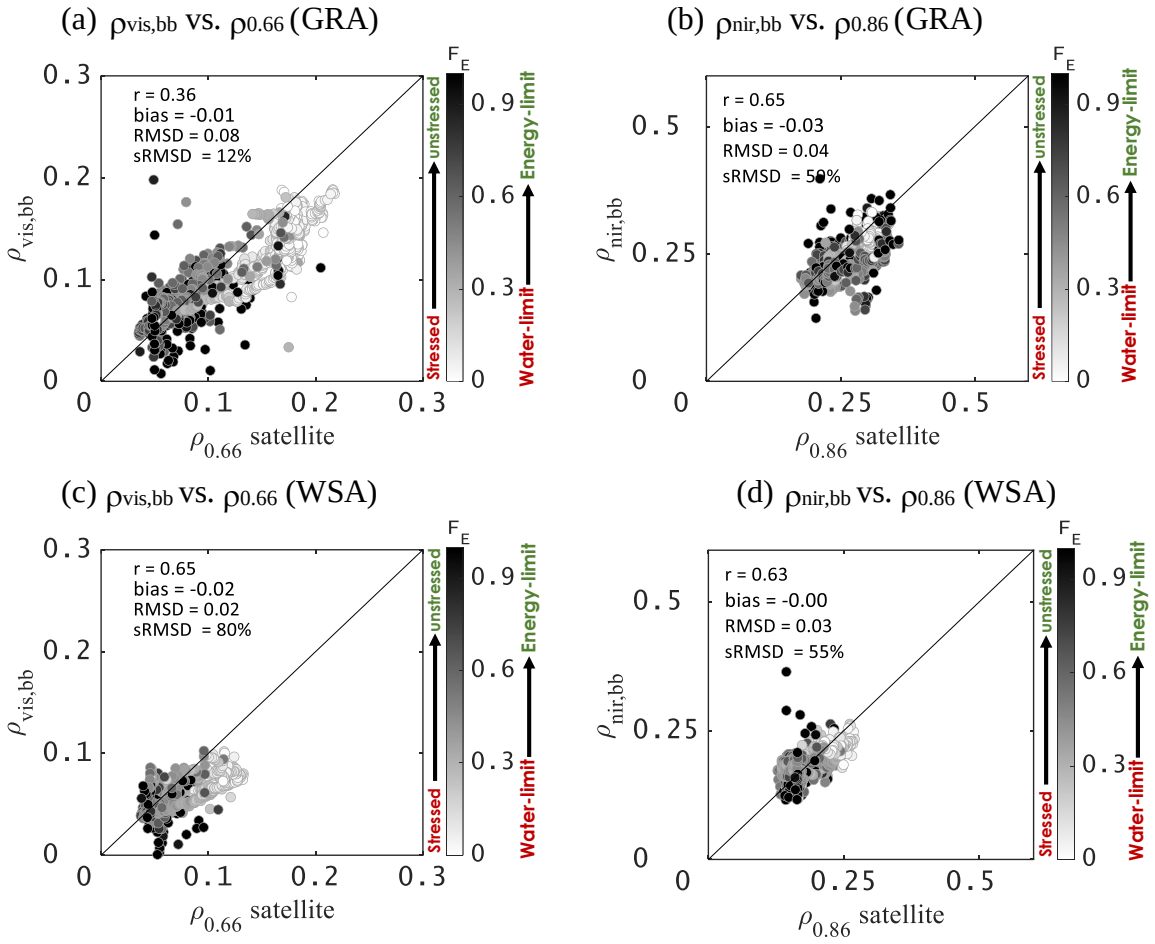

Figure A5: Illustrative examples of comparison between $\rho_{vis,bb}$ versus $\rho_{0.66}$ and $\rho_{nir,bb}$ versus $\rho_{0.86}$ for a range of water stress (evaporative fraction, F_E) over grassland (Vaira ranch) and woody savanna (Tonzi ranch) in California. This clearly shows a tendency of systematic underestimation of $\rho_{vis,bb}$ with respect to $\rho_{0.66}$, and the underestimation increases with elevated water stress. This analysis was performed with Planet Fusion data.

The effects of water limitations on $\rho_{nir,bb}$ was also evident at low $\rho_{0.86}$ and $\rho_{nir,bb}$ >$\rho_{0.86}$ at high water stress. This implies substantial overestimation of the numerator in $NDVI_{bb}$ as compared to satellite NDVI ($\rho_{nir,bb} - \rho_{vis,bb} > \rho_{0.86} - \rho_{0.66}$) with increasing water limitation, ultimately leading to a large positive difference between them when water stress progresses.

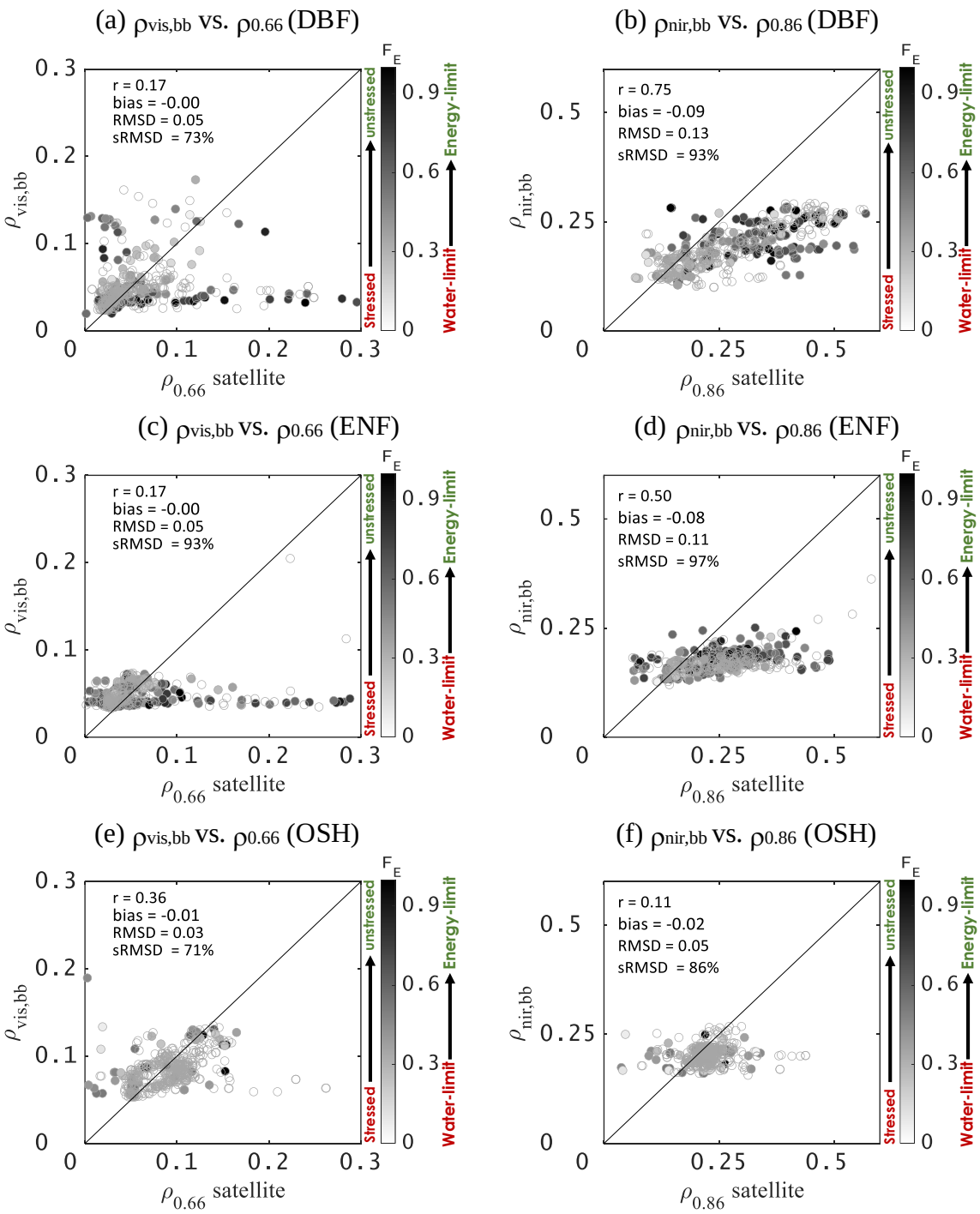

Figure A6: Illustrative examples of comparison between $\rho_{vis,bb}$ versus $\rho_{0.66}$ and $\rho_{nir,bb}$ versus $\rho_{0.86}$ for a range of water stress (evaporative fraction, F_E) over deciduous broadleaf forest (DBF) and evergreen needleleaf forest (ENF). This clearly shows a tendency of systematic underestimation of $\rho_{vis,bb}$ with respect to $\rho_{0.66}$, in majority of the datapoints. This also shows a clear saturation of $\rho_{nir,bb}$ signal at high $\rho_{0.86}$. This analysis was performed with HLS data since no Planet Fusion data was available for these ecosystems.

A5. Effects of variability of vegetation fraction on $NDVI_{bb}$ versus satellite NDVI relationship

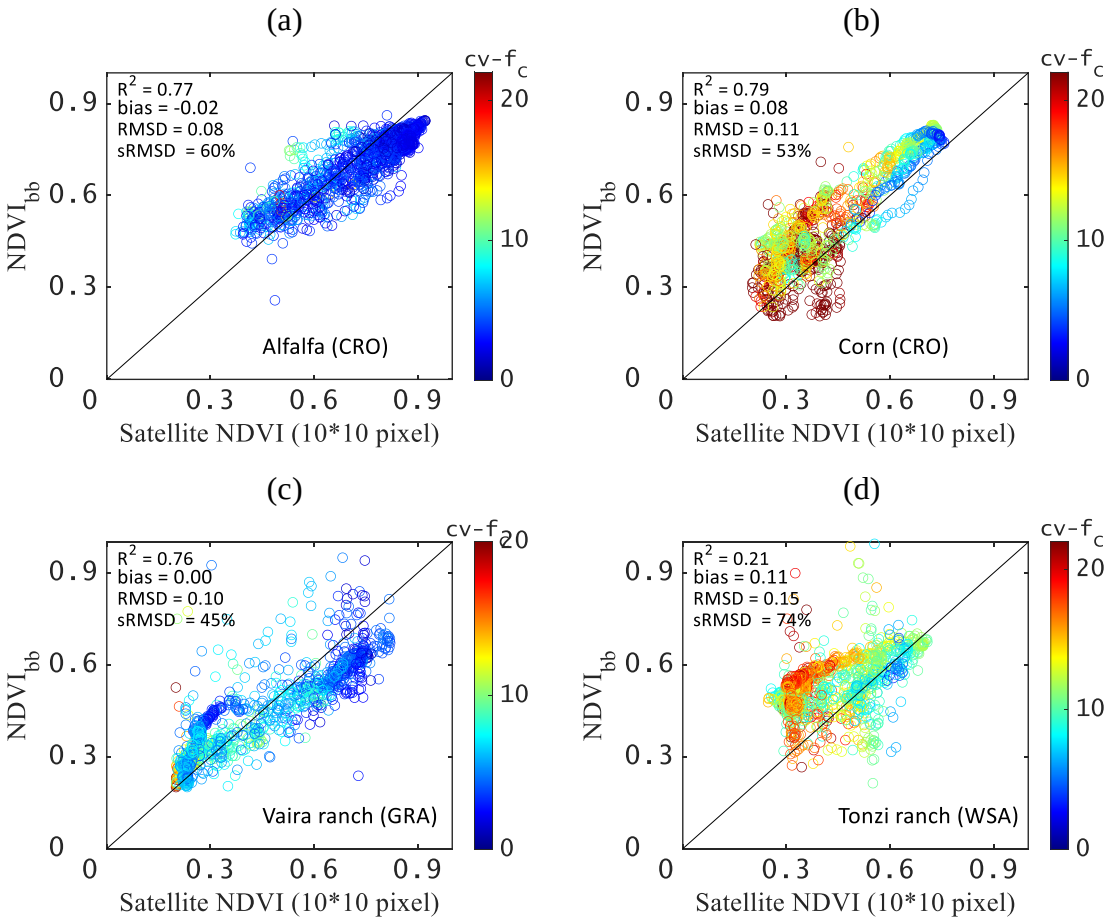

Figure A7: Illustrative examples of the effects of variability (coefficient of variation, cv in percent) in fractional vegetation cover (f_c) on broadband versus satellite NDVI comparison at four different ecosystems. We took the cluster average of 10 x 10 pixel NDVI from Planet Fusion surrounding the tower sites. To understand the impact of f_c variability we took the standard deviation of f_c of 10 x 10 pixel and normalized with mean f_c of the same pixels.

A simple analysis is conducted to examine the effects of coarser spatial resolution on the agreement between $NDVI_{bb}$ versus satellite NDVI. This analysis reveals the reasons for relatively higher errors in $NDVI_{bb}$ when it was compared with 30 m spatial resolution L8/9 and S2 NDVI from HLS datasets (as compared to Planet Fusion). This analysis is only possible over a small subset of sites in California where coincident data from both Planet Fusion and HLS is available. Therefore, investigation is made at four different ecosystems using data of UC Berkeley Biomet sites.

Figure A7 shows the effects of variability in fractional vegetation cover (f_c) on the comparison between $NDVI_{bb}$ versus satellite NDVI. To understand the impact of f_c variability, we estimated the coefficient of variation of f_c (cv-f_c, in percent.). We took the standard deviation of Planet Fusion (3 m spatial resolution) f_c over 10 x 10 pixel cutouts surrounding the towers and normalized it with mean f_c of the same numbers of pixels. Taking the cluster average of 10 x 10 pixel NDVI from Planet Fusion surrounding the tower sites, we found that the difference between $NDVI_{bb}$ versus satellite NDVI to be sensitive to high cv-f_c (≥20%). This showed overestimation of $NDVI_{bb}$ for low values of satellite NDVI at GRA and WSA (Fig. A6c, d). Overall, high systematic RMSD was found in both these ecosystems (45% in GRA and 74% in WSA) as compared to the errors obtained from NDVI averaging over 3x3 pixels (40% in GRA and 61% in WSA). The variability of f_c was very little over alfalfa and no significant difference due to pixel averaging was found at this site. For corn, the difference was found only at the start of the growing season when cv-f_c was high (≥20%) and the positive difference between $NDVI_{bb}$ versus satellite NDVI was narrowed down with full vegetation growth.

Table A1: Site wise error statistics of $NDVI_{bb}$ and NIR_{vbb} (parenthesis) with respect to L8/L9 Harmonized Landsat and Sentinel (HLS) data

Ecosystem	Site	r	bias	RMSD	nRMSD (%)
CRO	US-Bi1	0.81 (0.78)	0.02 (-0.03)	0.10 (0.08)	14 (17)
	US-Bi2	0.89 (0.86)	0.10 (0.01)	0.13 (0.04)	23 (14)
	US-Ne3	0.69 (0.69)	0.08 (0.05)	0.16 (0.10)	23 (19)
	US-UiA	0.94 (0.89)	-0.06 (-0.09)	0.12 (0.14)	18 (31)
	US-UiB	0.82 (0.80)	0.08 (-0.04)	0.17 (0.11)	24 (22)
	US-xSL	0.90 (0.73)	0.06 (0.00)	0.07 (0.02)	24 (14)
GRA	US-xAE	0.65 (0.72)	0.01 (-0.01)	0.08 (0.02)	12 (16)
	US-xCP	0.65 (0.70)	0.05 (0.01)	0.08 (0.02)	14 (13)
	US-xKA	0.81 (0.84)	0.01 (-0.02)	0.09 (0.04)	15 (14)
	US-xKZ	0.83 (0.80)	0.01 (-0.03)	0.13 (0.08)	20 (19)
	US-Var	0.92 (0.86)	-0.01 (-0.02)	0.08 (0.04)	10 (13)
	US-Wkg	0.67 (0.36)	-0.03 (-0.02)	0.07 (0.03)	13 (24)
WSA	US-Ton	0.65 (0.56)	0.10 (0.02)	0.13 (0.03)	13 (15)
	US-xSJ	0.51 (0.61)	-0.03 (-0.02)	0.10 (0.03)	13 (16)
OSH	US-xJR	0.72 (0.69)	0.07 (0.02)	0.08 (0.02)	20 (20)
	US-xNQ	0.36 (0.47)	0.04 (0.00)	0.07 (0.01)	8 (17)
	US-xSR	0.39 (0.28)	0.00 (-0.01)	0.06 (0.02)	14 (15)
FOR	US-xAB	0.62 (0.65)	-0.09 (-0.09)	0.14 (0.11)	24 (37)
	US-xBL	0.72 (0.90)	-0.10 (-0.10)	0.15 (0.12)	25 (27)
	US-xDL	0.72 (0.82)	-0.06 (-0.09)	0.13 (0.12)	18 (29)
	US-xHa	0.54 (0.74)	-0.05 (-0.09)	0.18 (0.13)	20 (26)
	US-xJE	0.54 (0.68)	-0.12 (-0.08)	0.17 (0.10)	20 (26)
WET	US-Myb	0.69 (0.66)	0.05 (0.01)	0.09 (0.03)	12 (13)
	US-TW1	0.74 (0.74)	-0.01 (-0.05)	0.07 (0.06)	10 (25)
	US-TW4	0.69 (0.21)	0.04 (-0.02)	0.10 (0.09)	14 (38)

Table A2: Site wise error statistics of $NDVI_{bb}$ and NIR_{vbb} with respect to S2 Harmonized Landsat and Sentinel (HLS) data

Ecosystem	Site	r	bias	RMSD	nRMSD
CRO	US-Bi1	0.85 (0.79)	0.02 (-0.02)	0.09 (0.07)	10 (13)
	US-Bi2	0.81 (0.88)	0.09 (0.01)	0.15 (0.04)	15 (14)
	US-Ne3	-	-	-	-
	US-UiA	-	-	-	-
	US-UiB	-	-	-	-
	US-xSL	0.87 (0.71)	0.04 (-0.01)	0.07 (0.04)	13 (19)
GRA	US-xAE	0.90 (0.81)	0.02 (0.01)	0.05 (0.02)	10 (16)
	US-xCP	0.65 (0.74)	0.09 (0.02)	0.11 (0.02)	1 (5)
	US-xKA	0.82 (0.78)	0.03 (-0.01)	0.09 (0.03)	12 (14)
	US-xKZ	0.81 (0.83)	-0.01 (-0.02)	0.14 (0.07)	21 (19)
	US-Var	0.85 (0.79)	0.03 (0.01)	0.11 (0.04)	18 (13)
	US-Wkg	0.55 (0.23)	-0.02 (-0.01)	0.07 (0.03)	6 (16)
WSA	US-Ton	0.46 (0.37)	0.17 (0.04)	0.19 (0.05)	30 (30)
	US-xSJ	0.56 (0.46)	-0.01 (-0.01)	0.11 (0.03)	12 (12)
OSH	US-xJR	0.79 (0.75)	0.11 (0.04)	0.12 (0.04)	26 (32)
	US-xNQ	0.32 (0.40)	0.07 (0.01)	0.09 (0.01)	6 (19)
	US-xSR	0.41 (0.22)	0.01 (-0.01)	0.06 (0.02)	14 (16)
FOR	US-xAB	-	-	-	-
	US-xBL	0.77 (0.87)	-0.05 (-0.05)	0.12 (0.07)	19 (21)
	US-xDL	0.75 (0.86)	0.01 (-0.04)	0.13 (0.08)	19 (23)
	US-xHa	0.53 (0.44)	-0.16 (-0.06)	0.26 (0.12)	26 (28)
	US-xJE	0.67 (0.74)	-0.03 (-0.05)	0.11 (0.07)	15 (25)
WET	US-Myb	0.83 (0.65)	0.08 (0.03)	0.10 (0.04)	14 (23)
	US-TW1	0.82 (0.78)	0.03 (-0.02)	0.10 (0.04)	12 (19)
	US-TW4	0.92 (0.80)	0.06 (-0.01)	0.08 (-0.03)	10 (11)